

Bayesian Transfer Learning for Artificially Intelligent Geospatial Systems: A Predictive Stacking Approach

Luca Presicce^a and Sudipto Banerjee^b

^a Department of Economics, Management and Statistics,
Università degli studi Milano-Bicocca, Milano, Italy

^bDepartment of Biostatistics,
University of California Los Angeles, CA, USA.

Abstract

Building artificially intelligent geospatial systems require rapid delivery of spatial data analysis at massive scales with minimal human intervention. Depending upon their intended use, data analysis may also entail model assessment and uncertainty quantification. This article devises transfer learning frameworks for deployment in artificially intelligent systems, where a massive data set is split into smaller data sets that stream into the analytical framework to propagate learning and assimilate inference for the entire data set. Specifically, we introduce Bayesian predictive stacking for multivariate spatial data and demonstrate rapid and automated analysis of massive data sets. Furthermore, inference is delivered without human intervention without excessively demanding hardware settings. We illustrate the effectiveness of our approach through extensive simulation experiments and in producing inference from massive datasets on sea surface temperatures and vegetation index that are indistinguishable from traditional (and more expensive) statistical approaches.

Keywords— Bayesian predictive stacking; Climate science; Gaussian process; Geospatial systems; Matrix-variate spatial models; Transfer learning.

1 Introduction

Geospatial artificial intelligence (GEOAI) is a rapidly evolving discipline at the interface of machine learning and spatial data science that attempts to harness the analytical capabilities of Artificial Intelligence (AI) to analyze massive amounts of geographic data and conduct data driven scientific discoveries in diverse domains within the environmental and physical sciences. The area, while still fledgling, presents opportunities for statisticians to devise

essential data analytic tools that should comprise an artificially intelligent “geospatial” system. Constructing comprehensive AI-based geospatial systems involve expertise in computer science relating to efficiently designed Geographic Information Systems (GIS) databases, conventional machine learning tools based upon algorithms for spatial interpolation, and statistical or probabilistic learning tools to offer scientific inference. This manuscript concerns itself primarily with statistical learning tools for artificially intelligent GEOAI systems.

What, if at all, should be the role of formal statistical inference in GEOAI? Formal inference for spatial and spatial-temporal random fields enjoy a venerable intellectual presence spanning several decades of theoretical developments within classical and Bayesian paradigms (see, e.g., [Cressie, 1993](#); [Stein, 1999](#); [Gelfand et al., 2010](#); [Cressie and Wikle, 2011](#); [Banerjee et al., 2015](#)). With increasing complexity in spatially oriented datasets, statisticians have built richly structured hierarchical models in their pursuit of “full” probabilistic inference. The term “full” loosely refers to approaches that attempt to estimate *all* unknowns in the model including all parameters (irrespective of how well they are identified by the data), random effects or partial realizations of the process, and predictive random variables for probabilistic interpolation at arbitrary locations (and time points in spatial-temporal data).

Statisticians would, we believe, broadly agree that GEOAI offers sufficient intellectual space to accommodate rigorous probabilistic learning as a crucial constituent in artificially intelligent data analysis systems. Spatial modeling relies upon Gaussian processes (GPs) to model dependence and achieves superior predictive inference. While GPs afford flexibility and are a conspicuous choice in spatial modeling, their covariance kernels do not necessarily yield computationally exploitable structures for the covariance matrices and the computational requirements for full inference become onerous and impracticable for massive datasets.

This presents a conundrum for statisticians: should we strive to completely retain the probabilistic rigors of theoretical inference, which may be computationally burdensome, or even impracticable, given the massive amounts of data, or should we concede uncertainty

quantification and adopt algorithm-driven data analysis that would easily scale massive data sets? Spatial data analysis at unprecedented scales requires some concessions from conventional decision-theoretic paradigms as has been reflected, for example, in a recent comprehensive case study by [Zhou et al. \(2022\)](#), who synthesize statistical models with machine learning algorithms to measure temporal trends and spatial distribution of housing vitality by exploiting information from multiple sources (also see the discussion by [Banerjee, 2022](#), for conventional Bayesian modeling perspectives and its challenges). Other efforts in melding machine learning methods with formal spatial statistics include deep learning for spatial data ([Zammit-Mangion et al., 2022](#); [Wikle and Zammit-Mangion, 2023](#), with the latter offering a comprehensive review of spatial machine learning) and, in a very related domain, for deep GP emulation in computer experiments ([Sauer et al., 2023b](#)), and spatial random forests ([Georganos et al., 2021](#); [Talebi et al., 2022](#); [Saha et al., 2023](#)).

Even a cursory review reveals a significant literature on statistical methods for massive spatial datasets, which is too vast to be summarized here (see, e.g., [Banerjee, 2017](#); [Heaton et al., 2017](#), and references therein). Within the hierarchical setup $[data \mid process] \times [process \mid parameters] \times [parameters]$, inference proceeds from spatial processes that scale massive data sets. Examples range from reduced-rank processes or subsets of regression approaches ([Quiñonero-Candela and Rasmussen, 2005](#); [Cressie and Johannesson, 2008](#); [Banerjee et al., 2008](#); [Wikle, 2010](#), and references therein), multi-resolution approaches ([Nychka et al., 2015](#); [Katzfuss, 2017](#)), and graph-based models [Vecchia \(1988\)](#); [Datta et al. \(2016\)](#); [Katzfuss and Guinness \(2021\)](#); [Dey et al. \(2022\)](#); [Sauer et al. \(2023a\)](#). Full inference typically requires efficient Markov chain Monte Carlo (MCMC) ([Finley et al., 2019](#)), variational approximations ([Ren et al., 2011](#); [Wu et al., 2022](#); [Cao et al., 2023](#)) and a significant body of literature on Gaussian Markov random field approximations ([Rue et al., 2009](#); [Lindgren et al., 2011](#), and references therein) in conjunction with integrated nested Laplace approximations (INLA) for computing the marginal distributions of the process at given locations.

The aforementioned methods focus upon richness of statistical inference, but almost invariably involve a significant amount of human intervention to analyze spatial data. Even the simplest of geostatistical datasets require exploratory data analysis to learn about aspects of the underlying process that are weakly identified by the data (Zhang, 2004; Tang et al., 2021). Building a GEOAI system, on the other hand, will require minimizing human intervention in offering a robust framework for spatial data analysis. This presents enough challenges that preclude a comprehensive solution in its entirety within the scope of a single manuscript. Nevertheless, we devise a spatial data analytic framework that holds significant promise for GEOAI. The premise of this approach relies upon two basic tenets: (i) model-based statistical inference for underlying spatial processes (including multivariate processes) in a robust and largely automated manner with minimal human input; and (ii) achieving such inference for truly massive amounts of data without resorting to iterative algorithms that may require significant human intervention to diagnose convergence (such as in MCMC).

We wish to retain the benefits of Bayesian hierarchical models, convincingly documented in the aforementioned manuscripts, with regard to spatial interpolation of the underlying stochastic process. In particular, we seek predictive inference over the uncountable collection of points in the spatial domain while propagating uncertainty about the model’s estimation in such inference. However, some compromises with regard to richness of models are inevitable from the standpoint of GEOAI. At the same time, statistical distribution theory has much to offer and we harness analytical closed-form distribution theory within a family of matrix-variate distributions to deliver inference. This is possible only by “fixing” certain spatial correlation kernel parameters that are weakly identified and hinder automated inference. Our approach relies upon carrying out fast and exact inference based upon the matrix-variate distributions and then assimilating the inference using Bayesian predictive stacking or BPS (Wolpert, 1992; Yao et al., 2018). Stacking (Breiman, 1996) is primarily related to predictions by minimizing the generalization error rate of one or more models.

To analyze massive amounts of data to be accessed in a GEOAI system, we devise Bayesian transfer learning over a streaming set of spatial datasets. We envisage a setting where the data stream into the GEOAI system in the form of K subsets, where each subset is composed of $\approx n/K$ locations with K being a function of computational resources available to GEOAI. We analyze and transfer learning from one dataset to the next and assimilate inference from these subsets to the full data set over n locations. The concept of delegating Bayesian calculations to a group of independent datasets is intuitive and has been explored from diverse perspectives. Examples include Consensus Monte Carlo (CMC) (Scott et al., 2016) and its kernel-based adaptations (Rendell et al., 2021), Bayesian meta-analysis in clinical applications (Parmigiani, 2002, see, e.g., Chapter 4 in) and in spatially-temporally structured data (Bell et al., 2005; Kang et al., 2011); and, more recently, approaches such as “meta-kriging” using geometric medians of posterior distributions (Srivastava et al., 2015; Minsker et al., 2017; Guhaniyogi and Banerjee, 2018, 2019; Guhaniyogi et al., 2019). However, each of these approaches have, hitherto, relied upon MCMC or other iterative algorithms for estimating the weakly identifiable parameter. We, instead, propose to execute transfer learning using a double stacking approach. We first obtain stacked inference for each of the parameters within each subset and, then, assimilate inference across subsets by a second stacking algorithm. A flowchart is supplied in Figure 1 comprising three steps: (i) partition data into smaller subsets; (ii) analyze each subset by stacking conjugate posteriors in closed form; and (iii) stack across data sets to deliver inference for the entire data.

The contents of the paper evolve in accordance with Figure 1. Section 2 outlines Bayesian transfer learning using double BPS. Section 3 provides details on computational aspects. Section 4 presents simulation experiments designed for empirically evaluating double BPS. Section 5 analyzes a very large climate data set with observed locations in the millions at global scales. Finally, Section 6 concludes with some discussion. References to an accompanying Supplement are provided throughout the article and after Section 6.

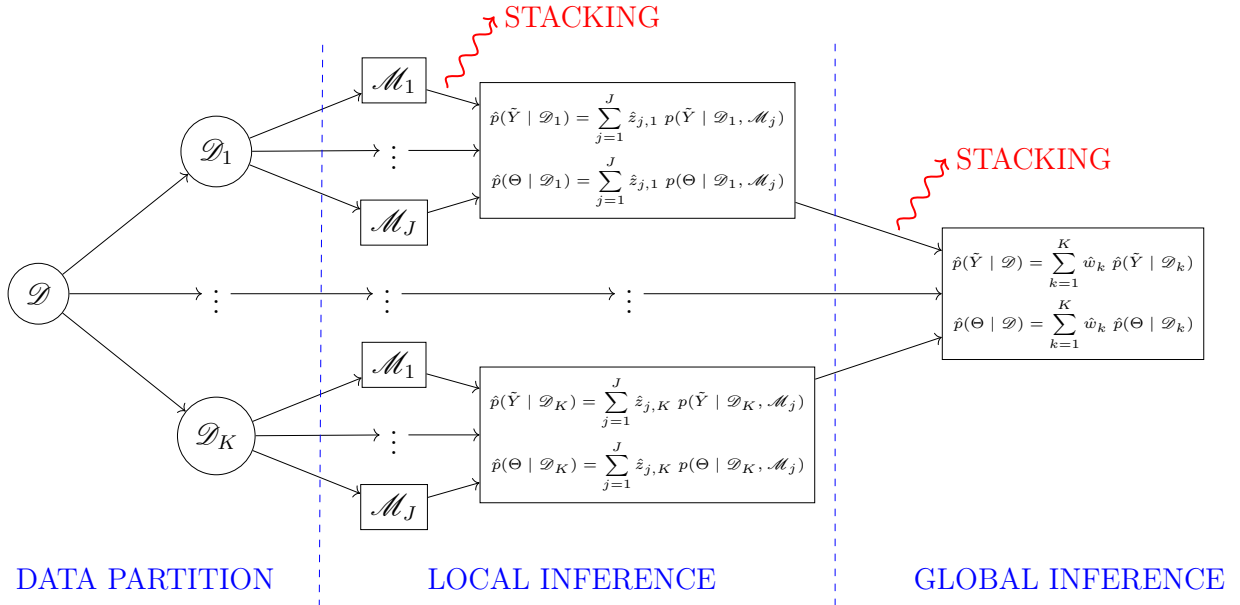


Figure 1: Double Bayesian predictive stacking approach representation

2 Bayesian transfer learning

Transfer learning (TL) broadly refers to propagating knowledge from one task to accomplish a different task. We consider transferring inference from one subset to the next in a stream of subsets to analyze the entire dataset. Learning from spatial random fields is challenging due to inherent dependencies in the data and we seek to infer about a latent spatial process (uncountable collection of unobserved random variables) with limited data (partially observed finite realization of the process). We develop an automated approach for GEOAI.

2.1 Divide-and-Conquer Multivariate Bayesian inference

Let $Y_{n \times q}$ be an $n \times q$ random matrix that is endowed with a probability law from the matrix-normal distribution, $MN(M, V, U)$, with probability density function

$$p(Y | M, V, U) = \frac{\exp \left[-\frac{1}{2} \text{tr} \{ U^{-1} (Y - M)^T V^{-1} (Y - M) \} \right]}{(2\pi)^{\frac{np}{2}} |U|^{\frac{n}{2}} |V|^{\frac{q}{2}}}, \quad (2.1)$$

where $\text{tr}(\cdot)$ is the trace operator on a square matrix, M is the mean matrix, and V and U are the $n \times n$ row-covariance and $q \times q$ column covariance matrices, respectively. We consider

the matrix-variate Bayesian linear regression model

$$Y = X\beta + E_Y, E_Y \sim \text{MN}(O, V, \Sigma); \beta = M_0 m_0 + E_\beta, E_\beta \sim \text{MN}(O, M_0, \Sigma), \quad (2.2)$$

where Y is $n \times q$, X is $n \times p$ comprising explanatory variables, β is $p \times q$ consisting of regression slopes, E_Y and E_β are zero-centered random matrices with row covariances V and M_0 , respectively, and a shared column covariance matrix Σ . We assign an inverse-Wishart distribution $\Sigma \sim \text{IW}(\Psi_0, \nu_0)$ and denote the joint density of β and Σ by $\text{MNIW}(M_0 m_0, M_0, \Psi_0, \nu_0)$, which affords a closed-form posterior for $\{\beta, \Sigma\}$ in the same family.

Let $\mathcal{D} = \{Y, X\}$ be the entire dataset, which is too massive to even be accessed, let alone be analyzed using (2.1), within the GEOAI system. Therefore, we envisage K disjoint and exhaustive subsets $\mathcal{D} = \{\mathcal{D}_1, \dots, \mathcal{D}_K\}$ streaming into GEOAI as a sequence. Each $\mathcal{D}_k = \{Y_k, X_k\}$ consists of n_k rows of Y and X , where $n = \sum_{k=1}^K n_k$, Y_k is $n_k \times q$ and X_k is $n_k \times p$ for each $k = 1, \dots, K$. We now fit (2.2) to each subset using $Y_k = X_k \beta + E_k$, $E_k \sim \text{MN}(O, V_k, \Sigma)$, where V_k is the $n_k \times n_k$ row-covariance matrix corresponding to the rows in Y_k ; the specification for $\{\beta, \Sigma\}$ remains as in (2.2). Starting with $\text{MNIW}(\beta, \Sigma | M_k m_k, M_k, \Psi_k, \nu_k)$ at $k = 0$ (the prior), we use Bayesian updating $p(\beta, \Sigma | \mathcal{D}_{1:k+1}) \propto p(\beta, \Sigma | \mathcal{D}_{1:k}) \times p(Y_{k+1} | X_{k+1} \beta, V_{k+1}, \Sigma)$ to obtain $\beta, \Sigma | \mathcal{D}_{1:k+1} \sim \text{MNIW}(M_{k+1} m_{k+1}, M_{k+1}, \Psi_{k+1}, \nu_{k+1})$ with $M_{k+1}^{-1} = M_k^{-1} + X_{k+1}^T V_{k+1}^{-1} X_{k+1}$, $m_{k+1} = m_k + X_{k+1}^T V_{k+1}^{-1} Y_{k+1}$, $\nu_{k+1} = \nu_k + n_{k+1}$, and $\Psi_{k+1} = \Psi_k + Y_{k+1}^T V_{k+1}^{-1} Y_{k+1} + m_k^T M_k m_k - m_{k+1}^T M_{k+1} m_{k+1}$. Upon termination at $k = K$, we exactly recover the posterior distribution $p(\beta, \Sigma | \mathcal{D})$. There is no need to interact between the subsets, and computational complexity is determined solely by the dimension of the subsets.

Spatial random fields immediately present a challenge. The above method delivers full inference without any loss of information only if Y_k 's are reasonably assumed to be independent (or exchangeable) across blocks. If each row of Y corresponds to one of n spatial locations so that V is an $n \times n$ spatial correlation matrix, the above scheme requires that each V_k is the spatial correlation matrix constructed from the n_k spatial locations in \mathcal{D}_k .

Independence across the K blocks may yield reasonable inference, especially if it is possible to design the blocks such that the spatial correlation across blocks do not impact overall inference, but this will require significant human intervention or a separate AI system for designing such blocks. We seek to avoid this in GEOAI.

Instead, we devise a method for assimilating the learning from each of these blocks using predictive stacking. We exploit the fact that V is indexed by a small number of parameters in a spatial correlation kernel. Fixing these parameters fixes V , and hence V_k for each k , yielding closed-form posterior inference on β and Σ based upon the entire dataset as described above. Stacking combines these analytically accessible distributions using an optimal set of weights that are computed using a convex optimization algorithm. These weights are then used to reconstruct the posterior and predictive distributions for the spatial random field without imposing block independence. It is worth remarking here that existing “meta-kriging” and related “divide and conquer” approaches (e.g., [Guhaniyogi and Banerjee, 2018](#); [Scott et al., 2016](#), and other references on “divide and conquer” methods provided in Section 1) analyze subsets of data using MCMC, which is expensive and not fully automated. A key distinction of the current manuscript is that we abandon all iterative estimation algorithms, let alone expensive MCMC, and focus on assimilating inference using closed forms of distributions. The matrix-variate formulation we pursue enhances flexibility and scope of applications.

What remains to be resolved is the issue of fixing the parameters in V . These parameters govern the strength of association across the spatial random field and possibly the smoothness of the field. Unfortunately, these parameters are weakly identified by the data and posterior learning struggles due to slower convergence of iterative algorithms. Also, exploratory spatial data science tools, such as variograms, for gleaning information about these parameters will also be less helpful as they may suggest different values for each of the variables indexed by the columns, while we insist on retaining a single parameter to exploit conjugate distribution

theory. Hence, we collect the closed-form posterior distributions obtained for a collection of fixed values of the spatial parameters and, subsequently, average these posterior distributions.

2.2 Bayesian stacking of predictive densities

Bayesian predictive stacking (BPS) assimilates models using a weighted distribution in the convex hull, $C = \left\{ \sum_{j=1}^J w_j p(\cdot | \mathcal{D}, \mathcal{M}_j) : \sum_j w_j = 1, w_j \geq 0 \right\}$, of individual posterior distributions by maximizing the score (Gneiting and Raftery, 2007; Yao et al., 2018) to fetch

$$(w_1, \dots, w_J)^\top = \arg \max_{w \in S_1^J} \frac{1}{n} \sum_{i=1}^n \log \sum_{j=1}^J w_j p(Y_i | \mathcal{D}_{-i}, \mathcal{M}_j) , \quad (2.3)$$

where \mathcal{D}_{-i} is the dataset excluding the i -th observation, or block (indexed by a row) of observations in the matrix Y , and $\mathcal{M} = (\mathcal{M}_1, \dots, \mathcal{M}_J)$ are J different models. For any given dataset \mathcal{D} , these J different models correspond to fixed spatial correlation kernel parameters in V and deliver closed-form analytic distributions. Solving (2.3) minimizes the Kullback-Leibler divergence from the true predictive distribution and is executed using convex optimization (Grant and Boyd, 2008; Fu et al., 2020). While the true predictive distribution is unknown, we can use a leave-one-out (LOO) estimate of the expected value of the score (see. e.g., Yao et al., 2018, for details), which requires fitting the model n times as we exclude one row of the data \mathcal{D} at a time so we prefer K-fold cross-validation as a more cost-effective method for generating predictions (Breiman, 1996).

2.3 Accelerated learning for spatial random fields

We turn to adapting the aforementioned concepts into an automated learning framework for GEOAI. Let $\mathcal{S} = \{s_1, \dots, s_n\} \subset \mathcal{D}$ be a set of n locations yielding observations on q possibly correlated outcomes collected into a $q \times 1$ vector $y(s) = (y_1(s), \dots, y_q(s))^\top$ for each $s \in \mathcal{S}$. We collect these measurements into the $n \times q$ matrix $Y = [y_j(s_i)^\top]$ for $i = 1, \dots, n$

and $j = 1, \dots, q$. Let $X = [x(s_i)^T]$ be $n \times p$ with rows $x(s_i)^T$ consisting of $p < n$ explanatory variables at location $s_i \in \mathcal{S}$; we assume X has rank p . We cast this into (2.2), but explicitly introduce a latent $q \times 1$ spatial process $\omega(s)$ as

$$\begin{aligned} Y &= X\beta + \Omega + E, \quad E | \Sigma \sim \text{MN}(O, (\alpha^{-1} - 1)\mathbb{I}_n, \Sigma); \quad \Sigma \sim \text{IW}(\Psi_0, \nu_0); \\ \beta &= M_0 m_0 + E_\beta, \quad E_\beta | \Sigma \sim \text{MN}(O, M_0, \Sigma); \quad \Omega | \Sigma \sim \text{MN}(O, V, \Sigma), \end{aligned} \quad (2.4)$$

where $\Omega = [\omega(s_i)^T]$ is $n \times q$ with rows $\omega(s_i)^T$. To capture spatial dependence, V is an $n \times n$ spatial correlation matrix with (i, j) -th element equaling the value of a positive definite spatial correlation function $\rho(s_i, s_j; \phi)$ indexed by parameter(s) ϕ . To account for measurement errors in observations, as is customary in geostatistics, we introduce a discontinuity in the spatial correlation function and modify the elements to $\rho(s_i, s_j; \phi) + (\alpha^{-1} - 1)\mathbb{1}_{s_i=s_j}$, where $\alpha \in [0, 1]$ represents the proportion of total variability attributed to the spatial process.

The covariance among the elements of $y(s)$ within s is given by the elements of $(\alpha^{-1} - 1)\Sigma$. Thus, Σ is the within-location (nonspatial) dependence among the outcomes adjusted by a scale of $(\alpha^{-1} - 1)$ to accommodate additional variation at local scales. The parameter α is the ratio of the ‘‘partial sill’’ to the ‘‘sill’’ in classical geostatistics. In the special case when $\Sigma = \sigma^2\mathbb{I}_q$, we interpret $\alpha = \sigma^2 / (\sigma^2 + \tau^2)$, where τ^2 is the measurement error variance (‘‘nugget’’) and α is the ratio of the spatial variance (partial sill) to the total variance (sill).

Letting $\gamma^T = [\beta^T, \Omega^T]$ be $q \times (p + n)$, we assume $\{\gamma, \Sigma\} \sim \text{MNIW}(\mu_\gamma, V_\gamma, \Psi_0, \nu_0)$, where

$$\text{MNIW}(\gamma, \Sigma | \mu_\gamma, V_\gamma, \Psi_0, \nu_0) = \text{IW}(\Sigma | \Psi_0, \nu_0) \times \text{MN}_{p,q}(\gamma | \mu_\gamma V_\gamma, \Sigma), \quad (2.5)$$

with $\mu_\gamma^T = [m_0^T M_0, 0_{q \times n}]$ and $V_\gamma = \text{blockdiag}\{M_0, \rho_\phi(\mathcal{S}, \mathcal{S})\}$. The MNIW prior is conjugate with respect to the matrix-normal likelihood. Thus, for any fixed $\{\alpha, \phi\}$ and hyperparameters in the prior density, we obtain a MNIW posterior density for $\{\gamma, \Sigma\}$,

$$p(\gamma, \Sigma | \mathcal{D}) = \text{MNIW}(\gamma, \Sigma | \mu_\gamma^*, V_\gamma^*, \Psi^*, \nu^*), \quad (2.6)$$

where $V_\gamma^* = \begin{bmatrix} \frac{\alpha}{1-\alpha} X^T X + M_0^{-1} & \frac{\alpha}{1-\alpha} X^T \\ \frac{\alpha}{1-\alpha} X & \rho_\phi^{-1}(\mathcal{S}, \mathcal{S}) + \frac{\alpha}{1-\alpha} \mathbb{I}_n \end{bmatrix}^{-1}$ and $\mu_\gamma^* = V_\gamma^* \begin{bmatrix} \frac{\alpha}{1-\alpha} X^T Y + m_0 \\ \frac{\alpha}{1-\alpha} Y \end{bmatrix}$,
 $\Psi^* = \Psi_0 + \frac{\alpha}{1-\alpha} Y^T Y + m_0^T M_0 m_0 - \mu_\gamma^{*\top} V_\gamma^{*-1} \mu_\gamma^*$ and $\nu^* = \nu_0 + n$.

The framework in (2.4) is equivalent to (2.2) with $V = R_\phi + (\alpha^{-1} - 1)\mathbb{I}_n$ with $R_\phi = [\rho(s_i, s_j; \phi)]$. We recover posterior samples of Ω by drawing a value of Ω from $p(\Omega | \mathcal{D}, \beta, \Sigma, \mathcal{M}_j)$ for every posterior draw of $\{\beta, \Sigma\}$. This renders itself seamlessly to the Bayesian transfer learning framework described in Section 2.1 provided that V , or $\{\alpha, \phi\}$, is fixed. For GEOAI, we seek to minimize human intervention. Rather than fixing them at one particular value, perhaps gleaned from a spatial variogram that requires human inspection, we use a set of J candidate values $\{\alpha_j, \phi_j\}$ specifying model \mathcal{M}_j for $j = 1, \dots, J$. We now obtain analytical closed forms for $p(\beta, \Sigma | \mathcal{D}, \mathcal{M}_j)$ for each j , as described in Section 2.1, and use Bayesian predictive stacking to evaluate the stacked posterior distribution.

Turning to prediction, let $\mathcal{U} = \{u_1, \dots, u_{n'}\}$ be a finite set of locations where we seek to predict or impute the value of Y based upon an observed $n' \times p$ design matrix $X_{\mathcal{U}}$ associated with the locations in \mathcal{U} . The joint posterior predictive for $Y_{\mathcal{U}}$ and the unobserved latent process $\Omega_{\mathcal{U}} = [\omega(u_i)^T]$ for $i = 1, \dots, n'$, can be recast by integrating out $\{\gamma, \Sigma\}$ from the conditional posterior predictive distribution to yield

$$p(Y_{\mathcal{U}}, \Omega_{\mathcal{U}} | \mathcal{D}) = \int \text{MN}_{n',q}(Y_{\mathcal{U}} | X_{\mathcal{U}}\beta + \Omega_{\mathcal{U}}, (\alpha^{-1} - 1)\mathbb{I}_{n'}, \Sigma) \times \text{MN}_{n',q}(\Omega_{\mathcal{U}} | M_{\mathcal{U}}\Omega, V_{\Omega_{\mathcal{U}}}, \Sigma) \times \text{MNIW}(\gamma, \Sigma | \mu_\gamma^*, V_\gamma^*, \Psi^*, \nu^*) d\gamma d\Sigma, \quad (2.7)$$

where $M_{\mathcal{U}} = \rho_\phi(\mathcal{U}, \mathcal{S})\rho_\phi^{-1}(\mathcal{S}, \mathcal{S})$ and $V_{\Omega_{\mathcal{U}}} = \rho_\phi(\mathcal{U}, \mathcal{U}) - \rho_\phi(\mathcal{U}, \mathcal{S})\rho_\phi^{-1}(\mathcal{S}, \mathcal{S})\rho_\phi(\mathcal{S}, \mathcal{U})$. This is a matrix-variate Student's t $T_{2n',q}(\nu^*, \mu^*, V^*, \Psi^*)$, with degrees of freedom ν^* , location matrix $\mu^* = M\mu_\gamma^*$, row-scale matrix V^* , and column-scale matrix Ψ^* , where $M = \begin{bmatrix} 0 & M_{\mathcal{U}} \\ X_{\mathcal{U}} & M_{\mathcal{U}} \end{bmatrix}$

and $V^* = MV_\gamma^*M^T + V_E$ with $V_E = \begin{bmatrix} V_{\Omega_{\mathcal{U}}} & V_{\Omega_{\mathcal{U}}} \\ V_{\Omega_{\mathcal{U}}} & V_{\Omega_{\mathcal{U}}} + (\alpha^{-1} - 1)\mathbb{I}_{n'} \end{bmatrix}$. See Section S1.1 for

details. While the conditional posterior predictive distributions take the following forms $p(\Omega_{\mathcal{U}} \mid \mathcal{D}, \gamma, \Sigma) = \text{MN}_{n',q}(\Omega_{\mathcal{U}} \mid M_{\mathcal{U}}\Omega, V_{\Omega_{\mathcal{U}}}, \Sigma)$, and $p(Y_{\mathcal{U}} \mid \mathcal{D}, \Omega_{\mathcal{U}}, \gamma, \Sigma) = \text{MN}_{n',q}(Y_{\mathcal{U}} \mid X_{\mathcal{U}}\beta + \Omega_{\mathcal{U}}, (\alpha^{-1} - 1)\mathbb{I}_{n'}, \Sigma)$. Hence, we can proceed with posterior predictive inference by sampling from the closed-form joint predictive distribution or sampling from the conditional distributions. We draw one instance of $\Omega_{\mathcal{U}} \sim p(\Omega_{\mathcal{U}} \mid \mathcal{D}, \gamma, \Sigma)$ for each posterior draw of $\{\gamma, \Sigma\}$ and then draw one value of $Y_{\mathcal{U}} \sim p(Y_{\mathcal{U}} \mid \mathcal{D}, \Omega_{\mathcal{U}}, \gamma, \Sigma)$ for each drawn $\{\Omega_{\mathcal{U}}, \gamma, \Sigma\}$. The resulting samples are exactly drawn from the posterior predictive distribution $p(Y_{\mathcal{U}} \mid \mathcal{D})$.

This tractability is possible if the range decay ϕ and α are fixed. While data can inform about these parameters, they are inconsistently estimable and lead to poorer convergence (Zhang, 2004). Finley et al. (2019) explored K -fold cross-validation, but inference is limited to only one set of values for the parameters. Instead, we pursue exact inference using (2.6) and (2.7) by stacking over different fixed values of $\{\alpha, \phi\}$ using BPS of predictive densities as described in Section 2.2. This minimizes human intervention and enables automation.

For each subset of the data we compute the stacking weights $z_k = \{z_{k,j}\}_{j=1,\dots,J}$ as

$$\max_{z_k \in S_1^J} \frac{1}{n_k} \sum_{i=1}^{n_k} \log \sum_{j=1}^J z_{k,j} p(Y_{k,i} \mid \mathcal{D}_{k,[-l]}, \mathcal{M}_j), \quad (2.8)$$

where $Y_{k,i}$ is the i -th of the n_k rows of $Y_{k,[l]} \in \mathcal{D}_{k,[l]}$ (the l -th fold within the k -th dataset), and $\mathcal{D}_{k,[-l]}$ is the k -th dataset without the l -th fold, with $l = 1, \dots, L$, and L the number of folds for K -fold cross-validation estimates for the expected value of the score (see Section 2.2). The posterior predictive density, $p(Y_{k,i} \mid \mathcal{D}_{k,[-l]}, \mathcal{M}_j)$, is available in closed form as a matrix t distribution, which makes the computation efficient. Leading Equation (2.8) to

$$\max_{z_k \in S_1^J} \frac{1}{n_k} \sum_{i=1}^{n_k} \log \sum_{j=1}^J z_{k,j} \text{T}_{1,q}(Y_{k,i} \mid \nu_{[-l]}^*, \mu_i^*, V_i^*, \Psi_{[-l]}^*), \quad (2.9)$$

where $\nu_{[-l]}^* = \nu_0 + n_{k,[-l]}$, $n_{k,[-l]}$ is the cardinality of $\mathcal{S}_{k,[-l]}$ (which is the set of locations in $\mathcal{D}_{k,[-l]}$), and $\Psi_{[-l]}^* = \Psi_0 + (\alpha_j^{-1} - 1)Y_{k,[-l]}^T Y_{k,[-l]} + m_0^T M_0 m_0 - \mu_{\gamma,[-l]}^{T*} V_{[-l]}^{-1*} \mu_{\gamma,[-l]}^*$. While $V_i^* =$

$M_{y,i}V_\gamma^*M_{y,i}^\top + V_{\Omega_i} + (\alpha_j^{-1} - 1)$, $\mu_i^* = M_{y,i}\mu_{\gamma,[-l]}^*$, which are defined by computing the following auxiliary quantities: $V_{\gamma,[-l]}^{-1*} = \begin{bmatrix} \frac{\alpha_j}{1-\alpha_j}X_{k,[-l]}^\top X_{k,[-l]} + M_0^{-1} & \frac{\alpha_j}{1-\alpha_j}X_{k,[-l]}^\top \\ \frac{\alpha_j}{1-\alpha_j}X_{k,[-l]} & \rho_{\phi_j}^{-1}(\mathcal{S}_{k,[-l]}, \mathcal{S}_{k,[-l]}) + \frac{\alpha_j}{1-\alpha_j}\mathbb{I}_{n_{k,[-l]}} \end{bmatrix}$, $\mu_{\gamma,[-l]}^* = V_{\gamma,[-l]}^* \begin{bmatrix} \frac{\alpha_j}{1-\alpha_j}X_{k,[-l]}^\top Y_{k,[-l]} + m_0 \\ \frac{\alpha_j}{1-\alpha_j}Y_{k,[-l]} \end{bmatrix}$, $M_{y,i} = \begin{bmatrix} X_{k,i} & \rho_{\phi_j}(\mathcal{S}_{k,i}, \mathcal{S}_{k,[-l]})\rho_{\phi_j}^{-1}(\mathcal{S}_{k,[-l]}, \mathcal{S}_{k,[-l]}) \end{bmatrix}$, and $V_{\Omega_i} = \rho_{\phi_j}(\mathcal{S}_{k,i}, \mathcal{S}_{k,i}) - \rho_{\phi_j}(\mathcal{S}_{k,i}, \mathcal{S}_{k,[-l]})\rho_{\phi_j}^{-1}(\mathcal{S}_{k,[-l]}, \mathcal{S}_{k,[-l]})\rho_{\phi_j}(\mathcal{S}_{k,[-l]}, \mathcal{S}_{k,i})$. Note that $\nu_{[-l]}^*$ is scalar, μ_i^* is $(1 \times q)$ row vector, V_i^* is a scalar, and $\Psi_{[-l]}^*$ is $(q \times q)$ matrix. Further details, including derivations and implementation, are supplied in Section S1.1 and Algorithm 1.

For each dataset \mathcal{D}_k , BPS computes: (i) an estimate of the posterior predictive $\hat{p}(\cdot | \mathcal{D}_k) = \sum_{j=1}^J \hat{z}_{k,j} p(\cdot | \mathcal{D}_k, \mathcal{M}_j)$ for $k = 1, \dots, K$ and $j = 1, \dots, J$; and (ii) a set of stacking weights $\hat{z}_k = \{\hat{z}_{k,j}\}_{j=1, \dots, J}$. Once these weights are available, we apply BPS a second time to obtain a weighted average of $\hat{p}(\cdot | \mathcal{D}_k)$ over the k subsets. This DOUBLE BPS of predictive densities seeks weights $w = \{w_k\}_{k=1, \dots, K}$ such that $\hat{w} = \max_{w \in S_1^K} \frac{1}{n} \sum_{i=1}^n \log \sum_{k=1}^K w_k \hat{p}(Y_i | \mathcal{D}_k)$ (see Section S2.1). Once the stacking weights $\hat{w} = \{\hat{w}_k\}_{k=1, \dots, K}$ are obtained, the DOUBLE BPS estimation of any posterior or posterior predictive distributions of interest is obtained from

$$\hat{p}(\cdot | \mathcal{D}) = \sum_{k=1}^K \hat{w}_k \sum_{j=1}^J \hat{z}_{k,j} p(\cdot | \mathcal{D}_k, \mathcal{M}_j) . \quad (2.10)$$

Only posterior predictive distributions are considered to acquire the two sets of stacking weights. Given the weights obtained from double stacking, the stacked posterior distribution is a mixture of finite mixtures. This makes sampling from (2.10) straightforward.

First, the set of stacking weights $\hat{z}_k = \{\hat{z}_{k,j}\}_{j=1, \dots, J}$ obtained using BPS within the subset of the data \mathcal{D}_k , is primarily used to approximate the subset posterior distribution $\hat{p}(\Theta | \mathcal{D}_k) = \sum_{j=1}^J \hat{z}_{k,j} p(\Theta | \mathcal{D}_k, \mathcal{M}_j)$, for each subset $k = 1, \dots, K$. By considering the second set of stacking weights $\hat{w} = \{\hat{w}_k\}_{k=1, \dots, K}$, the stacked full posterior distribution is $\hat{p}(\Theta | \mathcal{D}) = \sum_{k=1}^K \hat{w}_k \hat{p}(\Theta | \mathcal{D}_k) = \sum_{k=1}^K \hat{w}_k \sum_{j=1}^J \hat{z}_{k,j} p(\Theta | \mathcal{D}_k, \mathcal{M}_j)$, where $\Theta = \{\gamma, \Sigma\}$. This is a substantial simplification over meta-kriging (Guhaniyogi and Banerjee, 2018, 2019) that

Algorithm 1 Computing stacking weights within subsets using BPS

Input: Y ($n \times q$ matrix of outcomes), X ($n \times p$ design matrix), \mathcal{S} (coordinates of n locations); $\{m_0, M_0, \Psi_0, \nu_0\}$: Prior parameters; $G_\alpha \times G_\phi$: Grids of $\{\alpha, \phi\}$; n (no. of locations), q (no. of outcomes), p (no. of predictors); K (no. of subsets), J (no. of models), L (no. of folds).

Output: $\hat{z} = \{\hat{z}_k = \{\hat{z}_{k,j}\} : k = 1, \dots, K, j = 1, \dots, J\}$: Stacking weights within subsets; $\{pd_{k,j,i} : k = 1, \dots, K, j = 1, \dots, J, i = 1, \dots, n\}$: point-wise predictive density of Y ; G_{all} : Grid of dimension J , spanned by G_α, G_ϕ

- 1: Partition Y, X, \mathcal{S} into $\mathcal{D}_k = \{Y_k, X_k, \mathcal{S}_k\}$, $k = 1, \dots, K$
 - 2: Store n_k , as cardinality of \mathcal{S}_k ; Compute G_{all} by expanding G_α, G_ϕ
 - 3: **for** $k = 1, \dots, K$ **do Parallel**
 - 4: **for** $j = 1, \dots, J$ **do**
 - 5: Extract $\{\alpha_j, \phi_j\}$ from j -th row of G_{all}
 - 6: Form L folds: $\mathcal{D}_{k,[l]} = \{Y_{k,[l]}, X_{k,[l]}, \mathcal{S}_{k,[l]}\}$ and $\mathcal{D}_{k,[-l]} = \{Y_{k,[-l]}, X_{k,[-l]}, \mathcal{S}_{k,[-l]}\}$
 - 7: Store $n_{k,[-l]}$, as cardinality of $\mathcal{S}_{k,[-l]}$
 - 8: **for** $l = 1, \dots, L$ **do**
 - 9: Compute $R_{\phi_j}([-l]) = \rho_{\phi_j}(\mathcal{S}_{k,[-l]}, \mathcal{S}_{k,[-l]})$, $R_{\phi_j}^{-1}([-l])$ and M_0 for M_0^{-1}
 - 10: Construct $V_{\gamma,[-l]}^{-1\star} = \begin{bmatrix} \frac{\alpha_j}{1-\alpha_j} X_{k,[-l]}^T X_{k,[-l]} + M_0^{-1} & \frac{\alpha_j}{1-\alpha_j} X_{k,[-l]}^T \\ \frac{\alpha_j}{1-\alpha_j} X_{k,[-l]} & R_{\phi_j}^{-1}([-l]) + \frac{\alpha_j}{1-\alpha_j} \mathbb{I}_{n_{k,[-l]}} \end{bmatrix}$
 - 11: Solve for $\mu_{\gamma,[-l]}^*$: $V_{\gamma,[-l]}^{-1\star} \mu_{\gamma,[-l]}^* = \begin{bmatrix} \frac{\alpha_j}{1-\alpha_j} X_{k,[-l]}^T Y_{k,[-l]} + m_0 \\ \frac{\alpha_j}{1-\alpha_j} Y_{k,[-l]} \end{bmatrix}$
 - 12: Calculate $\Psi_{[-l]}^* = \Psi_0 + (\alpha_j^{-1} - 1) Y_{k,[-l]}^T Y_{k,[-l]} + m_0^T M_0 m_0 - \mu_{\gamma,[-l]}^{T\star} V_{[-l]}^{-1\star} \mu_{\gamma,[-l]}^*$
 - 13: Calculate $\nu_{[-l]}^* = \nu_0 + n_{k,[-l]}$
 - 14: **for** $i \in [l]$ **do**
 - 15: Compute $R_{\phi_j}(i) = \rho_{\phi_j}(\mathcal{S}_{k,i}, \mathcal{S}_{k,i})$ and $R_{\phi_j}(i, [-l]) = \rho_{\phi_j}(\mathcal{S}_{k,i}, \mathcal{S}_{k,[-l]})$
 - 16: Calculate $M_i = R_{\phi_j}(i, [-l]) R_{\phi_j}^{-1}([-l])$ and form $M_{y,i} = [X_{k,i} \quad M_i]$
 - 17: Calculate $\mu_i^* = M_{y,i} \mu_{\gamma,[-l]}^*$ and $V_{\Omega_i} = R_{\phi_j}(i) - M_i R_{\phi_j}([-l], i)$
 - 18: Construct $V_{e,i} = V_{\Omega_i} + (\alpha_j^{-1} - 1)$ and $V_i^* = M_{y,i} V_{\gamma,[-l]}^* M_{y,i}^T + V_{e,i}$
 - 19: Compute $pd_{k,j,i} = \mathbb{T}_{1,q}(Y_{k,i} \mid \nu_{[-l]}^*, \mu_i^*, V_i^*, \Psi_{[-l]}^*)$.
 - 20: **end for**
 - 21: **end for**
 - 22: **end for**
 - 23: Solve: $\max_{z_k \in S_1^J} \frac{1}{n_k} \sum_{i=1}^{n_k} \log \sum_{j=1}^J z_{k,j} pd_{k,j,i}$ such that $z_k \in [0, 1]^J : \sum_{j=1}^J z_{k,j} = 1$
 - 24: **end Parallel for**
 - 25: **return** $\{\hat{z}, \{pd_{k,j,i}\}, G_{all}\}$
-

does not require any empirical approximation of posterior or predictive distributions. Again,

the predictive random variable Y_U is recovered from (2.10) as

$$\hat{p}(Y_U \mid \mathcal{D}) = \sum_{k=1}^K \hat{w}_k \sum_{j=1}^J \hat{z}_{k,j} p(Y_U \mid \mathcal{D}_k, \mathcal{M}_j). \quad (2.11)$$

Inferential interest resides with the posterior predictive surface for Ω . Thus, we estimate Ω_U

using $\hat{p}(\Omega_U \mid \mathcal{D}) = \sum_{k=1}^K \hat{w}_k \hat{p}(\Omega_U \mid \mathcal{D}_k)$, where $\hat{p}(\Omega_U \mid \mathcal{D}_k) = \sum_{j=1}^J \hat{z}_{k,j} p(\Omega_U \mid \mathcal{D}_k, \mathcal{M}_j)$.

3 Computer programs and resources

Our subsequent implementations, including all simulations experiments and data analysis, are executed in native R and c++ deploying the `spBPS` package. In particular, all programs used to obtain the ensuing analysis are publicly accessible from the GitHub repository [lucapresicce/Bayesian-Transfer-Learning-for-GeoAI](https://github.com/lucapresicce/Bayesian-Transfer-Learning-for-GeoAI) that links the Rcpp-based `spBPS` package including the main function executing BPS for univariate and multivariate geostatistical models. The reported results are executed on a standard laptop, which runs an Intel Core I7-8750H CPU with 5 available cores for parallel computation and 16 GB of RAM.

We conduct experiments comparing double BPS with spatial meta-kriging (SMK) using a meta-posterior (Minsker et al., 2017) defined as the geometric median of individual posterior distributions based on subsets of the data (as implemented in Guhaniyogi and Banerjee, 2018, 2019). We execute meta-kriging using the `spMvLM` function within the `spBayes` R package that fits a linear model of coregionalization for multivariate spatial data using MCMC (Finley et al., 2015). For parallel implementations of BPS and SMK, we employ R packages `doParallel`, and `foreach` (Corporation and Weston, 2022; Microsoft and Weston, 2022). We map the interpolated spatial surfaces using the `MBA` R package (Finley et al., 2022), while sampling from the matrix-variate normal and t distributions are achieved using the `mvnfast` R package (Fasiolo, 2014). Section S2 in the Supplement provides further details including memory management considerations and efficient solutions to spatial “BIG” data analysis, and sensitivity on the number of data shards K .

4 Simulation experiments

We conduct multiple simulation experiments to evaluate inferential performance of double BPS while underscoring comparisons with SMK. We present a selection of simulation results for multivariate models here and refer the reader to Section S5 for further experiments.

Algorithm 2 Calculating stacking weights between subsets using BPS

Input: $\hat{z} = \{\hat{z}_k = \{\hat{z}_{k,j}\} : k \in \{1, \dots, K\}, j \in \{1, \dots, J\}\}$: Stacking weights within subsets; $\{pd_{k,j,i} : k = 1, \dots, K, j = 1, \dots, J, i = 1, \dots, n\}$: point-wise predictive density of Y ; n, q, p : Number of rows, number of outcomes, and number of predictors; $K, \{n_k : k \in \{1, \dots, K\}\}, J$: Number of subsets, dimension of each subset, and number of competitive models in each subset.

Output: $\hat{w} = \{\hat{w}_k : k = 1, \dots, K\}$: Stacking weights between subsets.

1: Construct $pd = [pd_1^T \cdots pd_K^T]^T$ of dimension $(n \times J)$

$$\text{where } pd_k = \begin{bmatrix} pd_{k,1,1} & \cdots & pd_{k,J,1} \\ \vdots & pd_{k,j,i} & \vdots \\ pd_{k,1,n_k} & \cdots & pd_{k,J,n_k} \end{bmatrix} \text{ of dimension } (n_k \times J)$$

2: **for** $k = 1, \dots, K$ **do**

3: Compute $epd_k = pd \hat{z}_k$ of dimension $(n \times 1)$

4: **end for**

5: Solve convex optimization problem:

$$\max_{w \in S_1^K} \frac{1}{n} \sum_{i=1}^n \log \sum_{k=1}^K w_k epd_{k,i} = \max_{w \in S_1^K} \frac{1}{n} \sum_{i=1}^n \log \sum_{k=1}^K w_k \sum_{j=1}^J \hat{z}_{k,j} pd_{k,j,i}$$

$$\text{where } pd_{k,j,i} = p(Y_{k,i} | \mathcal{D}_{k,[l]}, \mathcal{M}_j) = T_{1,q}(Y_{k,i} | \nu_{[-l]}^*, \mu_i^*, V_i^*, \Psi_{[-l]}^*)$$

$$\text{for } \forall i \notin [-l], l \in \{1, \dots, L\} \text{ and } S_1^K = \{w \in [0, 1]^K : \sum_{k=1}^K w_k = 1\}$$

6: **return** $\hat{w} = \{\hat{w}_k : k \in \{1, \dots, K\}\}$

4.1 Simulation - BPS vs SMK

In the first setting, we consider two synthetic datasets with common structures but distinct sizes using the model (2.4). Both datasets consist of $p = 2$ predictors and $q = 2$ response variables, but different numbers of spatial locations, $n = 5,000$ and $n = 10,000$, respectively.

We generate spatial coordinates from a uniform distribution on $[0, 1]^2$ domain and fix them.

We build the $n \times n$ spatial correlation matrix V over these coordinates using an exponential spatial correlation function with $\phi = 4$ and specify $\Sigma = \mathbb{I}_q$. From these specifications

we generate the $n \times q$ matrix Y from the first equation of (2.4) with fixed $p \times q$ matrix

$$\beta = \begin{bmatrix} -0.75 & 1.85 \\ 0.90 & -1.10 \end{bmatrix}, \text{ a fixed } n \times p \text{ matrix } X \text{ with a first column of ones, representing the}$$

intercept, and $p - 1$ columns of values randomly simulated from a uniform distribution on $[0, 1]$ (emulating standardized predictors), and the proportion of spatial variability $\alpha = 0.8$.

We analyze the simulated datasets using double BPS and SMK in two settings: (i) $K = 10$ and $n = 5,000$; (ii) $K = 10$ and $n = 10,000$; (iii) $K = 5$ and $n = 5,000$; and (iv) $K = 20$

Model	$n = 5000, K = 10$	$n = 5000, K = 5$	$n = 10000, K = 20$	$n = 10000, K = 10$
SMK	51.41	237.23	103.36	446.01
BPS	1.38	7.22	2.24	10.58
Relative ratio	37.25	32.85	46.14	42.15

Table 1: Computational aspects for the different settings, with time in minutes.

and $n = 10,000$. These settings produce subsets of size $n/K \in \{500, 1000\}$. We implement BPS using $J = 9$ candidate models $\mathcal{M}_j, j = 1, \dots, J$, where each model is specified by a set of candidate values for the hyperparameters α_j, ϕ_j in (2.4). These hyperparameters represent the proportion of spatial variability and the parameter(s) of the spatial correlation function, respectively. The set of candidate models is constructed as the set of all possible combinations of values for these hyperparameters. In the subsequent experiments, the grid of models was built using $\alpha \in \{0.70, 0.80, 0.90\}$ and $\phi \in \{3, 4, 5\}$. These values resemble an effective spatial range of $\{0.99, 0.75, 0.60\}$ units, corresponding to 70%, 53%, 42% of the maximum inter-site distance inside the unit square, beyond which the spatial correlation drops below 0.05. Equation (2.5) follows choices in Zhang et al. (2021). Specifically, we set $m_0 = 0_{p \times q}$, $M_0 = 10\mathbb{I}_p$, $\Psi_0 = \mathbb{I}_q$, and $\nu_0 = 3$ in the MNIW joint prior for $\{\gamma, \Sigma\}$ in 2.5. For data analysis, we use an exponential spatial correlation function for $\rho_\phi(\cdot, \cdot)$, which is completely defined conditionally on \mathcal{M}_j , since specifies a value for ϕ . Again, in the conjugate framework, we draw $R = 250$ posterior samples used for inference.

We also apply SMK to the two simulated datasets with the same combinations of n and K as BPS. Unlike BPS, where we stack analytically tractable posteriors over a range of fixed values of spatial covariance kernel parameters, the SMK implementation attempts full Bayesian inference using prior distributions on spatial covariance kernel parameters. We fit the linear model of coregionalization described in Finley et al. (2015) for each subset of the multivariate spatial data using MCMC. The posterior samples from the K subsets are combined using Weiszfeld’s iterative algorithm (Minsker et al., 2017) to produce an estimate of the geometric median of the posterior distributions.

Table 1, which compares the computational speed of double BPS with SMK reveals massive computational gains accrued from BPS. The computational advantage evinced from the relative ratio become more pronounced as the size of the data becomes larger despite the larger subsets. This is explained by the fact that fitting the Gaussian process regression dominates the computation relative to the assimilation of inference from the subsets. If the number of locations explode, then the geometric median of posteriors required by SMK is computationally unfeasible. While SMK offers Bayesian estimates using MCMC for each subset, double BPS avoids MCMC and, hence, issues of convergence.

Importantly, as we see in Figure 2, which depicts estimated response surfaces using BPS and SMK corresponding to $n = 5000$ and $K = 10$, inference from SMK and BPS are practically indistinguishable. The root mean squared prediction errors, RMSPE, reported in Figure 2 denotes the average squared differences between the generated and estimated values of the response and reveals minor discrepancies between BPS and SMK. Section S3 presents results for the other configurations of n and K , each of which reveals that BPS offers practically indistinguishable spatial interpolation from SMK at a fraction of the computational cost.

Figure 3 reports 95% posterior predictive intervals for the response. Again, the empirical coverage is impressive. While we see slightly wider intervals from BPS, this is less pronounced than the underestimation of variability seen with SMK. Moreover, Figure 3 reveals superior MAP estimates for the BPS. Finally, Figure 4 presents the recovery of parameter estimates. As seen in predictive inference, the posterior credible intervals for parameters also deliver practically indistinguishable inference for the two modeling frameworks. In particular, both methods recover the true values for β and Σ , while BPS reconstructs a better point estimate for range parameters ϕ using $\sum_{k=1}^K \hat{w}_k \sum_{j=1}^J \hat{z}_j \phi_j$. Similar conclusions are drawn from other values of n and K explored in Section S5 for univariate responses.

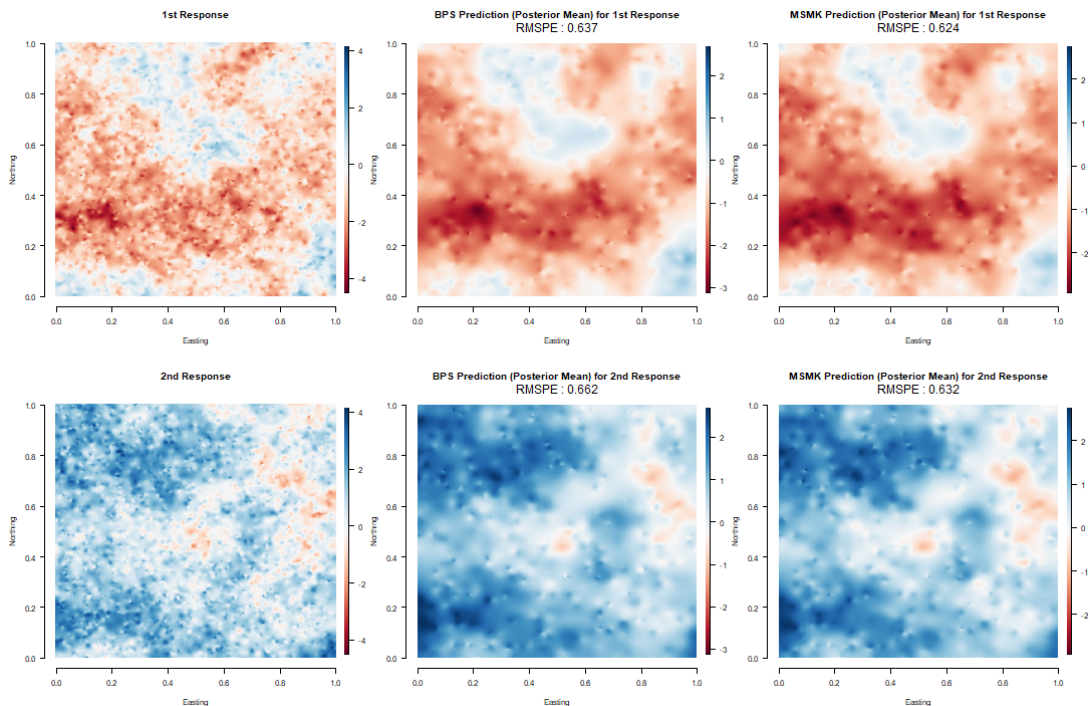


Figure 2: from left to right: comparison between the true generated response surfaces, the surfaces predicted from BPS and SMK (posterior mean), with RMSPE. For $n = 5000$, $K = 10$.

4.2 Simulation - Multivariate Transfer learning

We now consider inferential performance for different misspecified models. As in the earlier example, we generate the $n \times q$ outcome Y using (2.4) with $n = 5,000$, $q = 3$ and $p = 2$, X includes an intercept and $p - 1$ columns generated from a standard uniform distribution

over $[0, 1]$, $\beta = \begin{bmatrix} -0.75 & 1.05 & -0.35 \\ 2.20 & -1.10 & 0.45 \end{bmatrix}$ and $\Sigma = \begin{bmatrix} 2.00 & 0.80 & 0.20 \\ 0.80 & 2.00 & -0.45 \\ 0.20 & -0.45 & 2.00 \end{bmatrix}$. The $n \times n$ spatial

correlation matrix V is specified using an exponential correlation matrix with a fixed range parameter at $\phi = 4$ and $\alpha = 0.8$ to be the strength of spatial dependence.

We analyze the generated data using three different models that assign prior distributions to $\{\beta, \Sigma\}$ with $m_0 = 0_{p \times q}$, $M_0 = 10\mathbb{I}_p$, $\Psi_0 = \mathbb{I}_q$, and $\nu_0 = 3$, but different values of α and ϕ representing (i) well-specified setting with the data generating values $\{\alpha = 0.8, \phi = 4\}$; (ii) moderately misspecified setting with $\{\alpha = 0.45, \phi = 6.63\}$; and (iii) a highly misspecified setting with $\{\alpha = 0.25, \phi = 50\}$. For each setting, we partition the original data into $K = 10$

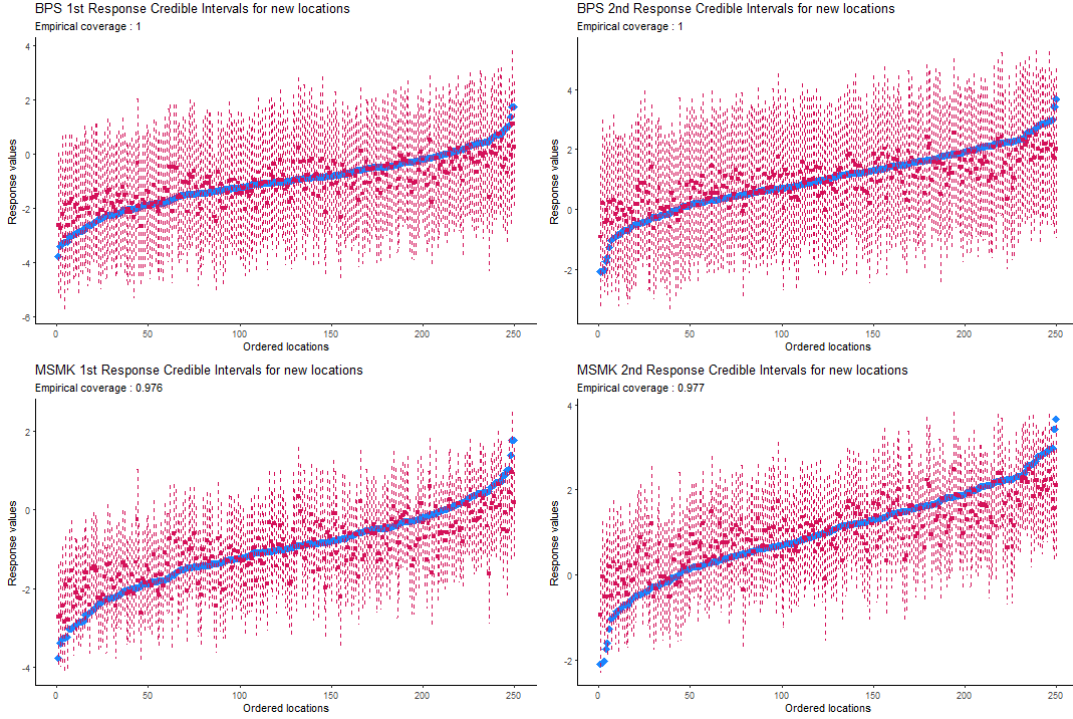


Figure 3: from top to bottom: comparison between posterior predictive intervals for the predicted response from BPS and SMK, with empirical coverage. For $n = 5000$, $K = 10$.

subsets, corresponding to subsets of size 500. We consider $J = 9$ competitive models for BPS and consider $\alpha \in \{0.75, 0.80, 0.85\}$ and $\phi \in \{2, 4, 6\}$ that yields effective spatial ranges in the percentage of maximum point inter-distance of 105%, 53%, 35% respectively.

Here, we display results for the BPS, while graphical results for other settings are available in Section S3. Figure 5 presents a visual comparison between the generated true response and the posterior mean of spatial predictions delivered by BPS. We present the RMSPE along with a set of credible intervals for the parameters relative to the true values. The inferential performance evaluated using the RMSPE as well as the spatially interpolated maps corroborates the effectiveness of BPS. Figure 6 reveals that more than half of the model unknowns are included in the 95% posterior credible interval. Unsurprisingly, inferential performance is weakest for the spatial variance, which is not identifiable from the realized data (Zhang, 2004). Further results on simulation experiments are available in Section S3.

Table 2 presents predictive performance in terms of RMSPE, along with the hyperparameter values corresponding to the different experimental settings. The first three rows cor-

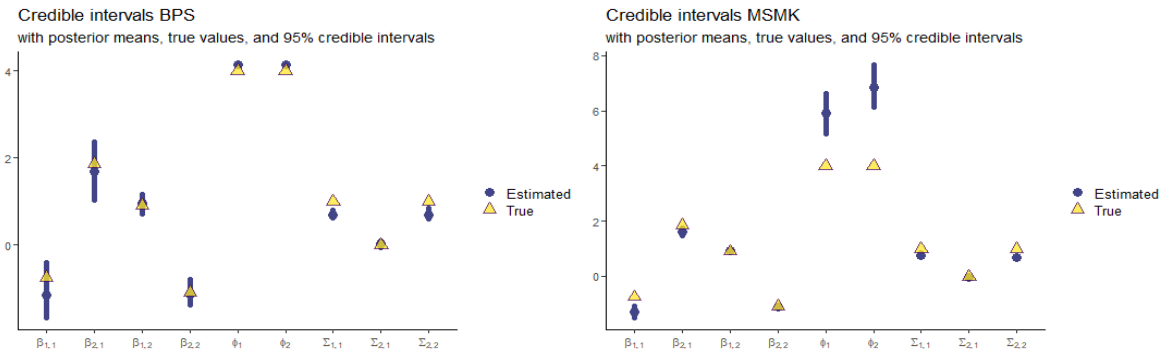


Figure 4: from left to right: comparison between posterior credible intervals for the parameters recovered from BPS and SMK. For $n = 5000$, $K = 10$.

Model	α	ϕ	Average RMSPE
WELL SPECIFIED	0.8	4	0.942
MISSPECIFIED	0.45	6.63	0.963
HIGHLY MISSPECIFIED	0.25	50	1.236
DOUBLE BPS	0.75	4.11	0.900

Table 2: Average RMSPE and specification for each model scenario.

respond to fixed values of $\{\alpha, \phi\}$ in the Bayesian transfer learning approach of Section 2.1. The last row corresponds to BPS when α and ϕ are weighted averages using the stacking weights as described in the last paragraph of Section 4.1. While BPS outperforms transfer learning in terms of RMSPE, some remarks on transfer learning are merited. The transfer learning approach offers slightly better predictive performance than the well-specified model with misspecified data than with well-specified data. This, while somewhat unexpected, is attributed to the estimated response surfaces being practically indistinguishable. Furthermore, transfer learning in even the highly misspecified setting performs competitively. In conclusion, these findings seem to be consistent with theoretical insights offered by Stein (1988) and Stein and Handcock (1989), who theoretically established the ability of Gaussian processes to deliver good predictive performance even for misspecified covariance functions within the in-fill asymptotic paradigm.

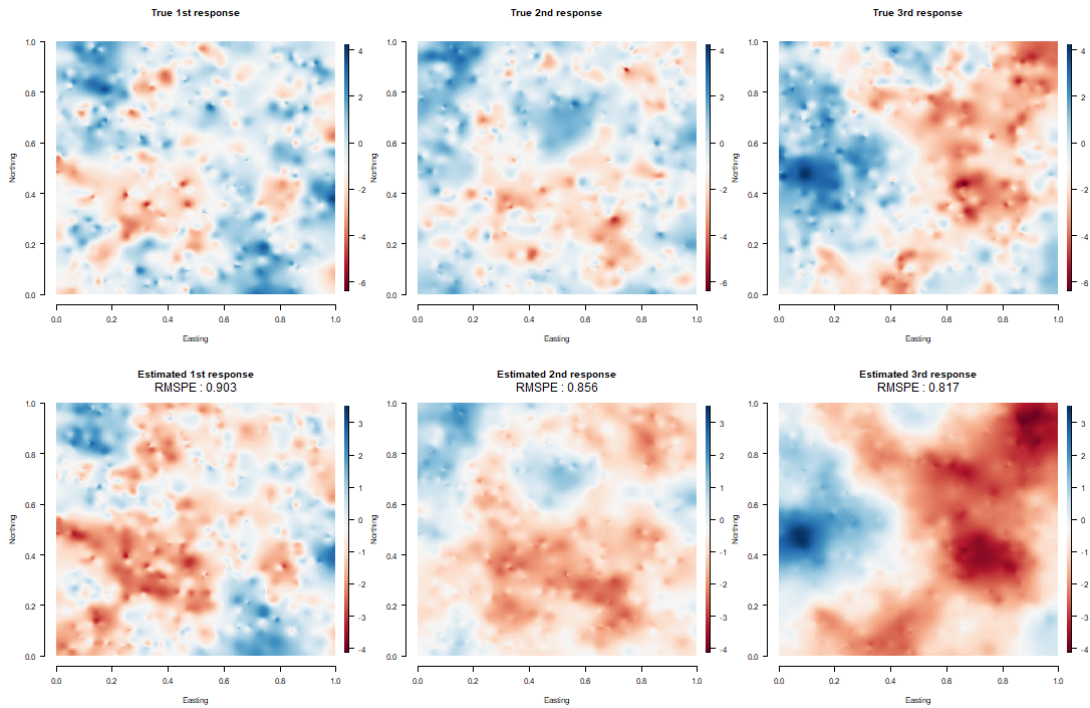


Figure 5: from top to bottom: comparison between the true generated spatial surfaces and the posterior mean surfaces of predictions from BPS, with RMSPE for each outcome.

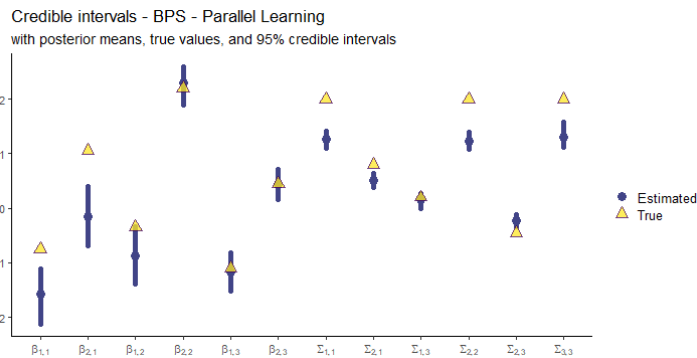


Figure 6: Posterior credible intervals for parameters recovered by BPS, with true parameters in yellow.

5 Application

Global warming and its critical consequences (see [Fisher, 1958](#); [Nicholls, 1989](#); [Friehe et al., 1991](#); [O'Carroll et al., 2019](#)) are increasingly being investigated using machine learning and AI tools that assist in developing predictive global models and formulating data-driven policies. trying to produce faster solutions. The key aspects of global warming are related to global temperature, atmospheric and land surface compositions. We analyze data extracted from NASA's Moderate Resolution Imaging Spectroradiometer (MODIS) platform.

Specifically, we consider as response variables two vegetation indices present in VI data: the normalized difference vegetation index (NDVI); and the red reflectance (RR). Both measure the activity of vegetation on land surfaces and are commonly investigated to help understand biophysical and structural properties of vegetation at global scales (Walther et al., 2018; Jiang et al., 2020; Ai et al., 2020). The predictors comprise an intercept and the solar zenith angle for that location ($p = 2$). The latter depicts the strength of solar irradiation. All the data were collected over a 16-day window in May 2024 and then averaged.

Following other investigations (Zhang and Banerjee, 2022), we report our analysis on all spatially dependent variables in the logarithmic scale. Machine generated exploratory data analysis (EDA) is described in Sections S6 and S7 to guide grid settings for α, ϕ . Based on Section S7, we set $\alpha \in \{0.825, 0.909\}$, and $\phi \in \{0.049, 0.067\}$ respectively. We specify $\{\gamma, \Sigma\}$ in (2.5) using $m_0 = 0_{p \times q}$, $M_0 = 10\mathbb{I}_p$, $\Psi_0 = \mathbb{I}_q$, $\nu_0 = 3$, and finally we opt for an exponential spatial covariance function. The analyzed data consists of 1,002,500 observed spatial locations across the world, of which $n = 1,000,000$ locations are used as training data and the rest are withheld for evaluating predictive performance. Following insights from Section S3.3, we fix the subset size at $n_k \in \{250, 500\}$, leading to a number of subsets $K \in \{4,000, 2,000\}$ respectively. We use a random scheme to form the partition of the dataset and present results when $K = 2,000$ and in Table 3 for $K = 4,000$.

The multivariate model developed in Section 2.3 with NDVI and RR comprising the $q = 2$ columns of Y . Figures 7 and 8 illustrate maps corresponding to NDVI and RR, respectively, using $K = 2,000$ subsets. The top left panel in each figure presents the spatially interpolated map of the training data for the respective responses. The interpolated maps for the test data are displayed in the top right panel of the respective figures. These maps reveal pronounced spatial variation, where the darker shades of green in NDVI represent higher values of detected biomass, while lighter shades of brown represent low biomass. Conversely for RR, warmer colors in the red spectrum represent higher reflectance.

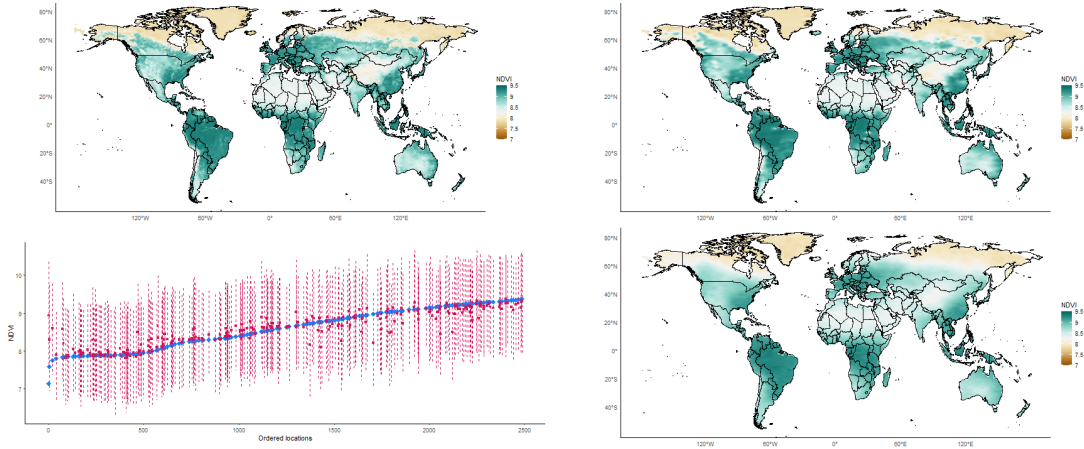


Figure 7: Left to right: Maps for training data (top left), test data (top right) and predicted surface (bottom right) for NDVI. Empirical coverage for held-out values are in the bottom left. Results correspond to $K = 2,000$.

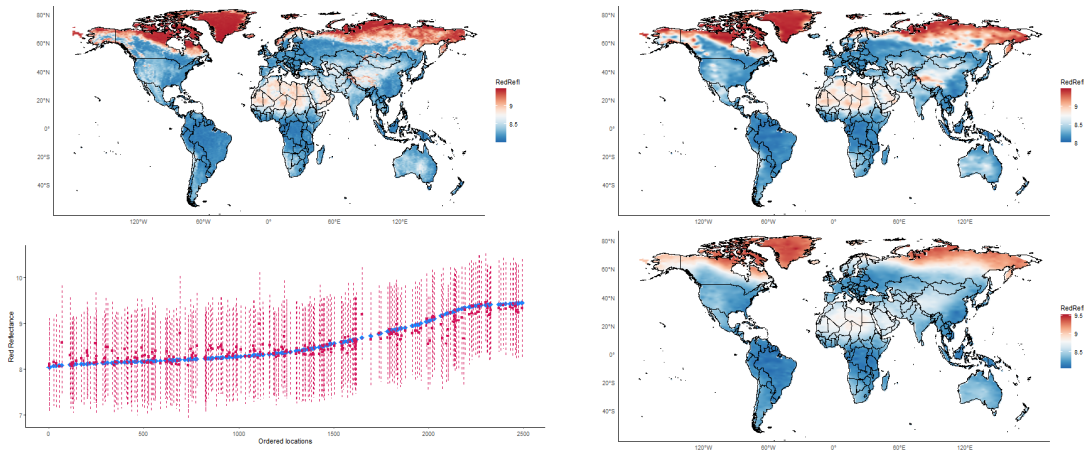


Figure 8: Left to right: Maps for training data (top left), test data (top right) and predicted surface (bottom right) for RR. Empirical coverage for held-out values of outcomes (bottom left). Results correspond to $K = 2,000$.

Figures 7 and 8 show results from double BPS. Maps of interpolated posterior means and predicted responses are displayed in the bottom right of the respective figures. The BPS interpolated maps are almost indistinguishable from the true surface (top right). This suggests that the automated BPS effectively, perhaps even strikingly, recovers the spatial patterns in spite of the modeling simplifications over more elaborate statistical models (Banerjee, 2020; Zhang et al., 2021). Moreover, the double BPS behaves well in terms of predictive performance and uncertainty quantification for both values of K considered. It achieves an RMSPE of $(0.206, 0.159)$ when $K = 2,000$, and $(0.241, 0.197)$ with $K = 4,000$ subsets for NDVI and RR respectively. This is significantly lower (by almost 100%) than the standard Bayesian conjugate multivariate linear model, which produces RMSPE of $(0.474, 0.439)$ for the two

	Conjugate Linear model	BPS ($K = 4,000$)	BPS ($K = 2,000$)
$\beta_{0,\text{NDVI}}$	34.495 (34.392, 34.601)	1.364 (-1.039, 3.907)	1.767 (-0.422, 3.917)
$\beta_{1,\text{NDVI}}$	-2.708 (-2.719, -2.697)	0.744 (0.478, 0.998)	0.707 (0.485, 0.939)
$\beta_{0,\text{RR}}$	-16.924 (-17.014, -16.837)	-0.418 (-2.470, 1.710)	-0.562 (-2.187, 0.962)
$\beta_{1,\text{RR}}$	2.664 (2.655, 2.674)	0.945 (0.726, 1.158)	0.959 (0.795, 1.139)
Σ_{NDVI}	0.221 (0.220, 0.221)	0.182 (0.130, 0.257)	0.119 (0.099, 0.146)
$\Sigma_{\text{NDVI,RR}}$	-0.167 (-0.168, -0.166)	-0.114 (-0.173, -0.079)	-0.076 (-0.094, -0.061)
Σ_{RR}	0.155 (0.154, 0.155)	0.115 (0.082, 0.170)	0.077 (0.062, 0.092)
$\varrho_{\text{NDVI,RR}}$	-0.921 (-0.928, -0.915)	-0.816 (-0.874, -0.706)	-0.844 (-0.880, -0.795)
RMSPE	[0.474, 0.404, 0.439]	[0.241, 0.197, 0.219]	[0.206, 0.159, 0.183]
Time	12	21	81

Table 3: Vegetation Index data analysis parameter estimates, RMSPE, and computing time in minutes for candidate models. Parameter posterior summary 50 (2.5, 97.5) percentiles. Root mean square prediction error(s) presentation [NDVI, red reflectance, average].

vegetation indexes, respectively. The predictive 95% credible intervals when $K = 2,000$ for both responses are shown in the bottom left of Figures 7 and 8, respectively.

Table 3 compares BPS with the Bayesian conjugate linear model, which does not take into account spatial variability for $K \in \{4,000, 2,000\}$. The notably higher magnitudes of the intercepts in the non-spatial linear model are unsurprising as the random effects in the spatial models absorb much of the variation in the intercepts. The solar zenith angle is positively associated with RR and negatively associated with NDVI in the non-spatial model. This, too, is expected since higher levels of solar irradiation are associated with higher red reflectance and with more arid regions with less vegetation. However, the spatial models reveal that the slope for NDVI is also significantly positive with solar irradiation after the spatial effects have absorbed previously unaccounted latent or lurking factors that might have contributed to the negative slopes in the non-spatial model. Estimates of ϱ_{NDVI} and ϱ_{RR} reveal a well-documented negative association between the two responses. Indeed, the spatial patterns in these indices are almost the reverse of each other as revealed in Figures 7 and 8. The conjugate Bayesian linear model estimates higher negative correlation, while BPS tends to underestimate it, considerably so as n_k decreases.

Recalling that all the analyses are produced on a personal laptop (with just 5 physical cores) with minimal human intervention, the total run time of only 21 minutes with $K =$

4,000 and 81 minutes with $K = 2,000$ are impressive confirm the quadratic dependence of the partition size discussed in Section S6. Moreover, the strong dependence on the number of J competitive models assessed is worth noting. Here $J = 4$ while in Section S6 $J = 3$. This suggests a marginal computational burden for each competitive model.

6 Discussion

This manuscript devises a statistical modeling component for an artificially intelligent geospatial system (GEOAI) tailored to analyze massive datasets with minimal human intervention. The contribution harnesses analytically accessible multivariate statistical distributions in conjunction with Bayesian predictive stacking to deliver rapid inference on multivariate processes and circumventing iterative algorithms that require, often extensive, human tuning or control. Our proposed GeoSpatial AI system is capable of handling truly massive amounts of spatial data that preclude accessibility even on high performance CPU architectures and we develop Bayesian transfer learning using double Bayesian predictive stacking.

A few additional remarks are warranted. The development here has been elucidated with a hierarchical matrix-variate spatial process framework. While modeling simplifications have been introduced to minimize human intervention, we wish to emphasize that the BPS seamlessly applies to more versatile but analytically intractable models. First, for spatially misaligned multivariate data where not all the variables may have been observed over the same set of locations, we encounter missing entries in Y but are still able to deliver analytically tractable closed-form distribution theory (Zhang and Banerjee, 2022). Second, should users wish to explore more complex models with unknown $\{\alpha, \phi\}$ or work with alternate multivariate models, then we can implement full Bayesian inference (now using MCMC, Variational Bayes or Laplace approximations) on each subset and invoke BPS to pool across the subsets of the data. Time for analyzing each subset increase due to model complexity, but scaling inference to massive datasets is still enabled by BPS—and that too with consider-

able efficiency over alternate divide-and-conquer approaches such as the geometric median, or GM, of posteriors (used in meta-kriging developed by [Guhaniyogi and Banerjee, 2018](#)).

A preliminary examination of [Section 2.3](#) reveals that posterior inference is conceptualized as a “mixture of mixtures”. Following [Yao et al. \(2018\)](#), we prefer stacking to fitting a mixture model because the former is numerically robust and requires almost no human tuning. Moreover, the structure of mixture-of-mixtures conceptually resembles the “Mixture of Experts” (MOE) that are adopted by AI platforms such as GPT-4 and Mistral. Disseminating our proposed product with our accompanying software, which is currently being migrated to R, is expected to significantly boost GEOSPATIAL AI systems. Future directions will also explore perceived potential of BPS as a feeder for emerging amortized inference methods ([Ganguly et al., 2023](#); [Zammit-Mangion et al., 2024](#); [Sainsbury-Dale et al., 2024](#)) to achieve Bayesian inference. Rapid delivery of posterior estimates of the entire spatial process from BPS will amount to more training data for amortized neural learners that can result in accelerated tuning for subsequent Bayesian inference. We do not see our proposed approach as a competitor to, but rather as supplementary to amortized neural inference. Such developments will be pursued as future research. We also seek to expand and fully investigate automated double BPS using Markovian graphical structures across data subsets to further expedite and improve GEOSPATIAL AI systems.

Supplementary Materials

The online supplement includes additional derivations and details on matrix-variate distributions ([Section S1](#)), computational details and algorithms ([Section S2](#)), additional simulation experiment results ([Section S5](#)), details on accelerated BPS for univariate spatial data ([Section S4](#)) and analysis of an additional dataset on sea surface temperature ([Section S6](#)). [Section S7](#) outlines automated computation of model hyperparameters without human in-

tervention. Computer programs to reproduce all experiments and data analysis are publicly accessible from the GitHub repository [lucapresicce/Bayesian-Transfer-Learning-for-GEOAI](https://github.com/lucapresicce/Bayesian-Transfer-Learning-for-GEOAI)

References

- Ai, J., Xiao, S., Feng, H., Wang, H., Jia, G., and Hu, Y. (2020). A global terrestrial ecosystem respiration dataset (2001-2010) estimated with MODIS land surface temperature and vegetation indices. *Big Earth Data*, 4(2):142–152.
- Banerjee, S. (2017). High-dimensional Bayesian geostatistics. *Bayesian Analysis*, 12(2):583–614.
- Banerjee, S. (2020). Modeling massive spatial datasets using a conjugate Bayesian linear modeling framework. *Spatial Statistics*, 37:100417. *Frontiers in Spatial and Spatio-temporal Research*.
- Banerjee, S. (2022). Discussion of “Measuring housing vitality from multi-source big data and machine learning”. *Journal of the American Statistical Association*, 117(539):1063–1065.
- Banerjee, S., Carlin, B. P., and Gelfand, A. E. (2015). *Hierarchical modeling and analysis for Spatial Data*. Chapman & Hall/CRC.
- Banerjee, S., Gelfand, A. E., Finley, A. O., and Sang, H. (2008). Gaussian predictive process models for large spatial data sets. *Journal of the Royal Statistical Society: Series B (Statistical Methodology)*, 70(4):825–848.
- Bell, M. L., Dominici, F., and Samet, J. M. (2005). A meta-analysis of time-series studies of ozone and mortality with comparison to the national morbidity, mortality, and air pollution study. *Epidemiology*, 16(4):436–45.
- Breiman, L. (1996). Stacked regressions. *Machine Learning*, 24(1):49–64.

- Cao, J., Kang, M., Jimenez, F., Sang, H., Schaefer, F. T., and Katzfuss, M. (2023). Variational sparse inverse cholesky approximation for latent Gaussian processes via double kullback-leibler minimization. In Krause, A., Brunskill, E., Cho, K., Engelhardt, B., Sabato, S., and Scarlett, J., editors, *Proceedings of the 40th International Conference on Machine Learning*, volume 202 of *Proceedings of Machine Learning Research*, pages 3559–3576. PMLR.
- Corporation, M. and Weston, S. (2022). *doParallel: Foreach parallel adaptor for the 'parallel' Package*. R package version 1.0.17.
- Cressie, N. (1993). *Statistics For Spatial Data, Revised Edition*. John Wiley & Sons.
- Cressie, N. and Johannesson, G. (2008). Fixed rank kriging for very large spatial data sets. *Journal of the Royal Statistical Society: Series B (Statistical Methodology)*, 70(1):209–226.
- Cressie, N. and Wikle, C. K. (2011). *Statistics for spatio-temporal data*. Wiley.
- Datta, A., Banerjee, S., Finley, A. O., and Gelfand, A. E. (2016). Hierarchical nearest-neighbor Gaussian process models for large geostatistical datasets. *Journal of the American Statistical Association*, 111(514):800–812.
- Dey, D., Datta, A., and Banerjee, S. (2022). Graphical Gaussian process models for highly multivariate spatial data. *Biometrika*, 109(4):993–1014.
- Fasiolo, M. (2014). *An introduction to mvnfast*. University of Bristol. R package version 0.2.8.
- Finley, A., Banerjee, S., and Øyvind Hjelle (2022). *MBA: Multilevel B-spline approximation*. R package version 0.1-0.
- Finley, A. O., Banerjee, S., and Gelfand, A. E. (2015). spBayes for large univariate and multivariate point-referenced spatio-temporal data models. *Journal of Statistical Software*, 63(13):1–28.

- Finley, A. O., Datta, A., Cook, B. D., Morton, D. C., Andersen, H.-E., and Banerjee, S. (2019). Efficient algorithms for Bayesian nearest neighbor Gaussian processes. *Journal of Computational and Graphical Statistics*, 28(2):401–414.
- Fisher, E. L. (1958). Hurricanes and the sea-surface temperature field. *Journal of Atmospheric Sciences*, 15(3):328–333.
- Friehe, C. A., Shaw, W. J., Rogers, D. P., Davidson, K. L., Large, W. G., Stage, S. A., Crescenti, G. H., Khalsa, S. J. S., Greenhut, G. K., and Li, F. (1991). Air-sea fluxes and surface layer turbulence around a sea surface temperature front. *Journal of Geophysical Research: Oceans*, 96(C5):8593–8609.
- Fu, A., Narasimhan, B., and Boyd, S. (2020). CVXR: An R package for disciplined convex optimization. *Journal of Statistical Software*, 94(14):1–34.
- Ganguly, A., Jain, S., and Watchareeruetai, U. (2023). Amortized variational inference: A systematic review. *Journal of Artificial Intelligence Research*, 78:167–215.
- Gelfand, A. E., Diggle, P., Guttorp, P., and Fuentes, M. (2010). *Handbook of Spatial Statistics*. Taylor & Francis.
- Georganos, S., Grippa, T., Gadiaga, A. N., Linard, C., Lennert, M., Vanhuyse, S., Mboga, N., Wolff, E., and Kalogirou, S. (2021). Geographical random forests: a spatial extension of the random forest algorithm to address spatial heterogeneity in remote sensing and population modelling. *Geocarto International*, 36(2):121–136.
- Gneiting, T. and Raftery, A. E. (2007). Strictly proper scoring rules, prediction, and estimation. *Journal of the American Statistical Association*, 102(477):359–378.
- Grant, M. and Boyd, S. (2008). Graph implementations for nonsmooth convex programs. In Blondel, V., Boyd, S., and Kimura, H., editors, *Recent Advances in Learning and Control*, Lecture Notes in Control and Information Sciences, pages 95–110. Springer-Verlag Limited.

- Guhaniyogi, R. and Banerjee, S. (2018). Meta-kriging: Scalable Bayesian modeling and inference for massive spatial datasets. *Technometrics*, 60(4):430–444.
- Guhaniyogi, R. and Banerjee, S. (2019). Multivariate spatial meta kriging. *Statistics & Probability Letters*, 144:3–8.
- Guhaniyogi, R., Li, C., Savitsky, T. D., and Srivastava, S. (2019). A divide-and-conquer Bayesian approach to large-scale kriging. *arXiv preprint*, page arXiv:1712.09767.
- Heaton, M. J., Datta, A., Finley, A. O., Furrer, R., Guinness, J., Guhaniyogi, R., Gerber, F., Gramacy, R. B., Hammerling, D. M., Katzfuss, M., Lindgren, F., Nychka, D. W., Sun, F., and Zammit-Mangion, A. (2017). A case study competition among methods for analyzing large spatial data. *Journal of Agricultural, Biological, and Environmental Statistics*, 24(3):398–425.
- Jiang, Y., Zhou, L., and Raghavendra, A. (2020). Observed changes in fire patterns and possible drivers over central africa. *Environmental Research Letters*, 15(9):0940b8.
- Kang, J., Johnson, T. D., Nichols, T. E., and Wager, T. D. (2011). Meta analysis of functional neuroimaging data via Bayesian spatial point processes. *Journal of the American Statistical Association*, 106(493):124–134.
- Katzfuss, M. (2017). A multi-resolution approximation for massive spatial datasets. *Journal of the American Statistical Association*, 112(517):201–214.
- Katzfuss, M. and Guinness, J. (2021). A general framework for Vecchia approximations of Gaussian processes. *Statistical Science*, 36(1):124–141.
- Lindgren, F., Rue, H., and Lindström, J. (2011). An explicit link between Gaussian fields and Gaussian Markov random fields: The stochastic partial differential equation approach. *Journal of the Royal Statistical Society Series B: Statistical Methodology*, 73(4):423–498.

- Microsoft and Weston, S. (2022). *Foreach: Provides foreach looping construct*. R package version 1.5.2.
- Minsker, S., Srivastava, S., Lin, L., and Dunson, D. B. (2017). Robust and scalable Bayes via a median of subset posterior measures. *Journal of Machine Learning Research*, 18(124):1–40.
- Nicholls, N. (1989). Sea surface temperatures and australian winter rainfall. *Journal of Climate*, 2(9):965–973.
- Nychka, D., Bandyopadhyay, S., Hammerling, D., Lindgren, F., and Sain, S. (2015). A multiresolution gaussian process model for the analysis of large spatial datasets. *Journal of Computational and Graphical Statistics*, 24(2):579–599.
- O’Carroll, A. G., Armstrong, E. M., Beggs, H. M., Bouali, M., Casey, K. S., Corlett, G. K., Dash, P., Donlon, C. J., Gentemann, C. L., Høyer, J. L., Ignatov, A., Kabobah, K., Kachi, M., Kurihara, Y., Karagali, I., Maturi, E., Merchant, C. J., Marullo, S., Minnett, P. J., Pennybacker, M., Ramakrishnan, B., Ramsankaran, R., Santoleri, R., Sunder, S., Saux Picart, S., Vázquez-Cuervo, J., and Wimmer, W. (2019). Observational needs of sea surface temperature. *Frontiers in Marine Science*, 6(420):1–27.
- Parmigiani, G. (2002). *Modeling in Medical Decision Making: A Bayesian Approach*. John Wiley & Sons, Hoboken, NJ.
- Quiñonero-Candela, J. and Rasmussen, C. E. (2005). A unifying view of sparse approximate gaussian process regression. *Journal of Machine Learning Research*, 6(65):1939–1959.
- Ren, Q., Banerjee, S., Finley, A. O., and Hodges, J. S. (2011). Variational bayesian methods for spatial data analysis. *Computational Statistics & Data Analysis*, 55(12):3197–3217.
- Rendell, L. J., Adam M. Johansen, A. L., and Whiteley, N. (2021). Global consensus Monte Carlo. *Journal of Computational and Graphical Statistics*, 30(2):249–259.

- Rue, H., Martino, S., and Chopin, N. (2009). Approximate Bayesian inference for latent Gaussian models by using integrated nested Laplace approximations. *Journal of the Royal Statistical Society Series B: Statistical Methodology*, 71(2):319–392.
- Saha, A., Basu, S., and Datta, A. (2023). Random forests for spatially dependent data. *Journal of the American Statistical Association*, 118(541):665–683.
- Sainsbury-Dale, M., Zammit-Mangion, A., Richards, J., and Huser, R. (2024). Neural bayes estimators for irregular spatial data using graph neural networks.
- Sauer, A., Cooper, A., and Gramacy, R. B. (2023a). Vecchia-approximated deep gaussian processes for computer experiments. *Journal of Computational and Graphical Statistics*, 32(3):824–837.
- Sauer, A., Gramacy, R. B., and Higdon, D. (2023b). Active learning for deep gaussian process surrogates. *Technometrics*, 65(1):4–18.
- Scott, S. L., Alexander W. Blocker, F. V. B., Chipman, H. A., George, E. I., and McCulloch, R. E. (2016). Bayes and big data: the consensus Monte Carlo algorithm. *International Journal of Management Science and Engineering Management*, 11(2):78–88.
- Srivastava, S., Cevher, V., Dinh, Q., and Dunson, D. (2015). WASP: Scalable Bayes via barycenters of subset posteriors. In Lebanon, G. and Vishwanathan, S. V. N., editors, *Proceedings of the Eighteenth International Conference on Artificial Intelligence and Statistics*, volume 38 of *Proceedings of Machine Learning Research*, pages 912–920, San Diego, California, USA. PMLR.
- Stein, M. L. (1988). Asymptotically efficient prediction of a random field with a misspecified covariance function. *The Annals of Statistics*, 16(1):55–63.
- Stein, M. L. (1999). *Interpolation of spatial data*. Springer Series in Statistics. Springer-Verlag, New York. Some theory for Kriging.

- Stein, M. L. and Handcock, M. S. (1989). Some asymptotic properties of kriging when the covariance function is misspecified. *Mathematical Geology*, 21:171–190.
- Talebi, H., Peeters, L. J. M., Otto, A., and Tolosana-Delgado, R. (2022). A truly spatial random forests algorithm for geoscience data analysis and modelling. *Mathematical Geosciences*, 54(1):1–22.
- Tang, W., Zhang, L., and Banerjee, S. (2021). On identifiability and consistency of the nugget in Gaussian spatial process models. *Journal of the Royal Statistical Society: Series B (Statistical Methodology)*, 83(5):1044–1070.
- Vecchia, A. V. (1988). Estimation and model identification for continuous spatial processes. *Journal of the Royal Statistical society, Series B*, 50:297–312.
- Walther, S., Guanter, L., Heim, B., Jung, M., Duveiller, G., Wolanin, A., and Sachs, T. (2018). Assessing the dynamics of vegetation productivity in circumpolar regions with different satellite indicators of greenness and photosynthesis. *Biogeosciences*, 15(20):6221–6256.
- Wikle, C. K. (2010). Low-rank representations for spatial processes. *Handbook of Spatial Statistics*, pages 107–118. Gelfand, A. E., Diggle, P., Fuentes, M. and Guttorp, P., editors, Chapman and Hall/CRC, pp. 107-118.
- Wikle, C. K. and Zammit-Mangion, A. (2023). Statistical deep learning for spatial and spatiotemporal data. *Annual Review of Statistics and Its Application*, 10(Volume 10, 2023):247–270.
- Wolpert, D. H. (1992). Stacked generalization. *Neural Networks*, 5(2):241–259.
- Wu, L., Pleiss, G., and Cunningham, J. P. (2022). Variational nearest neighbor Gaussian process. In Chaudhuri, K., Jegelka, S., Song, L., Szepesvari, C., Niu, G., and Sabato, S.,

- editors, *Proceedings of the 39th International Conference on Machine Learning*, volume 162 of *Proceedings of Machine Learning Research*, pages 24114–24130. PMLR.
- Yao, Y., Vehtari, A., Simpson, D., and Gelman, A. (2018). Using stacking to average Bayesian predictive distributions (with discussion). *Bayesian Analysis*, 13(3):917–1007.
- Zammit-Mangion, A., Ng, T. L. J., Vu, Q., and Filippone, M. (2022). Deep compositional spatial models. *Journal of the American Statistical Association*, 117(540):1787–1808.
- Zammit-Mangion, A., Sainsbury-Dale, M., and Huser, R. (2024). Neural methods for amortised inference.
- Zhang, H. (2004). Inconsistent estimation and asymptotically equal interpolations in model-based geostatistics. *Journal of the American Statistical Association*, 99(465):250–261.
- Zhang, L. and Banerjee, S. (2022). Spatial factor modeling: A Bayesian matrix-normal approach for misaligned data. *Biometrics*, 78(2):560–573.
- Zhang, L., Banerjee, S., and Finley, A. O. (2021). High-dimensional multivariate geostatistics: A Bayesian matrix-normal approach. *Environmetrics*, 32(4):e2675.
- Zhou, Y., Xue, L., Shi, Z., Wu, L., and Fan, J. (2022). Measuring housing vitality from multi-source big data and machine learning. *Journal of the American Statistical Association*, 117(539):1045–1059.

Supplemental material: Bayesian Transfer Learning for Artificially Intelligent Geospatial Systems: A Predictive Stacking Approach

Organization of the supplemental material

The supplementary material is organized as follows. In Section [S1](#), we present the distributional results; Section [S1.1](#) provides the analytical derivation of the posterior predictive distribution in Equation (2.7) of Section [2.3](#), applicable to the spatial latent regression model in Equation (2.4). Section [S2](#) contains the remaining computational details we examined. In addition, in Section [S2.2](#) we offer a comprehensive discussion of the theoretical complexity, including comparisons with other algorithmic approaches. Moreover, in Section [S2.1](#) we explicitly derive the objective function of the optimization problems described in Section [2.3](#) along with the double Bayesian stacking. Section [S2.4](#) offers an innovative posterior sampling procedure for the regression coefficients β , which allows for improved memory allocation. Similarly, in Section [S2.3](#) we introduce an alternative algorithm for subset stacking, which is extremely efficient in large-scale problems. Finally, Section [S3](#) includes additional plots referring to the simulation studies presented in Section [4](#) of the main paper. Section [S3.3](#) concludes the multivariate geospatial investigations by analyzing the sensitivity to subset dimension. In addition, in Section [S4](#) we provide the content described in Section [2.3](#) but for univariate GeoAI systems instead, subsequently followed by simulations in Section [S5](#). The investigation of univariate models concludes with a climate science data analysis in Section [S6](#). Section [S7](#) concludes the supplemental material by providing details on explanatory data analyses related to the data applications of Section [5](#), and Section [S6](#).

S1 Distribution theory

S1.1 Posterior and predictive matrix-variate T distributions

The joint posterior predictive for $Y_{\mathcal{U}}$ and the unobserved latent process $\Omega_{\mathcal{U}}$, can be recast by integrating out $\{\gamma, \Sigma\}$ from the joint conditional posterior predictive, that is

$$p(Y_{\mathcal{U}}, \Omega_{\mathcal{U}} | \mathcal{D}) = \int \text{MN}_{n',q}(Y_{\mathcal{U}} | X_{\mathcal{U}}\beta + \Omega_{\mathcal{U}}, (\alpha^{-1} - 1)\mathbb{I}_{n'}, \Sigma) \times \text{MN}_{n',q}(\Omega_{\mathcal{U}} | M_{\mathcal{U}}\Omega, V_{\Omega_{\mathcal{U}}}, \Sigma) \\ \times \text{MNIW}(\gamma, \Sigma | \mu_{\gamma}^*, V_{\gamma}^*, \Psi^*, \nu^*) d\gamma d\Sigma,$$

where $M_{\mathcal{U}} = \rho_{\phi}(\mathcal{U}, \mathcal{S})\rho_{\phi}^{-1}(\mathcal{S}, \mathcal{S})$ and $V_{\Omega_{\mathcal{U}}} = \rho_{\phi}(\mathcal{U}, \mathcal{U}) - \rho_{\phi}(\mathcal{U}, \mathcal{S})\rho_{\phi}^{-1}(\mathcal{S}, \mathcal{S})\rho_{\phi}(\mathcal{S}, \mathcal{U})$. We derive $p(\Omega_{\mathcal{U}}, Y_{\mathcal{U}} | \Sigma, \mathcal{D})$ by avoiding direct integration with respect to γ using the following augmented linear system

$$\underbrace{\begin{bmatrix} \Omega_{\mathcal{U}} \\ Y_{\mathcal{U}} \end{bmatrix}}_{\Upsilon} = \underbrace{\begin{bmatrix} \mathbf{0}_{n' \times q} & M_{\mathcal{U}} \\ X_{\mathcal{U}} & M_{\mathcal{U}} \end{bmatrix}}_M \underbrace{\begin{bmatrix} \beta \\ \Omega \end{bmatrix}}_{\gamma} + \underbrace{\begin{bmatrix} E_{Y_{\mathcal{U}}} \\ E_{\Omega_{\mathcal{U}}} \end{bmatrix}}_E, \quad E \sim \text{MN}_{2n',q}(0_{2n' \times q}, V_E, \Sigma), \quad (\text{S1})$$

where $V_E = \begin{bmatrix} V_{\Omega_{\mathcal{U}}} & V_{\Omega_{\mathcal{U}}} \\ V_{\Omega_{\mathcal{U}}} & (\alpha^{-1} - 1)\mathbb{I}_{n'} + V_{\Omega_{\mathcal{U}}} \end{bmatrix}$. We write the posterior distribution $p(\gamma | \mathcal{D})$ in Equation (2.6) as a linear equation, $\gamma = \mu_{\gamma}^* + E_{\gamma}$, with $E_{\gamma} \sim \text{MN}_{n',q}(0, V_{\gamma}^*, \Sigma)$, where E and E_{γ} are independent of each other. Then,

$$\Upsilon = M\mu_{\gamma}^* + ME_{\gamma} + E \sim \text{MN}_{2n',q}(M\mu_{\gamma}^*, V^*, \Sigma), \quad (\text{S2})$$

where $V^* = MV_{\gamma}^*M^{\top} + V_E$. This yields $p(\Upsilon | \Sigma, \mathcal{D}) = p(\Omega_{\mathcal{U}}, Y_{\mathcal{U}} | \Sigma, \mathcal{D})$ as the closed-form joint predictive distribution by integrating out Σ from $p(\Omega_{\mathcal{U}}, Y_{\mathcal{U}} | \Sigma, \mathcal{D})p(\Sigma | \mathcal{D})$ to get

$$\int \text{MNIW}(\Omega_{\mathcal{U}}, Y_{\mathcal{U}}, \Sigma | M\mu_{\gamma}^*, V^*, \Psi^*, \nu^*) d\Sigma = \text{T}_{2n',q}(\nu^*, M\mu_{\gamma}^*, V^*, \Psi^*)$$

which is a matrix-variate Student's t random variable. Defining $\Upsilon = [\Omega_{\mathcal{U}}^T, Y_{\mathcal{U}}^T]^T$, as a matrix of dimension $m \times q$, where $m = 2n'$, the predictive distribution is

$$p(\Upsilon | Y) = \int P(\Upsilon, \Sigma | Y) d\Sigma. \quad (\text{S3})$$

This matrix-variate integral can be avoided by simply writing

$$p(\Upsilon | Y) = \frac{p(\Upsilon, \Sigma | Y)}{p(\Sigma | \Upsilon, Y)}. \quad (\text{S4})$$

The density $p(\Upsilon, \Sigma | Y)$ comes from Equation (S2), while the denominator is obtained as

$$\begin{aligned} p(\Sigma | \Upsilon, Y) &= \frac{p(\Sigma | Y)p(\Upsilon | \Sigma, Y)}{p(\Upsilon | Y)} \\ &\propto \frac{|\Psi^*|^{\frac{\nu^*}{2}} |V_\gamma^*|^{-\frac{q}{2}} |\Sigma|^{-\frac{\nu^*+m+q+1}{2}} \exp \left\{ -\frac{1}{2} \text{tr} [\Sigma^{-1} (\Psi^* + (\Upsilon - \mu^*)^T V_\gamma^{*-1} (\Upsilon - \mu^*))] \right\}}{2^{\frac{(\nu^*+m)q}{2}} (\pi)^{\frac{mq}{2}} \Gamma_q \left(\frac{\nu^*}{2} \right)} \\ &\propto |\Sigma|^{-\frac{\nu^*+m+q+1}{2}} \exp \left\{ -\frac{1}{2} \text{tr} [\Sigma^{-1} (\Psi^* + (\Upsilon - \mu^*)^T V_\gamma^{*-1} (\Upsilon - \mu^*))] \right\}, \end{aligned}$$

where $\mu^* = M\mu_\gamma^*$. Hence, $\Sigma | \Upsilon, Y \sim \text{IW}(\hat{\Psi}, \hat{\nu})$ with $\hat{\Psi} = (\Psi^* + (\Upsilon - \mu^*)^T V_\gamma^{*-1} (\Upsilon - \mu^*))$, and $\hat{\nu} = \nu^* + m$. The joint posterior predictive density by the follows from Equation (S4)

$$\begin{aligned} p(\Upsilon | Y) &= \frac{\text{MNIW}(\Upsilon, \Sigma | \mu^*, V_\gamma^*, \Psi^*, \nu^*)}{\text{IW}(\Sigma | \hat{\Psi}, \hat{\nu})} \\ &= K(\Upsilon) |\Psi^*|^{-\frac{\nu^*+m}{2}} \left| \mathbb{I}_m + V_\gamma^{*-1} (\Upsilon - \mu^*) \Psi^{*-1} (\Upsilon - \mu^*)^T \right|^{-\frac{\nu^*+m}{2}}, \end{aligned}$$

where $K(\Upsilon) = \frac{\Gamma_q(\frac{\hat{\nu}}{2}) |\Psi^*|^{\frac{\nu^*}{2}} |V_\gamma^*|^{-\frac{q}{2}}}{\Gamma_q(\frac{\nu^*}{2}) (\pi)^{\frac{mq}{2}}} = \frac{\Gamma_q(\frac{\nu^*+m}{2}) |\Psi^*|^{\frac{\nu^*}{2}} |V_\gamma^*|^{-\frac{q}{2}}}{\Gamma_q(\frac{\nu^*}{2}) (\pi)^{\frac{mq}{2}}}$, since $\hat{\nu} = \nu^* + m$.

This is a matrix-variate T density, which we denote as $\Upsilon | Y \sim \text{T}_{m,q}(\nu^*, \mu^*, V^*, \Psi^*)$. We recover exactly the same result, without needing to integrate out Σ (Iranmanesh et al., 2010; Gupta and Nagar, 2000), but only using Bayes theorem and related distribution theory. Finally, the marginal predictive distributions $\Omega_{\mathcal{U}} | \mathcal{D}$, and $Y_{\mathcal{U}} | \mathcal{D}$, are also available in analytic form as matrix T distributions for any set of predictive points \mathcal{U} .

S2 Computational details

Key computational aspects of the proposed method involve two points: comparing its theoretical complexity to state-of-the-art approaches and addressing memory constraints. The complexity comparison evaluates the method’s time and space efficiency, particularly its scalability with larger datasets. This includes discernment from the explicit objective function, highlighting its computational impact. Memory constraints are equally critical, as limitations can hinder performance despite powerful processors. The proposed method addresses these challenges, ensuring both scalability and efficient resource use.

In summary, this section will examine both the theoretical complexity, including the explicit derivation of the objective function for the optimization problems detailed in Equations (2.8) and (S5), as well as the memory management strategies, offering a comprehensive view of the computational feasibility in practical applications.

S2.1 Objective function for double Bayesian predictive stacking

We expound the double Bayesian predictive stacking in Section 2.3. The optimization problem used to compute the stacking weights in Equation (2.10) is formally defined as:

$$\max_{w \in S_1^K} \frac{1}{n} \sum_{i=1}^n \log \sum_{k=1}^K w_k \hat{p}(Y_i | \mathcal{D}_k) = \max_{w \in S_1^K} \frac{1}{n} \sum_{i=1}^n \log \sum_{k=1}^K w_k \sum_{j=1}^J \hat{z}_{k,j} p(Y_{k,i} | \mathcal{D}_{k,[-l]}, \mathcal{M}_j), \quad (\text{S5})$$

as $\hat{p}(Y_i | \mathcal{D}_k) = \sum_{j=1}^J \hat{z}_{k,j} p(Y_{k,i} | \mathcal{D}_{k,[-l]}, \mathcal{M}_j)$. In this DOUBLE BPS framework, we focus exclusively on \mathcal{D}_k , which is treated equivalently to \mathcal{M}_j in the first step. It is crucial to discriminate the predictive performance induced by each \mathcal{D}_k . We must utilize a common set of Y across all \mathcal{D}_k – namely, Y itself. This stems from the construction of BPS. Specifically, for BPS to be effective, it necessitates predictive assessments over a common set of points for each model in the competition. Otherwise, the predictive performances cannot be directly compared, and the weights cannot be optimized to distinguish predictive capabilities across

models, as different points would be used for different models. To illustrate, consider the first stacking step. Here, we compute $p(Y_{k,i} | \mathcal{D}_k, \mathcal{M}_j)$ for each subset, where $i = 1, \dots, n_k$ and $j = 1, \dots, J$. This allows us to evaluate Y_k with respect to the predictive density of all J models under comparison. Similarly, in DOUBLE BPS, the goal is to evaluate Y_i with respect to the predictive density across all K subsets (acting as competing models) for comparison. The weights $\{\hat{z}_{k,j}\}$, which are derived from the optimization problem specified in Equation (2.8) also appear in Equation (S5). However, comparing the right-hand sides of Equations (S5) and (2.8), we observe that the objective functions are almost identical, with the only difference being the second convex linear combination governed by the weights $\{w_k\}$. Therefore, the predictive distributions in both optimization problems refer to the same quantity. To summarize, the objective function in Equation (2.8) can be derived by substituting each $\{z_{k,j}\}$ with its optimized counterpart $\{\hat{z}_{k,j}\}$ and incorporating the weights $\{w_k\}$. This leads to the maximization objective in Equation (S5).

Next, we consider the optimization problem in Equation (2.8) with objective function,

$$\max_{z_k \in S_1^J} \frac{1}{n_k} \sum_{i=1}^{n_k} \log \sum_{j=1}^J z_{k,j} p(Y_{k,i} | \mathcal{D}_{k,[-l]}, \mathcal{M}_j) = \max_{z_k \in S_1^J} f(z_k), \quad (\text{S6})$$

where $f(z_k) = \frac{1}{n_k} \sum_{i=1}^{n_k} \log \sum_{j=1}^J z_{k,j} p(Y_{k,i} | \mathcal{D}_{k,[-l]}, \mathcal{M}_j)$. An explicit form of $f(z_k)$ is

$$\begin{aligned} f(z_k) &= f(z_{k,1}, \dots, z_{k,J}) = \frac{1}{n_k} \sum_{i=1}^{n_k} \log \sum_{j=1}^J z_{k,j} p(Y_{k,i} | \mathcal{D}_{k,[-l]}, \mathcal{M}_j) \\ &= \frac{1}{n_k} \sum_{i=1}^{n_k} \log \sum_{j=1}^J z_{k,j} \text{T}_{1,q}(Y_{k,i} | \nu_{[-l]}^*, \mu_i^*, V_i^*, \Psi_{[-l]}^*) \\ &= \frac{1}{n_k} \sum_{i=1}^{n_k} \log \sum_{j=1}^J z_{k,j} K(Y_{k,i}) \left| 1 + V_i^{*-1} (Y_{k,i} - \mu_i^*) \Psi_{[-l]}^{-1*} (Y_{k,i} - \mu_i^*)^\text{T} \right|^{-\frac{\nu_{[-l]}^* + 1}{2}}, \end{aligned} \quad (\text{S7})$$

where $K(Y_{k,i}) = \frac{|\Psi_{[-l]}^*|^{-\frac{1}{2}} |V_i^*|^{-\frac{q}{2}} \Gamma_q\left(\frac{\nu_{[-l]}^*+1}{2}\right)}{(\pi)^{\frac{1}{2}} \Gamma_q\left(\frac{\nu_{[-l]}^*}{2}\right)}$. The logarithm of a linear combination precludes further accessibility, but $f(z_k)$ is computed easily by evaluating the matrix-T density. This is standard convex optimization (Yao et al., 2018); see Section 3 for further details.

The objective function in Equation (S5) is related to Equation (2.8) as

$$\max_{w \in S_1^K} \frac{1}{n} \sum_{i=1}^n \log \sum_{k=1}^K w_k \sum_{j=1}^J \hat{z}_{k,j} p(Y_{k,i} | \mathcal{D}_{k,[-l]}, \mathcal{M}_j) = \max_{w \in S_1^K} g(w), \quad (\text{S8})$$

where $w = (w_1, \dots, w_K)^T$ and

$$\begin{aligned} g(w) &= \frac{1}{n} \sum_{i=1}^n \log \sum_{k=1}^K w_k \sum_{j=1}^J \hat{z}_{k,j} p(Y_{k,i} | \mathcal{D}_{k,[-l]}, \mathcal{M}_j) \\ &= \frac{1}{n} \sum_{i=1}^n \log \sum_{k=1}^K w_k \sum_{j=1}^J \hat{z}_{k,j} T_{1,q}(Y_{k,i} | \nu_{[-l]}^*, \mu_i^*, V_i^*, \Psi_{[-l]}^*) \\ &= \frac{1}{n} \sum_{i=1}^n \log \sum_{k=1}^K w_k \sum_{j=1}^J \hat{z}_{k,j} K(Y_{k,i}) \left| 1 + V_i^{*-1} (Y_{k,i} - \mu_i^*) \Psi_{[-l]}^{-1*} (Y_{k,i} - \mu_i^*)^T \right|^{-\frac{\nu_{[-l]}^*+1}{2}}. \end{aligned} \quad (\text{S9})$$

In practical applications, we address Equation (S5) separately from Equation (2.8), which is defined for each k^{th} subset. Although it must be solved for each subset, we perform K separate maximizations of Equation (2.8), one for each subset. Once we obtain all K sets of $\{\hat{z}_{k,j}\}$, we can recover the weights $\{\hat{w}_k\}$ across subsets by solving the convex optimization problem in Equation (S5).

Overlooking the possibility of computing the subset stacking weights $\{z_{k,j}\}$ in parallel for the time being, this method offers a significant computational benefit: no extra quantities need to be computed to solve the problem in Equation (S5). All necessary information is already available from independent computations performed within each subset. For clarity, all the terms in Equations (2.8) and (S5) are known and coincide except for the weights w , which still need to be optimized. Consequently, there is no need to recompute the cross-validated predictive distributions or $\{\hat{z}_{k,j}\}$ as all these components have been computed.

S2.2 Theoretical complexity

In terms of theoretical computational complexity, we now provide a comparison between the SMK and the double BPS. So far, given a dataset \mathcal{D}_n , n denotes the total number of observations and K the number of subsets. Let M be the number of target posterior samples. From [Guhaniyogi and Banerjee \(2018\)](#), it is known that each posterior sample, considering a parallel implementation over K cores of SMK requires $\mathcal{O}\left(\left(\frac{n}{K}\right)^3\right)$. Thus, taking into account M draws from each of the subset posteriors yields theoretical complexity of $\mathcal{O}\left(M\left(\frac{n}{K}\right)^3\right)$, for each computational core. The cost of computing the Geometric median also has to be added. As stated in [Minsker et al. \(2017\)](#), Weiszfeld’s algorithm has a complexity of $\mathcal{O}(M^2)$ for each step and it needs at most $\mathcal{O}(1/\epsilon)$ steps to approximate the full posterior to a degree ϵ of accuracy. However, especially in large-scale applications, having a computational core for each subset is not always possible. Let us consider the number of available cores hereafter as m , generally $m \ll K$. Leading the total complexity of SMK, for K partitions in parallel over m cores to $\mathcal{O}\left(\frac{K}{m}\left[M\left(\frac{n}{K}\right)^3\right] + \frac{(KM)^2}{\epsilon}\right)$.

For theoretical complexity of double Bayesian predictive stacking, we have to specify J as the number of competitive models, and L as the number of folds used for cross-validations. Equivalently to SMK, model fitting within subsets is dominated by Cholesky decompositions implying costs in the order of $\mathcal{O}\left(\left(\frac{n}{K}\right)^3\right)$. Nevertheless, in double BPS, we perform J Cholesky decompositions, and for each of them, we refit the model L times. Hence, the theoretical complexity boils down to $\mathcal{O}\left(\frac{K}{m}JL\left(\frac{n}{K}\right)^3\right)$. In addition, we use the package CVXR [Fu et al. \(2020\)](#) in the R statistical computing environment by applying disciplined convex programming [Grant \(2005\)](#); [CVX Research \(2012\)](#) to find the stacking weights in polynomial time using an interior-point algorithm. We used the solvers SCS ([O’Donoghue et al., 2016](#)) and ECOSolveR ([Fu and Narasimhan, 2023](#)) to obtain the stacking weights. This introduces the discipline convex problems into the theoretical complexity, turning out to be $\mathcal{O}\left(\frac{K}{m}\left[JL\left(\frac{n}{K}\right)^3 + J^p\right] + K^p\right)$, for K subsets over m cores, and a polynomial degree p . The

portion in square brackets pertains to model fitting within each subset, consisting of a term related to cross-validation and the polynomial cost of BPS across J models. Finally, we account for the complexity introduced by the second stacking process across the K subsets.

Next, we compare the computational complexities of the two approaches. We will separately examine the terms associated with subset modeling and full inference combination. Thus, for SMK and double BPS, respectively, the computational complexities are as follows:

$$\mathcal{O} \left(\underbrace{\frac{K}{m} \left[M \left(\frac{n}{K} \right)^3 \right]}_{\text{subset modeling}} + \underbrace{\frac{(KM)^2}{\epsilon}}_{\text{combination}} \right), \quad \mathcal{O} \left(\underbrace{\frac{K}{m} \left[JL \left(\frac{\ell n}{K} \right)^3 + J^p \right]}_{\text{subset modeling}} + \underbrace{K^p}_{\text{combination}} \right) \quad (\text{S10})$$

Focusing on the subset modeling component, as highlighted in Equation (S10), two key specifications stand out. First, consider the difference in magnitude between M and the product JL . In this context, double BPS offers a theoretical advantage when $JL < M$, a quite common condition in practice. This is because M represents the number of posterior samples required for convergence across all the Markov chains involved, and it typically needs to be at least on the order of 10^3 . In contrast, the product JL consists of relatively small terms, making it highly likely that this inequality will hold. Second, due to the significant difference in scale, the term J^p is absorbed by $(n/K)^3$.

When comparing the combination phase, the analysis reduces to a comparison between the geometric median approximation and Bayesian predictive stacking. Since a discrete number of posterior samples M is required by SMK for each of the K partitions, we generally find that $K^p < (KM)^2/\epsilon$. Thus, while empirical computational times are significantly lower for double Bayesian predictive stacking compared to SMK, there are some modest theoretical differences between the two methods. The major advantage lies in avoiding simulation-based methods, such as MCMC while achieving local inferences through exact approaches.

Like Weiszfeld’s algorithm, modern disciplined convex programming encounters computational challenges in high-dimensional contexts, particularly in managing random memory

allocation. In Section S2.3, we present a feasible strategy for approximating the BPS weights, tailored for very large-scale memory problems.

S2.3 Memory management and Pseudo-BMA

When modeling GeoAI systems, as the number of locations exceeds the order of millions, managing storage space becomes crucial. Timing issues may arise depending on the available optimizer. While open-source solvers theoretically offer faster solutions compared to iterative algorithms, e.g. geometric median, they often face practical challenges when the problem size considerably exceeds dimensions of 10^2 . In contrast, commercial optimizers behave slightly better, even if these approaches are not exempted from random allocation memory constraints. We emphasize working with portable approaches, i.e. with open-source solvers, that can effectively handle large-scale problems.

We present a computationally cheaper alternative that facilitates better management of available RAM. The subsequent contents, including Algorithm S1, were implemented in data analyses involving millions (10^6) of locations of Sections 5, and S6. When addressing optimization problems of significant dimensions, AIC-based alternatives could be considered.

To facilitate model stacking, various methodologies exist within the Bayesian model averaging (BMA) framework. In particular, we present an approach based on information criteria, and formerly introduced in Yao et al. (2018). To ensure comparability between datasets and enhance interpretability, we estimate the expected log point-wise predictive density (as done in BPS). The expected log pointwise predictive density (*elpd*) for each partition k is defined as

$$\widehat{\text{elpd}}^k = \sum_{i=1}^n \widehat{\text{elpd}}_i^k = \sum_{i=1}^n \log p(Y_{k,i} | \mathcal{D}_{k,[-i]}) \quad (\text{S11})$$

Importantly, each *elpd* term need not be computed individually, as these values are generated during the first BPS procedure within each subset for all model configurations, significantly reducing memory storage requirements and the total computational burden. Given the set

Algorithm S1 Calculating stacking weights between subsets using pseudo-BMA

Input: $\hat{z} = \{\hat{z}_k = \{\hat{z}_{k,j}\} : k \in \{1, \dots, K\}, j \in \{1, \dots, J\}\}$: Stacking weights within subsets; $\{pd_{k,j,i} = T_{1,q}(Y_{k,i} \mid \nu_{[-l]}^*, \mu_i^*, V_i^*, \Psi_{[-l]}^*) : k = 1, \dots, K, j = 1, \dots, J, i = 1, \dots, n\}$: point-wise predictive density of Y ; n, q, p : Number of rows, number of outcomes, and number of predictors; $K, \{n_k : k \in \{1, \dots, K\}\}, J$: Number of subsets, dimension of each subset, and number of competitive models in each subset.

Output: $\hat{w} = \{\hat{w}_k : k = 1, \dots, K\}$: Stacking weights between subsets.

- 1: Construct $pd = \underbrace{[pd_1^T : \dots : pd_K^T]^T}_{n \times J}$, $pd_k = \underbrace{\begin{bmatrix} pd_{k,1,1} & \dots & pd_{k,J,1} \\ \vdots & pd_{k,j,i} & \vdots \\ pd_{k,1,n_k} & \dots & pd_{k,J,n_k} \end{bmatrix}}_{n_k \times J}$
 - 2: **for** $k = 1, \dots, K$ **do**
 - 3: Compute $\widehat{elpd}^k = \sum_{i=1}^n \log(pd \hat{z}_k)$
 - 4: **end for**
 - 5: **for** $k = 1, \dots, K$ **do**
 - 6: Compute $\hat{w}_k = \exp(\widehat{elpd}^k) / \sum_{k=1}^K \exp(\widehat{elpd}^k)$
 - 7: **end for**
 - 8: **return** $\hat{w} = \{\hat{w}_k : k \in \{1, \dots, K\}\}$
-

$\{\widehat{elpd}^k\}_{k=1, \dots, K}$, the pseudo Bayesian model averaging (pseudo-BMA) weights are computed as

$$\hat{w}_k = \frac{\exp(\widehat{elpd}^k)}{\sum_{k=1}^K \exp(\widehat{elpd}^k)}. \quad (\text{S12})$$

This formulation, early introduced by Yao et al. (2018), simplifies the computation of the stacking weights, significantly reducing computational costs in terms of complexity and storage while maintaining the Bayesian predictive stacking framework. Thus, it serves as a viable alternative to BPS for predictive densities in challenging scenarios. When dealing with datasets comprising millions of instances and a substantial number of partitions, optimization solvers may fail or produce errors due to memory constraints, and the iterative processes involving large matrices can lead to increased procedure times.

Based on empirical experience, we primarily utilize pseudo-BMA as a Bayesian predictive stacking approach when datasets require excessive memory storage, particularly when $n \gg 10^5$ and $K \gg 10^2$. When feasible we generally prefer convex optimization using BPS of predictive densities without reservations. Simulations highlighting potential differences in

posterior predictive and posterior inference performances between these two model stacking approaches can be found in Yao et al. (2018), where several alternatives to Bayesian stacking approaches were discussed. We opted for pseudo-BMA due to its simpler analytical formulation, which enables matrix algebra to mitigate the computational burden of both random allocation memory and runtime.

S2.4 Memory-efficient posterior sampling

In the matrix-variate conjugate Bayesian linear regression model presented in Equation (2.2), the Bayesian updating process may become costly if several data shards come, even more, if the dimensions involved are somehow cumbersome. Computational problems are often related to the available RAM, especially when working with considerable datasets. We present a memory-efficient posterior sampling for the regression coefficient β , helping in such intricate contexts. We consider the model in Equation (2.2) of Section 2.1,

$$\begin{aligned} Y &= X\beta + E, \quad E | \Sigma \sim \text{MN}(O, V, \Sigma); \\ \beta &= M_0 m_0 + E_\beta, \quad E_\beta | \Sigma \sim \text{MN}(O, M_0, \Sigma); \quad \Sigma \sim \text{IW}(\Psi_0, \nu_0), \end{aligned} \tag{S13}$$

Where Σ is assumed as known hereafter. Then, by matrix normal distribution theory, we know the exact form of the posterior distribution

$$\beta | \mathcal{D}, \Sigma \sim \text{MN}(M_n m_n, M_n, \Sigma), \tag{S14}$$

where $M_n^{-1} = M_0^{-1} + X^\top V^{-1} X$, $m_n = m_0 + X^\top V^{-1} Y$. We provide a memory-efficient way to sample from this distribution and reduce its computational burden. We define random variables $Y_{rep} \sim \text{MN}(Y, V, \Sigma)$ and $Z \sim \text{MN}(M_0 m_0, M_0, \Sigma)$. Expressing the relation between Y_{rep} , Z , and B as

$$M_n^{-1} B = A_1 Z + A_2 Y_{rep}. \tag{S15}$$

We seek matrices A_1, A_2 such that $B \stackrel{d}{=} \beta \mid \mathcal{D}, \Sigma$. Since $\beta \mid \mathcal{D}, \Sigma$ is distributed as a Gaussian random variable, it is fully characterized by its mean and variance (in a such case, with both row and column covariance matrices). Then, all we need are A_1 and A_2 so that the first two moments of B matches with $\beta \mid \mathcal{D}, \Sigma$.

For $X \sim \text{MN}(m, v, s)$, we have $DXC \sim \text{MN}(DmC, DvD^\top, CsC^\top)$. Moreover, if X is $n \times q$, the row-variance matrix is defined as $v = \mathbb{V}_{\text{row}}(X) = \mathbb{E}[(X - m)(X - m)^\top] \text{tr}(s)^{-1}$ of dimension $(n \times n)$ and its elements are defined as the variance computed on each row, while the $q \times q$ column covariance matrix is depicted by $s = \mathbb{V}_{\text{col}}(X) = \mathbb{E}[(X - m)^\top(X - m)] \text{tr}(v)^{-1}$ (see, e.g., [Gupta and Nagar, 2000](#), for further details). Without loss of generality, we compute the row covariance matrix for B since the column covariance matrix Σ is given. Note that

$$M_n^{-1} \mathbb{V}_{\text{row}}(B) M_n^{-1} = A_1 \mathbb{V}_{\text{row}}(Z) A_1^\top + A_2 \mathbb{V}_{\text{row}}(Y_{\text{rep}}) A_2^\top = A_1 M_0 A_1^\top + A_2 V A_2^\top \quad (\text{S16})$$

Setting these matrices as $A_1 = M_0^{-1}$, and $A_2 = X^\top V^{-1}$, we have

$$M_n^{-1} \mathbb{V}_{\text{row}}(B) M_n^{-1} = M_0^{-1} M_0 M_0^{-1} + X^\top V^{-1} V V^{-1} X = M_0^{-1} + X^\top V^{-1} X = M_n^{-1}. \quad (\text{S17})$$

This implies $\mathbb{V}_{\text{row}}(B) = M_n$. The mean follows from

$$M_n^{-1} \mathbb{E}[B] = A_1 \mathbb{E}[Z] + A_2 \mathbb{E}[Y_{\text{rep}}] = M_0^{-1} M_0 m_0 + X^\top V^{-1} Y = m_n, \quad (\text{S18})$$

and we obtain $\mathbb{E}[B] = M_n m_n$. Therefore, we can derive the next equality in distribution between B and the posterior distribution of the regression coefficient β as

$$B \stackrel{d}{=} \beta \mid \mathcal{D}, \Sigma \sim \text{MN}(M_n m_n, M_n, \Sigma). \quad (\text{S19})$$

This implies we can sample from $\beta \mid \mathcal{D}, \Sigma$ by solving a linear system. Specifically, by simply drawing samples from Z and Y_{rep} , we obtain a sample from $\beta \mid \mathcal{D}, \Sigma$ by solving the system $(M_0^{-1} + X^\top V^{-1} X)B = (M_0^{-1} Z + X^\top V^{-1} Y_{\text{rep}})$ for B . This approach is particularly advantageous for Bayesian transfer learning, as it avoids storing several large matrices when computing the posterior of $\beta \mid \mathcal{D}, \Sigma$. Instead, only the prior precision matrix for β , M_0^{-1} , and the product matrix $X^\top V^{-1}$ need to be stored, significantly reducing the memory footprint.

S3 Simulations for multivariate models

We supplement empirical results from Sections 4.1 and 4.2. The full set of comparisons and findings is provided in Tables 1 and 2, respectively. For further details, we refer to the main article. Following the same structure, we begin by comparing the double Bayesian predictive stacking approach with the multivariate SMK method, as outlined in Section 4.1 and conclude with investigations for the transfer learning settings discussed in Section 4.2.

S3.1 Simulation - BPS vs SMK

The simulation experiment findings discussed in Section 4.1 do not include visualizations for each dataset/partition size combination. We provide a comprehensive collection of plots and detailed expositions. Recall that the two generated datasets consist of 5,000 and 10,000 rows, respectively, based on the model introduced in Equation (2.4). Each dataset includes $q = 2$ outcomes, and $p = 2$ predictors, with spatial coordinates randomly placed within the unit square. The model simulations are conducted with the parameters fixed at $\beta = \begin{bmatrix} -0.75 & 1.85 \\ 0.90 & -1.10 \end{bmatrix}$, $\Sigma = \mathbb{I}_q$ and a spatial variability proportion of $\alpha = 0.8$. The spatial covariance follows an exponential function with $\phi = 4$. The predictors' matrix X includes an intercept, with the remaining $p - 1$ columns consisting of values randomly generated from a uniform distribution on $[0, 1]$.

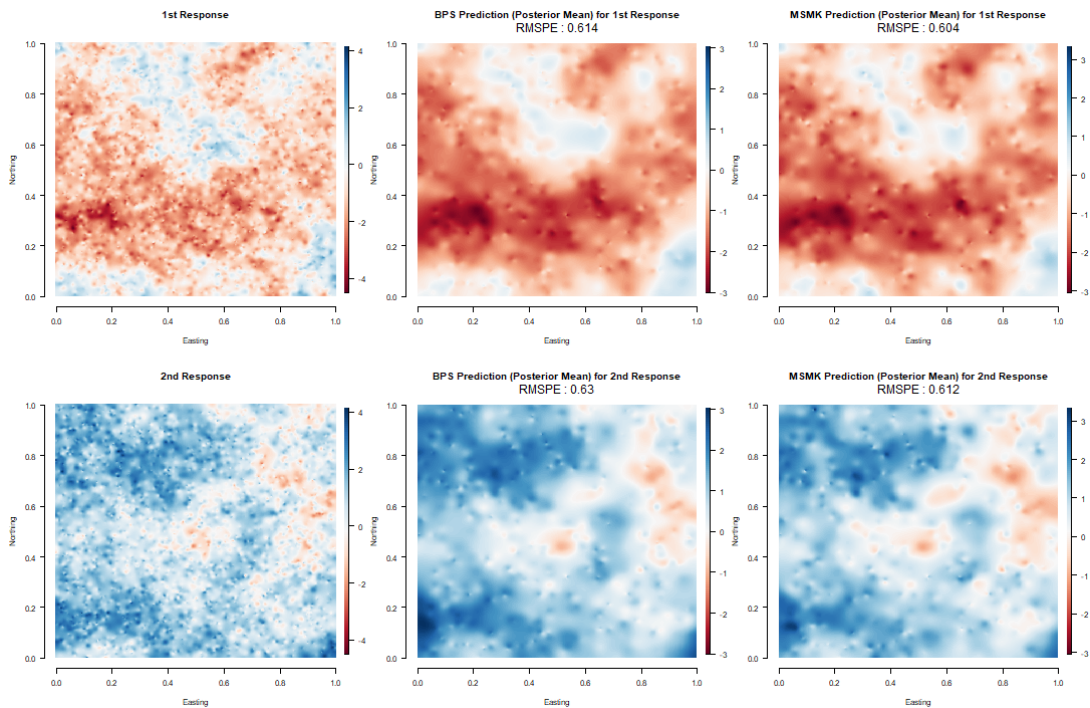


Figure S1: from left to right: comparison between the true generated response surfaces, the surfaces predicted from BPS and SMK (posterior mean), with RMSPE. For $n = 5000$, $K = 5$.

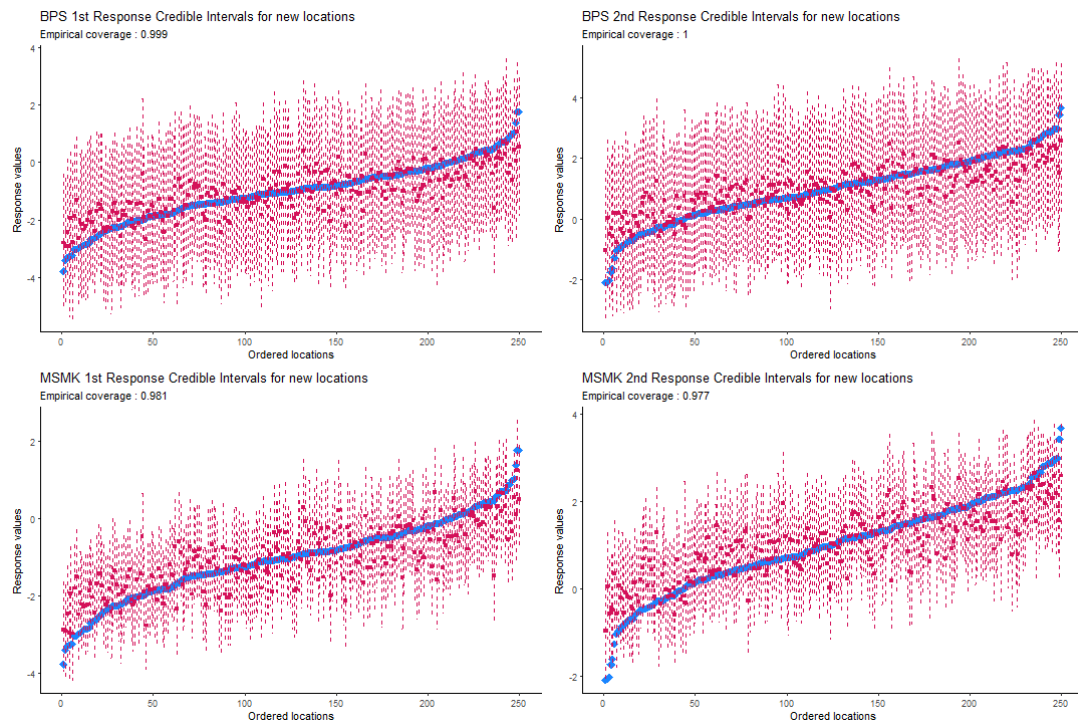


Figure S2: from top to bottom: comparison between posterior predictive intervals for the predicted response from BPS and SMK, with empirical coverage. For $n = 5000$, $K = 5$.

We implement our analysis with two different partition sizes, 500 and 1,000, for each dataset. Hence, $K = 10$ for $n = 5,000$ and $K = 20$ for $n = 10,000$ when the partition

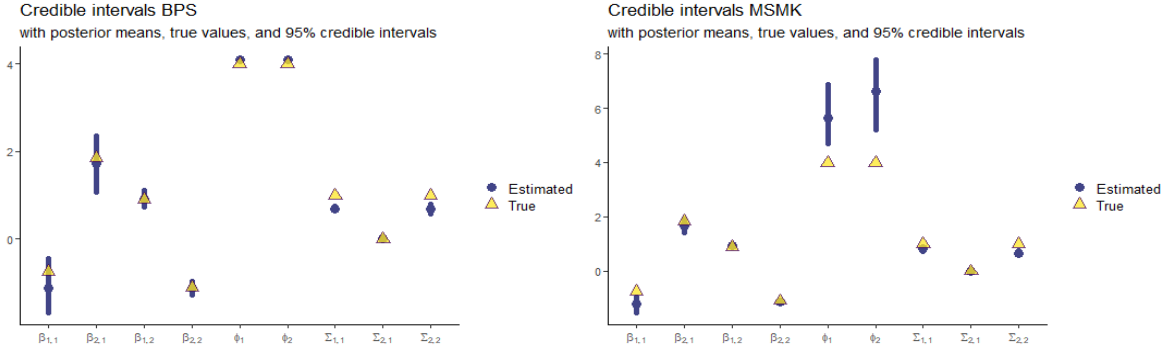


Figure S3: from left to right: comparison between posterior credible intervals for the parameters recovered from BPS and SMK. For $n = 5000$, $K = 5$.

size is fixed at 500 units, and $K = 5$ for $n = 5,000$ and $K = 10$ for $n = 10,000$ when it is 1,000. When implementing double Bayesian predictive stacking, we consider $J = 9$ competitive models, $\mathcal{M}_j, j = 1, \dots, J$, where each model is specified by a set of values for the hyperparameters $\{\alpha_j, \phi_j\}$ in Equation (2.4), representing the proportion of spatial variability and the parameter(s) of the spatial correlation function, respectively. In the following simulations, the grid of models was built using: $\alpha \in \{0.70, 0.80, 0.90\}$, and $\phi \in \{3, 4, 5\}$. We introduce prior information following Equation (2.5) with standard choices. Specifically, we set: $m_0 = 0_{p \times q}$, $M_0 = 10\mathbb{I}_p$, $\Psi_0 = \mathbb{I}_q$, and $\nu_0 = 3$, in the joint prior specified by Equation (2.5). For data analysis, we use an exponential spatial correlation function for $\rho_\phi(\cdot, \cdot)$, which is fully defined conditionally on \mathcal{M}_j , as each model specifies a value for ϕ . In the conjugate framework, we draw $R = 250$ samples from the posterior and posterior predictive distributions.

Since Section 4.1 already presents results for $\{n = 5000, K = 10\}$, we begin directly with the setting $\{n = 5000, K = 5\}$, omitting repeated results. Similarly, the results in Table 1 are omitted here and referenced in the main paper to avoid duplication.

Figure S1 shows the estimated response surface using BPS for $\{n = 5000, K = 5\}$. This plot reveals no noteworthy differences compared to the results obtained from MSMK. Although the RMSPE values for MSMK are slightly better, the differences are negligible when compared with the response scale, leading us to conclude that both approaches exhibit

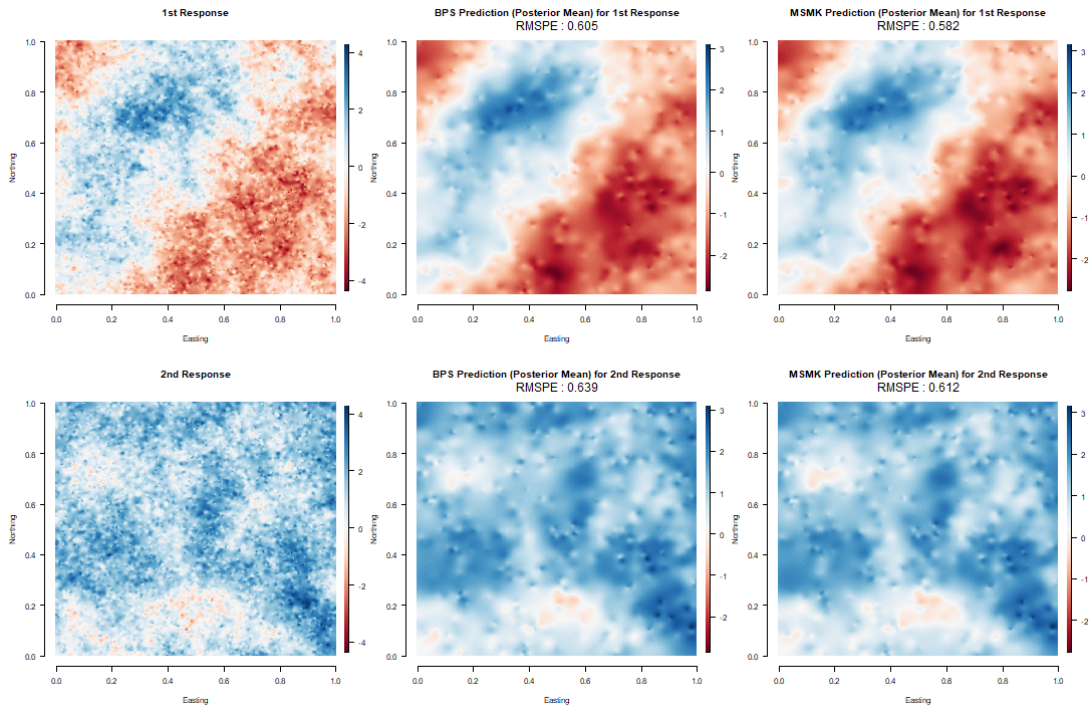


Figure S4: from left to right: comparison between the true generated response surfaces, the surfaces predicted from BPS and SMK (posterior mean), with RMSPE. For $n = 10000$, $K = 20$.

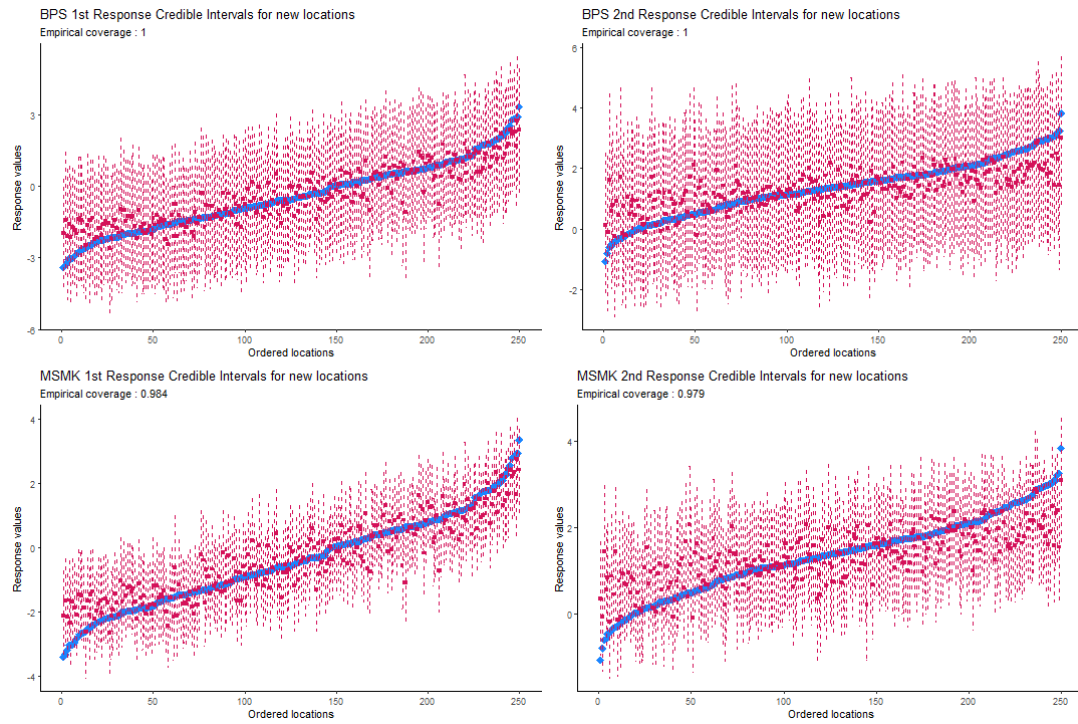


Figure S5: from top to bottom: comparison between posterior predictive intervals for the predicted response from BPS and SMK, with empirical coverage. For $n = 10000$, $K = 20$.

almost identical predictive performance. Regarding the first scenario from Section 4.1, it is unsurprising that a doubled number of locations per partition leads to improved performance.

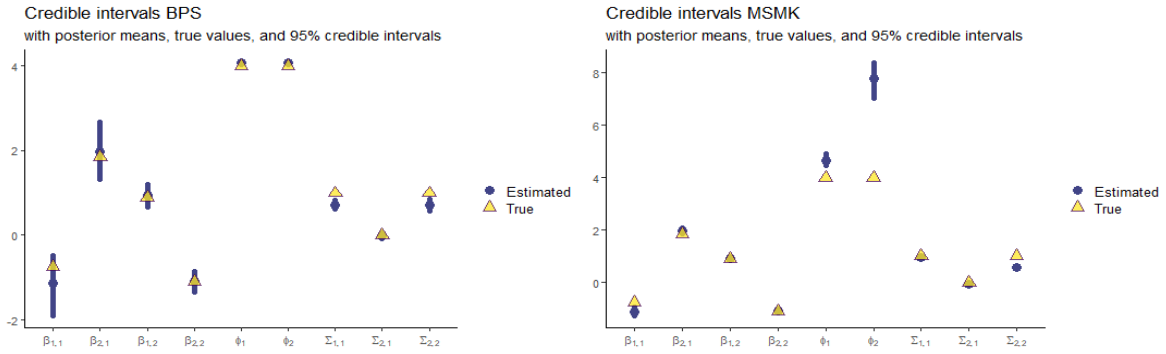


Figure S6: from left to right: comparison between posterior credible intervals for the parameters recovered from BPS and SMK. For $n = 10000$, $K = 20$.

Figure S3 provides empirical support to this. While MSMK shows some degree of spatial over-smoothing, as indicated by higher estimated values of ϕ compared to the true ones, BPS does not exhibit such deviations. Both the MAP estimates and the posterior inferences for BPS show strong performance. Recall that BPS reconstructs the point estimates for the range parameters ϕ using $\sum_{k=1}^K \hat{w}_k \sum_{j=1}^J \hat{z}_j \phi_j$, as explained in Section 4.1.

Figure S2 aligns with the previous conclusions, highlighting slightly wider predictive credibility intervals for BPS compared to MSMK. However, this difference is less pronounced than the underestimation of variability witnessed with SMK. For both approaches, the empirical coverage appears impressive.

Despite focusing on the larger dataset later in this section, where $n = 10,000$, the results increasingly appear to depend on the size of the subsets rather than the number of partitions. This remark on the influence of local inferences on global performance, with the number of partitions playing a lesser role.

For the case $\{n = 10,000, K = 20\}$, Figure S4 compares the estimated posterior mean surfaces. As seen in Section 4.1 and Section S5.1, the performances of BPS and SMK are nearly equivalent. The most noticeable difference is in Figure S5, where SMK produces narrower predictive credible intervals for the response variable. However, in Figure 4, BPS demonstrates superior posterior MAP estimates, including for the range parameters, which are typically challenging to identify. Together, Figures S5, S6, and S4 present comparable

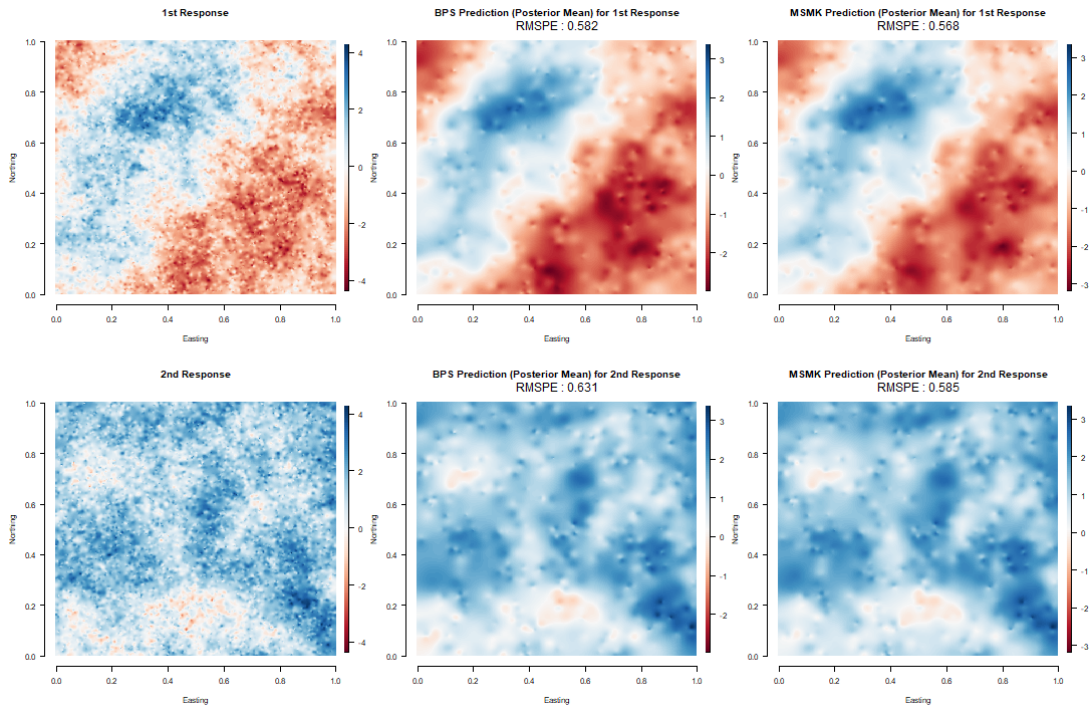


Figure S7: from left to right: comparison between the true generated response surfaces, the surfaces predicted from BPS and SMK (posterior mean), with RMSPE. For $n = 10000$, $K = 10$.

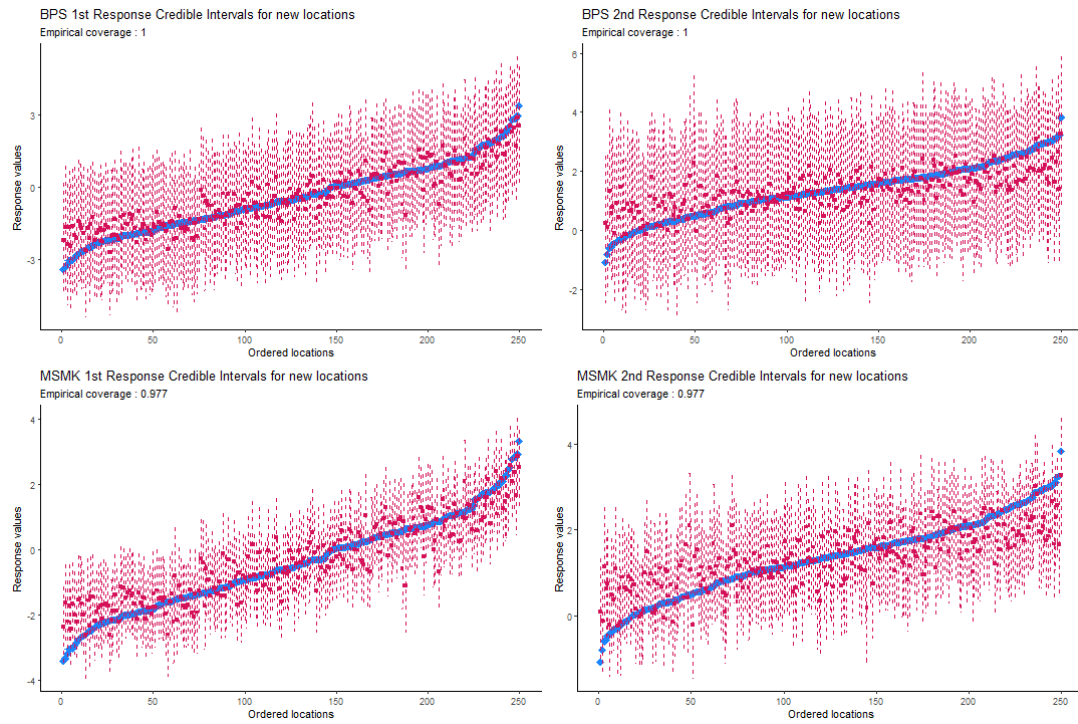


Figure S8: from top to bottom: comparison between posterior predictive intervals for the predicted response from BPS and SMK, with empirical coverage. For $n = 10000$, $K = 10$.

findings to the $\{n = 5,000, K = 10\}$ setting, reinforcing the importance of subset learning over the overall dataset size, as expected.

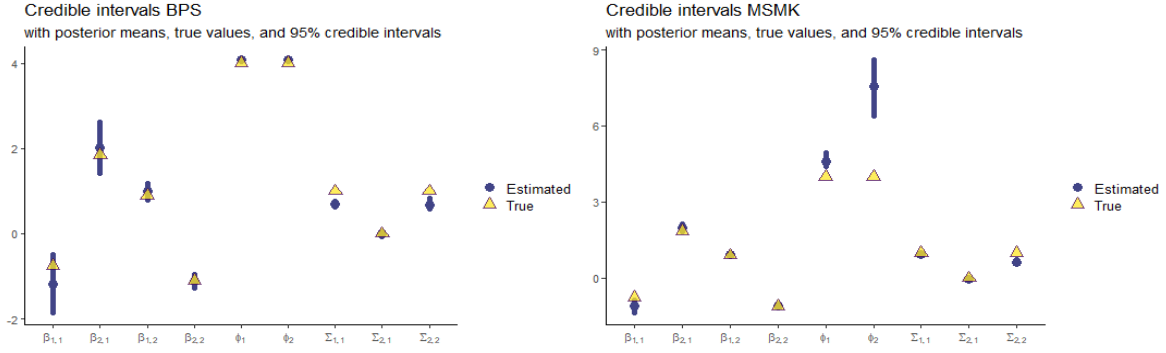


Figure S9: from left to right: comparison between posterior credible intervals for the parameters recovered from BPS and SMK. For $n = 10000$, $K = 10$.

The simulation experiment concludes with the $\{n = 10,000, K = 10\}$ setting. Once again, Figures S7, S8, and S9 show results consistent with previous settings, particularly with $\{n = 5,000, K = 10\}$, highlighting the critical role of partition size in achieving reliable posterior inferences. In Figure S9, despite the strong posterior performance, BPS exhibits wider posterior credible intervals compared to MSMK. This is similarly reflected in Figure S8, where BPS achieves empirical coverage of 100% for the 95% predictive intervals. Furthermore, BPS tends to avoid the underestimation of spatial variances in Σ , as evidenced in Figure S9, supporting earlier findings.

A significant discrepancy, however, lies in the time required to perform the simulations using BPS versus multivariate SMK. Table 1 reports the absolute times for each approach, as well as the relative ratio of MSMK to BPS. As discussed in Section 4.1, the computational advantage of BPS over MSMK is substantial, becoming more pronounced as the dataset size increases, and making comparison infeasible for datasets with more than $n = 10,000$ locations.

In conclusion, as shown in Section 4.1, notwithstanding indistinguishable posterior inferences between BPS and multivariate SMK, Table 1 clearly illustrates that the primary advantage of Bayesian predictive stacking lies in its enormous computational efficiency. This speedup is crucial for delivering feasible Bayesian inference for large datasets within GeoAI systems.

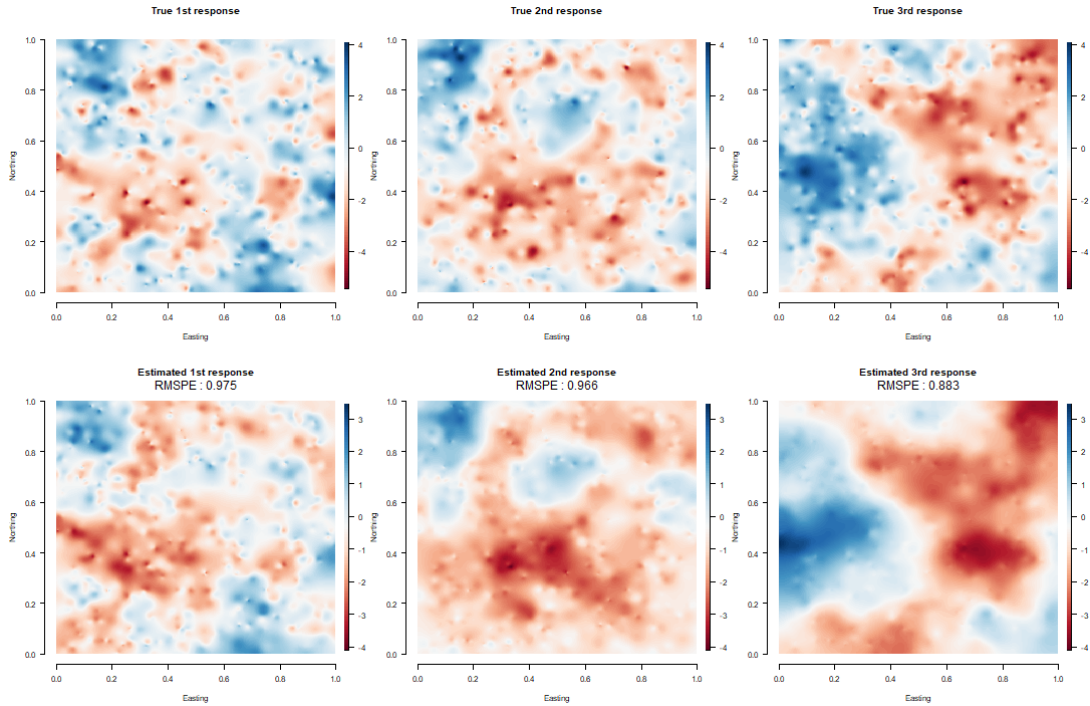


Figure S10: from left to right: comparison between the true spatial surface and the recovered surface for scenario (i), with RMSPE.

S3.2 Simulation - Transfer learning

To begin, we briefly outline the simulation settings. We analyze a synthetic dataset with dimensions $n = 5,000$, $q = 3$, and $p = 2$, generated according to the model specified

in Equation (2.4). The parameters are set as $\beta = \begin{bmatrix} -0.75 & 1.05 & -0.35 \\ 2.20 & -1.10 & 0.45 \end{bmatrix}$ and $\Sigma =$

$\begin{bmatrix} 2.00 & 0.80 & 0.20 \\ 0.80 & 2.00 & -0.45 \\ 0.20 & -0.45 & 2.00 \end{bmatrix}$. The predictor matrix X includes an intercept and $p - 1$ columns

generated from a uniform distribution over the interval $[0, 1]$. Prior information is fixed as $m_0 = 0_{p \times q}$, $M_0 = 10\mathbb{I}_p$, $\Psi_0 = \mathbb{I}_q$, and $\nu_0 = 3$ for each model under consideration.

We examine $J = 9$ competitive models for double Bayesian predictive stacking (BPS), utilizing values of $\alpha \in \{0.75, 0.80, 0.85\}$ and $\phi \in \{2, 4, 6\}$. In addition to the double BPS, we analyze the model presented in Equation (2.2), where the generated data is partitioned into $K = 10$ random subsets, each containing 500 units. The conjugate model in Equation (2.4)

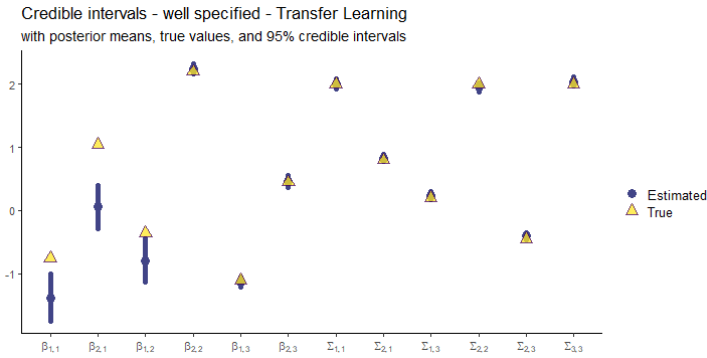


Figure S11: Posterior credible intervals for the parameters for scenario (i), with true parameters in yellow.

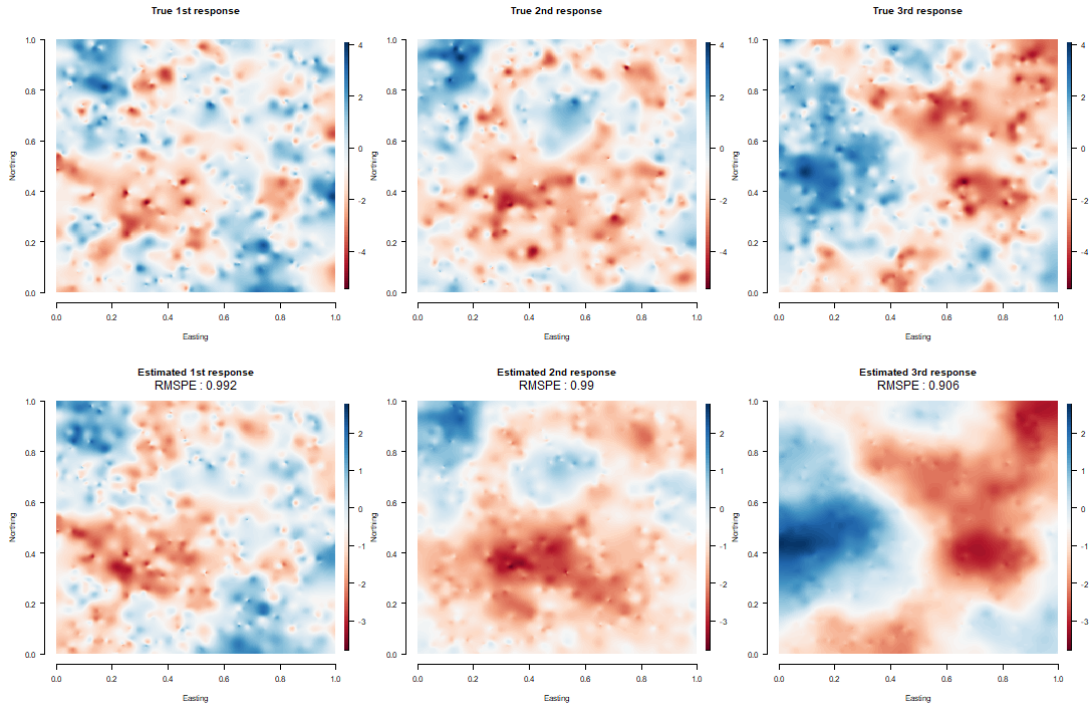


Figure S12: from left to right: comparison between the true spatial surface and the recovered surface for scenario (ii), with RMSPE.

requires fixed values for α and ϕ . Therefore, we consider three distinct scenarios: (i) a well-specified case with $\{\alpha = 0.8, \phi = 4\}$; (ii) a moderately misspecified case with $\{\alpha = 0.45, \phi = 6.63\}$; and (iii) a highly misspecified case with $\{\alpha = 0.25, \phi = 50\}$.

Starting with scenario (i), referred to as “well specified”, we proceed through varying degrees of misspecification, presenting two illustrative plots accompanied by detailed interpretations. It is important to note that this scenario uses the same values for $\{\alpha, \phi\}$ as those used in the data generation mechanism. As expected, this setting yields strong predictive results. Figure S10 showcases effective interpolated predictive maps for all responses. How-

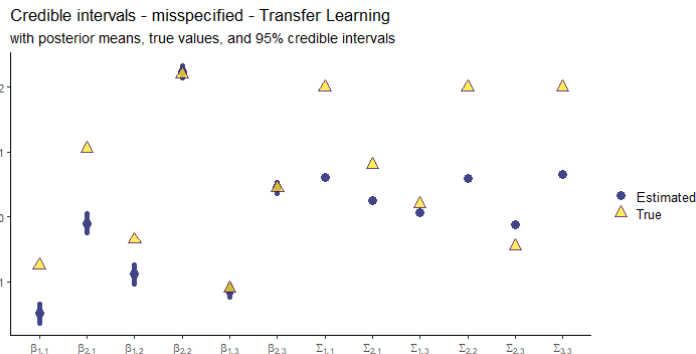


Figure S13: Posterior credible intervals for the parameters for scenario (ii), with true parameters in yellow.

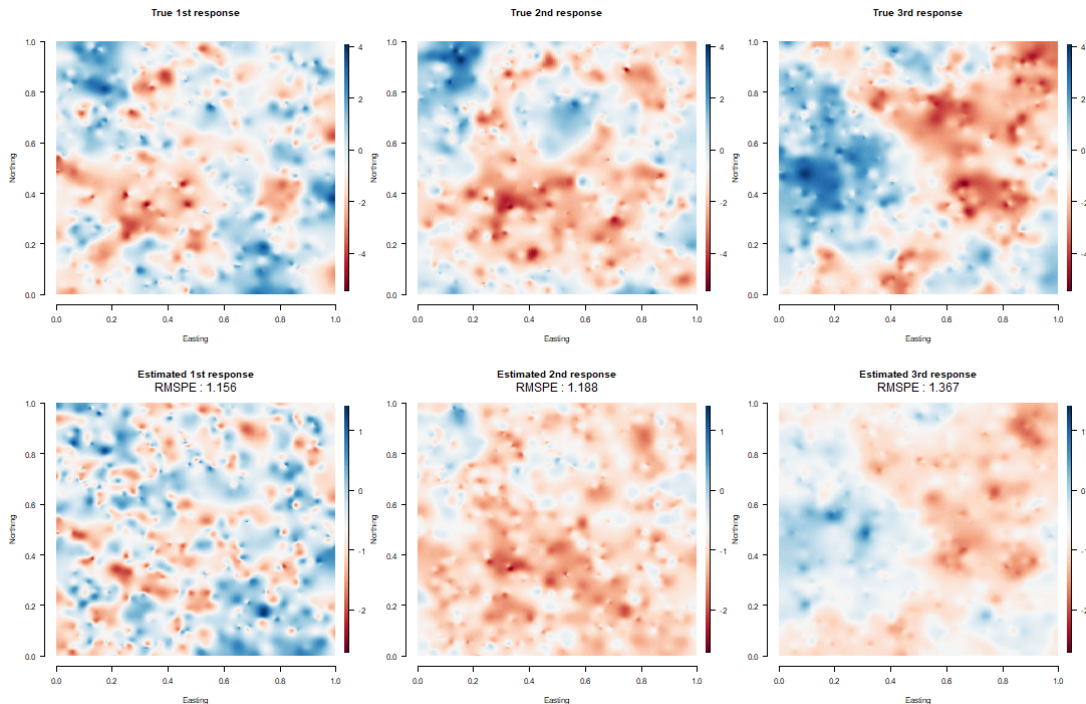


Figure S14: from left to right: comparison between the true spatial surface and the recovered surface for scenario (iii), with RMSPE.

ever, as indicated in Table 2, it does not attain the best RMSPE. In contrast, Figure S11 clearly illustrates that nearly all parameters lie within the posterior 95% credible intervals, indicating a robust recovery of the true values.

The first astonishing results emerge from the misspecified scenario, which involves $\{\alpha = 0.45, \phi = 6.63\}$. As shown in Table 2 and Figure S12, scenario (ii) performs almost equivalently to scenario (i) in terms of RMSPE. Conversely, Figure S13 reveals a different story: while the estimation for β remains reasonable, the estimates for the Σ are misleading, exhibiting a strong underestimation of spatial variability.

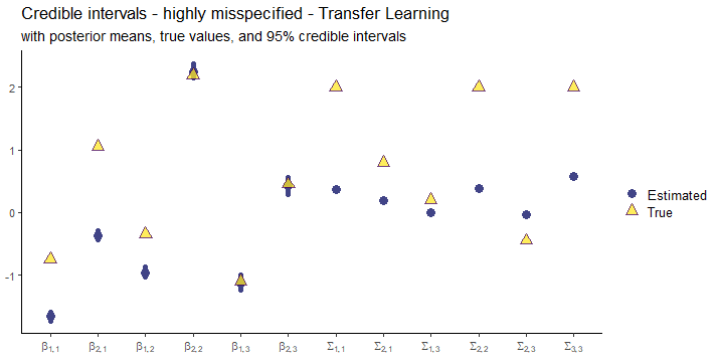


Figure S15: Posterior credible intervals for the parameters for scenario (iii), with true parameters in yellow.

Finally, we present results for the third and last scenario, characterized by high misspecification. Scenario (iii) involves an odd combination of values for α and ϕ . Specifically, fixing the range parameter at $\phi = 50$ results in an “almost spatially independent” model. To exemplify this, it suffices to note that the associated effective spatial range is 0.06, which is less than 5% of the maximum inter-point distance over the unit square. This indicates that the spatial correlation is expected to drop below 0.05 at such distances. Despite the theoretical implications of high misspecification, the results in Figure S14 are quite surprising. In particular, the predicted surface for the third response (bottom right panel in Figure S14) shows an unexpected spatial clustering of predictions that is almost unbelievable. Unfortunately, the posterior credible intervals in Figure S15 take us back to reality: posterior inference is notably poor. As expected and consistent across all scenarios, the inferential performance is weakest for the spatial variance, which is challenging to identify from the observed data (Zhang, 2004).

S3.3 Simulation - Subset size sensitivity

The methodological novelty introduced in Section 2.3 can be summarized in three main steps, as illustrated in Figure 1. First, we partition the original, often massive, dataset into K smaller subsets. The number of locations in each partition is a critical decision, seriously impacting inferential, predictive, and computational outcomes. Accordingly, a trade-off arises between computational resources and performance.

To address this, we conduct a simulation analysis to assess the sensitivity of the results to subset size. This section aims to investigate how predictive performance (in terms of RMSPE), and runtime (in seconds) change as the number of locations within each partition grows. Intuitively and theoretically, as the dimension of the subsets grows, we expect predictive performance to improve, while runtime increases polynomially with n . To enhance the comparability of the results, we apply min-max normalization to each variable, defined as $\tilde{x} = \frac{x - \min(x)}{\max(x) - \min(x)}$. This normalization scales all variables to the interval $[0, 1]$, facilitating a more direct graphical comparison.

We utilize a multivariate synthetic dataset comprising $n = 5,000$ locations, $q = 2$ simulated responses, and $p = 2$ predictors to explore the sensitivity to subset size. This dataset is generated from the model in Equation (2.4), with parameters $\beta = \begin{bmatrix} -0.75 & 1.85 \\ 0.90 & -1.10 \end{bmatrix}$ and $\Sigma = \begin{bmatrix} 1.00 & -0.30 \\ 0.40 & 1.00 \end{bmatrix}$. The predictor matrix X includes an intercept and $p - 1$ columns generated from a standard uniform distribution over $[0, 1]$. The range parameter for the exponential spatial covariance function, and the proportion of spatial variability, are fixed at $\phi = 4$ and $\alpha = 0.8$ respectively. We set prior information as follows: $m_0 = 0_{p \times q}$, $M_0 = 10\mathbb{I}_p$, $\Psi_0 = \mathbb{I}_q$, and $\nu_0 = 3$. These specifications and prior information remain constant, allowing only the number of locations in each subset to vary. In performing double BPS detailed in Section 2.3, we consider $J = 9$ competitive models characterized by $\alpha \in \{0.70, 0.80, 0.90\}$ and $\phi \in \{3, 4, 5\}$.

We focus our sensitivity analysis by selecting the following set of partition sizes: $\{25, 50, 100, 250, 500, 1000, 1250\}$, which correspond to the number of partitions $K \in \{200, 100, 50, 20, 10, 5, 4\}$. Figure S16 illustrates the two curves resulting from this sensitivity analysis.

As anticipated, the behavior of the two curves aligns with theoretical expectations across most scenarios. Specifically, the total time required to fit the model increases monotonically, exhibiting more than linear growth in the number of locations within each partition, as

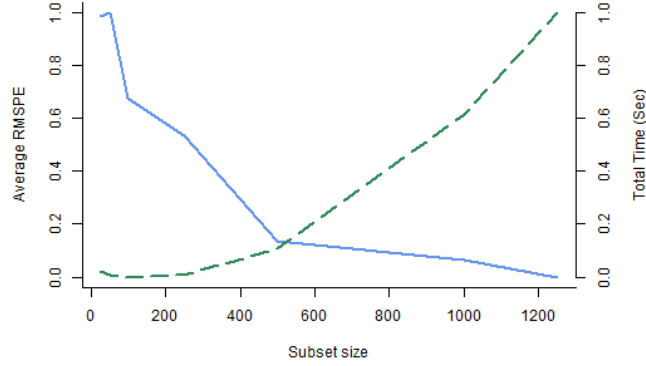


Figure S16: Comparison between average RMSPE (solid line) and model fitting time (dashed line) across various subset dimensions (both min-max normalized).

the dashed line exhibits in Figure S16. Conversely, the root mean square prediction error experiences an unexpected fluctuation, likely due to the extremes of very low or high numbers of locations/subsets (50/100). RMSPE decreases until it stabilizes at a “plateau” for partition sizes of 500 units on. The trends observed in Figure S16 reveal a compromise between predictive performance and computational effort close to a subset size of 500 units.

However, Figure S16 also raises an important question: how much predictive error is acceptable? The two quantities, although normalized for comparison, differ significantly in their scales. More precisely, the trade-off is asymmetric: doubling the number of locations per partition yields a moderate reduction in RMSPE, while the runtime can increase dramatically, rising at least quadratically with n . For all these reasons, we generally opt for a subset size of 500 locations in both our simulation studies and data applications. Nonetheless, we should not overlook the opportunity to reduce this size, accepting a trade-off in predictive performance to achieve even faster full Bayesian inference for exceptionally large GeoAI applications.

S4 Accelerated learning for univariate random fields

In Section 2.3 of the main manuscript, we propose a method to accelerate Bayesian learning for multivariate spatial random fields. While the primary focus is on multivariate geostatistical modeling, we also adapt this approach for simpler frameworks, specifically univariate random fields.

Let $\mathcal{S} = \{s_1, \dots, s_n\} \subset \mathcal{D}$ denote a set of n locations yielding observations on an outcome $y(s)$ for each $s \in \mathcal{S}$. We collect these measurements into the vector $y = (y(s_i))^T$, where $i = 1, \dots, n$. Let $X = [x(s_i)^T]$ represent an $n \times p$ matrix, with each row vector $x(s_i)^T$ consisting of recorded measurements on $p < n$ explanatory variables at the location $s_i \in \mathcal{S}$. It is assumed that X has full column rank p . Such data can be modeled spatially using a customary Bayesian hierarchical model.

$$\begin{aligned} y &= X\beta + \omega + e_y, \quad e_y \sim N(0, \delta^2 \sigma^2 \mathbb{I}_n), \quad \omega \mid \sigma^2 \sim N(0, \sigma^2 \rho_\phi(\mathcal{S}, \mathcal{S})) ; \\ \beta &= M_0 m_0 + e_\beta, \quad e_\beta \sim N(0, \sigma^2 M_0); \quad \sigma^2 \sim \text{IG}(a_\sigma, b_\sigma), \end{aligned} \tag{S20}$$

where y is $n \times 1$, X is an $n \times p$ matrix of explanatory variables, β is the $p \times 1$ vector of slopes measuring the trend, $\omega = (\omega(s_1), \dots, \omega(s_n))^T$ the finite-dimensional realization of the zero-centered spatial Gaussian process on \mathbb{R}^d , and let $\rho_\phi(\mathcal{S}, \mathcal{S})$ be the $n \times n$ spatial correlation matrix constructed from the correlation function with spatial correlation function $\rho_\phi(\cdot, \cdot)$ depending on spatial range parameter ϕ , and σ^2 is a scale (spatial variance) parameter, and e_y is the zero-centered random vector of errors, with $\tau^2 \mathbb{I}$ being the covariance matrix. Actually, Equation (S20) is parametrized with the noise-to-spatial variance ratio $\delta^2 := \tau^2 / \sigma^2$, instead of τ^2 . We further model $\beta \mid \Sigma \sim N(M_0 m_0, \sigma^2 M_0)$ and $\sigma^2 \sim \text{IG}(a_\sigma, b_\sigma)$, where all the hyperparameters, including the spatial correlation parameters ϕ , and the noise-to-spatial variance ratio δ^2 are considered fixed. Fixing the parameters ϕ and δ^2 ensures closed-form conjugate marginal posterior and posterior predictive distributions for this hierarchical specification (Finley et al., 2017; Banerjee, 2020). The joint density of β and σ^2 is denoted

by $\text{NIG}(M_0 m_0, M_0, a_\sigma, b_\sigma)$. Harnessing familiar results from conjugate Bayesian linear regression, we cast the spatial model in Equation (S20) into the following augmented linear system:

$$\underbrace{\begin{bmatrix} y \\ M_0 m_0 \\ 0 \end{bmatrix}}_{y_\star} = \underbrace{\begin{bmatrix} X & \mathbb{I}_n \\ \mathbb{I}_p & 0 \\ 0 & \mathbb{I}_n \end{bmatrix}}_{X_\star} \underbrace{\begin{bmatrix} \beta \\ \omega \end{bmatrix}}_{\gamma} + \underbrace{\begin{bmatrix} \eta_1 \\ \eta_2 \\ \eta_3 \end{bmatrix}}_{\eta}, \quad \eta \sim \text{N}(0, \sigma^2 V_\star),$$

where $V_\star = \begin{bmatrix} \delta^2 \mathbb{I}_n & 0 & 0 \\ 0 & M_0 & 0 \\ 0 & 0 & \rho_\phi(\mathcal{S}, \mathcal{S}) \end{bmatrix}$. For the new linear-system formulation of the hierarchical

model presented in Equation (S20), we derive a conjugate Bayesian model by considering the joint prior on the parameters $\{\gamma, \sigma^2\}$. This prior is denoted as $p(\gamma, \sigma^2 \mid M_0 m_0, M_0, a_\sigma, b_\sigma) \propto \text{IG}(\sigma^2 \mid a_\sigma, b_\sigma)$. Given that we have conjugacy for any fixed values of $\{\phi, \delta^2\}$ and hyperparameters in the prior density, we can then obtain the posterior density.

$$p(\gamma, \sigma^2 \mid \mathcal{D}) = p(\sigma^2 \mid \mathcal{D}) p(\gamma \mid \sigma^2, \mathcal{D}) = \text{IG}(\sigma^2 \mid a_\sigma^\star, b_\sigma^\star) \text{N}(\gamma \mid \hat{\gamma}, \sigma^2 M_\star), \quad (\text{S21})$$

where $a_\sigma^\star = a_\sigma + n/2$, $b_\sigma^\star = b_\sigma + 1/2 (y_\star - X_\star \hat{\gamma})^\top V_\star^{-1} (y_\star - X_\star \hat{\gamma})$, $M_\star^{-1} = X_\star^\top V_\star^{-1} X_\star$, and $\hat{\gamma} = M_\star X_\star^\top V_\star^{-1} y_\star$. The marginal posterior distribution $p(\gamma \mid \mathcal{D})$ is a multivariate Student's t with degrees of freedom $2a_\sigma^\star$, location $\hat{\gamma}$ and scale matrix $(b_\sigma^\star/a_\sigma^\star) M_\star$. We refer the reader to [Zhang et al. \(2024, Lemma 1\)](#) for further details regarding this result.

Let $\mathcal{U} = \{u_1, \dots, u_{n'}\} \in \mathcal{D}$ denote a set of n' unknown points. We define $\omega_{\mathcal{U}}$ and $y_{\mathcal{U}}$ as the $n' \times 1$ vectors with elements $\omega(u_i)$ and $y(u_i)$ for $i = 1, 2, \dots, n'$. The matrix of predictors is given by $X_{\mathcal{U}} = (x(u_1) : \dots : x(u_{n'}))^\top$ which is an $n' \times p$ matrix. Additionally, we denote the spatial correlation matrix at \mathcal{U} as $\rho_\phi(\mathcal{U}, \mathcal{U})$. Then, spatial predictive inference follows

from the posterior distribution

$$p(\omega_{\mathcal{U}}, y_{\mathcal{U}} | \mathcal{D}) = \int p(y_{\mathcal{U}} | \omega_{\mathcal{U}}, \beta, \sigma^2) p(\omega_{\mathcal{U}} | \omega, \sigma^2) p(\gamma, \sigma^2 | \mathcal{D}) d\gamma d\sigma^2, \quad (\text{S22})$$

which is again a multivariate t distribution with degrees of freedom $2a_{\sigma}^*$, location $\tilde{\mu}$ and scale matrix $(b_{\sigma}^*/a_{\sigma}^*)\tilde{M}$ where $\tilde{\mu} = W\hat{\gamma}$, and $\tilde{M} = WM_{\star}W^{\text{T}} + V_e$. With $V_{\omega} = \rho_{\phi}(\mathcal{U}, \mathcal{U}) - \rho_{\phi}(\mathcal{U}, \mathcal{S})\rho_{\phi}^{-1}(\mathcal{S}, \mathcal{S})\rho_{\phi}^{\text{T}}(\mathcal{U}, \mathcal{S})$, and $M_{\omega} = \rho_{\phi}(\mathcal{U}, \mathcal{S})\rho_{\phi}^{-1}(\mathcal{S}, \mathcal{S})$, we can express W , and V_e , as

$$W = \begin{bmatrix} 0 & M_{\omega} \\ X_{\mathcal{U}} & M_{\omega} \end{bmatrix}, \quad V_e = \begin{bmatrix} V_{\omega} & V_{\omega} \\ V_{\omega} & V_{\omega} + \delta^2\mathbb{I}_{n'} \end{bmatrix}. \quad (\text{S23})$$

The predictive distributions $p(\omega(u) | \mathcal{D})$ and $p(y(u) | \mathcal{D})$ are also available in analytic form as non-central t distributions for any single point $u \in \mathcal{D}$.

Analogous to the multivariate case discussed in Section 2.3, we use the BPS model averaging procedure to achieve global inference. This method enables us to leverage conjugate frameworks by integrating out two typically problematic hyperparameters: $\{\phi, \delta^2\}$. For further details, see Banerjee (2020).

To implement Bayesian stacking of predictive densities within subsets, we first partition the full data into K subsets, represented as $\mathcal{D} = \{\mathcal{D}_1, \dots, \mathcal{D}_K\}$. Next, we select a range of reasonable values for each hyperparameter. We then construct a grid that combines all possible pairs of hyperparameter values, resulting in a set of J competitive models: $\{\mathcal{M}_j\}_{j=1}^J$. For each model configuration \mathcal{M}_j , we follow the same scheme outlined in Section 2.3. The univariate setting does not alter the dimensions of the working quantities appearing in Algorithms 1 and 2, as the predictive densities are probability density functions, that always yield scalar values greater than zero. We then need to evaluate the predictive distributions $p(y_{k,i} | \mathcal{D}_{k,[-l]}, \mathcal{M}_j)$ for each of the J candidate models, where $i \notin [-l]$, $k = 1, \dots, K$, and $l = 1, \dots, L$, with L representing the number of folds. Here $y_{k,i}$ is the i -th element of $y_K \in \mathcal{D}_k$, for $i \in [l]$, and

$\mathcal{D}_{k,[-l]}$ is the full dataset excluding the l -th fold of units. As in the multivariate setting detailed in Section 2.3, closed-form conjugate posterior distributions are available. Considering results of Equation (S22), we have $p(y_{k,i} | \mathcal{D}_{k,[-l]}, \mathcal{M}_j) = \text{t}_{2a_{[-l],\sigma}^*}(\tilde{\mu}_i, [b_{[-l],\sigma}^*/a_{[-l],\sigma}^*]\tilde{M}_i)$. Where $\tilde{\mu}_i = W_{y,i}\hat{\gamma}_{k,[-l]}$, $W_{y,i} = \begin{bmatrix} X_{k,i} & \rho_{\phi_j}(\mathcal{S}_{k,i}, \mathcal{S}_{k,[-l]})\rho_{\phi_j}^{-1}(\mathcal{S}_{k,[-l]}, \mathcal{S}_{k,[-l]}) \end{bmatrix}$ and $\tilde{M}_i = W_{y,i}M_{[-l],\star}W_{y,i}^T + \delta_j^2 + V_{\omega,i}$, $V_{\omega,i} = \rho_{\phi_j}(\mathcal{S}_{k,i}, \mathcal{S}_{k,i}) - \rho_{\phi_j}(\mathcal{S}_{k,i}, \mathcal{S}_{k,[-l]})\rho_{\phi_j}^{-1}(\mathcal{S}_{k,[-l]}, \mathcal{S}_{k,[-l]})\rho_{\phi_j}(\mathcal{S}_{k,[-l]}, \mathcal{S}_{k,i})$. $\mathcal{S}_{k,[-l]}$, $\mathcal{S}_{k,i}$ are the set of locations in k -th partition of data, but not in fold l -th, and the location of $y_{k,i}$, respectively.

When closed-form predictive distributions are unavailable, point-wise predictive densities can be obtained using a sampling scheme that recovers conditional posterior predictive samples, followed by Monte Carlo (MC) averaging for the density. To this end, we can implement the following approximation: $p(y_{k,i} | \mathcal{D}_{k,[-l]}, \mathcal{M}_j) \approx \frac{1}{S} \sum_{s=1}^S p(y_{k,i} | \gamma^{(s)}, \sigma_{(s)}^2, \mathcal{M}_j)$. Here, $p(y_{k,i} | \gamma, \sigma^2, \mathcal{M}_j) \sim N(X_{k,i}^T\beta + \omega_i, \sigma^2\delta_j^2)$, since $\gamma = [\beta^T \ \omega^T]^T$. The samples $\gamma^{(s)}, \sigma_{(s)}^2$ are drawn from $p(\gamma, \sigma^2 | \mathcal{D}_{k,[-l]}, \mathcal{M}_j)$ (see Equation (S21)), for $s = 1, \dots, S$ with S the number of posterior samples used for the MC density approximation. Even when closed-form results are available for the predictive distributions in Equation (S22), the MC density approximation can significantly reduce computational burden. In fact, recovering the parameters for the marginal posterior predictive distributions may involve heavy matrix computations, rendering such approaches impractical in some contexts. Even when closed-form results are available for the predictive distributions in Equation (S22), often MC density approximation may result in a computational advantage. Recovering the parameters for the marginal posterior predictive distributions may involve heavy matrix computations, which makes their recovery worthless in some contexts.

We will now consider the same quantities discussed in Section 2.2, but adapted for the univariate setting. The first step involves fitting the subset models, specifically performing BPS within the subsets. The within-staking weight solve convex optimization problem takes the form $\max_{z_k \in S_1^J} \frac{1}{n_k} \sum_{i=1}^{n_k} \log \sum_{j=1}^J z_{k,j} p(y_{k,i} | \mathcal{D}_{k,[-l]}, \mathcal{M}_j)$. Accordingly, the between-stacking

weights are derived from the solution to the following problem:

$$\max_{w \in S_1^K} \frac{1}{n} \sum_{i=1}^n \log \sum_{k=1}^K w_k \sum_{j=1}^J \hat{z}_{k,j} p(y_{k,i} | \mathcal{D}_{k,[-l]}, \mathcal{M}_j). \quad (\text{S24})$$

We can now derive the desired inferences. Following the multivariate framework in Section 2.3, we obtain the predictive and posterior distributions of $\theta = \{\gamma, \sigma^2\}$ for the complete dataset through the convex combinations of local inferences from subsets, weighted by BPS weights. Specifically $\hat{p}(y_{\mathcal{U}} | \mathcal{D}) = \sum_{k=1}^K \hat{w}_k \sum_{j=1}^J \hat{z}_{k,j} p(y_{\mathcal{U}} | \mathcal{D}_k, \mathcal{M}_j)$, and $\hat{p}(\theta | \mathcal{D}) = \sum_{k=1}^K \hat{w}_k \hat{p}(\theta | \mathcal{D}_k) = \sum_{k=1}^K \hat{w}_k \sum_{j=1}^J \hat{z}_{k,j} p(\theta | \mathcal{D}_k, \mathcal{M}_j)$, for $k = 1, \dots, K$, and $j = 1, \dots, J$.

In conclusion, the main difference between univariate and multivariate settings lies in the introduction of matrix-variate random variables. Although the Bayesian predictive stacking of predictive densities necessitates adaptations to the computations due to the tensors formed by these matrix random variables, the principles of the procedure remain consistent. A comprehensive understanding of the mechanisms within either framework is sufficient for effective implementation.

S5 Simulations for univariate models

We conduct simulation experiments to evaluate the effectiveness of the proposed method. In this section, we present a selection of simulation results for univariate models, serving as the univariate counterpart to Section 4 and Section S3. Initially, we compare the performance of the BPS method against the SMK approach. Two synthetic datasets of different sizes are generated, and we evaluate posterior learning for each dataset by fixing the number of partitions and examining the impact of subset size on inference. Additionally, we assess the inferential performance of BPS across three transfer learning model configurations: (i) well-specified, (ii) misspecified, and (iii) highly misspecified models. Most comparisons are based on the root mean square prediction error. Several maps illustrate the method’s ability to recover

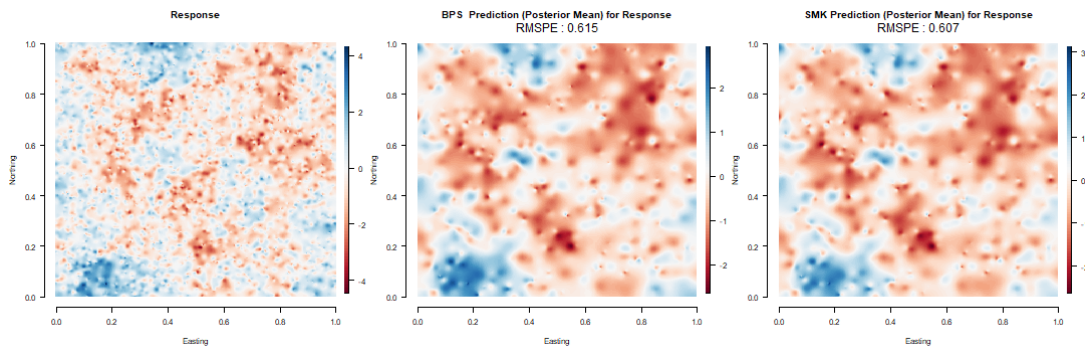


Figure S17: from left to right: comparison between the true response surface, the surface recovered from BPS and SMK, with RMSPE. For $n = 5000$, $K = 10$.

underlying spatial surfaces. We also examine the empirical coverage of predictive outcomes and present the corresponding results. Lastly, graphical representations of posterior credible intervals, along with the true parameter values (when available), are displayed for further evaluation.

S5.1 Simulation - BPS vs SMK

In the first simulation setup, we generate two synthetic datasets with similar structures but different sizes, based on the model in Equation S20. The datasets differ in the number of spatial locations, with $n = 5,000$ and $n = 10,000$, respectively, while both consider $p = 4$ predictors. Spatial coordinates are generated from a uniform distribution over the unit square and remain fixed throughout. The $n \times n$ spatial correlation matrix is constructed using an exponential spatial correlation function with $\phi = 4$, and the variance is set to $\sigma^2 = 1$. From these specifications, we generate the n -dimensional response vector y , using the first equation of (S20). The p -dimensional regression coefficient vector $\beta = \{-0.75, 0.9, -1.1, 1.85\}$ is fixed, along with the $n \times p$ predictor matrix X . The first column of X contains ones to represent the intercept, and the remaining $p - 1$ columns are randomly simulated from a uniform distribution over $[0, 1]$, emulating standardized predictors. We set the noise-to-spatial variance ratio $\delta^2 = \tau^2/\sigma^2 = 0.25$.

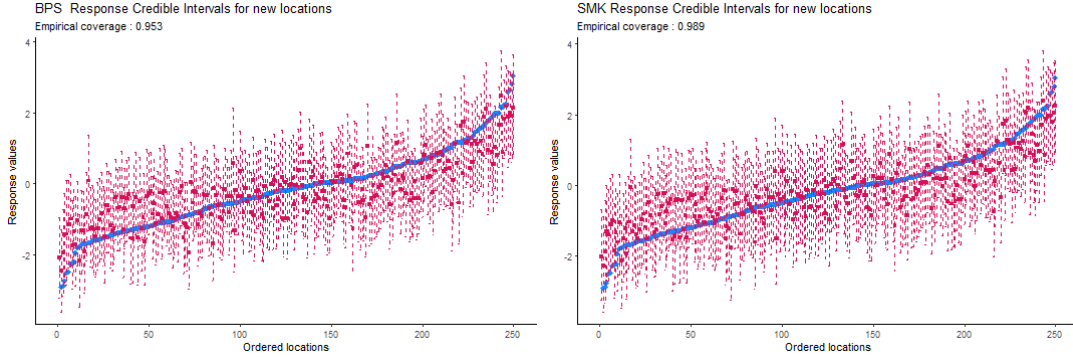


Figure S18: from left to right: comparison between posterior predictive intervals for the response recovered from BPS and SMK, with empirical coverage. For $n = 5000$, $K = 10$.

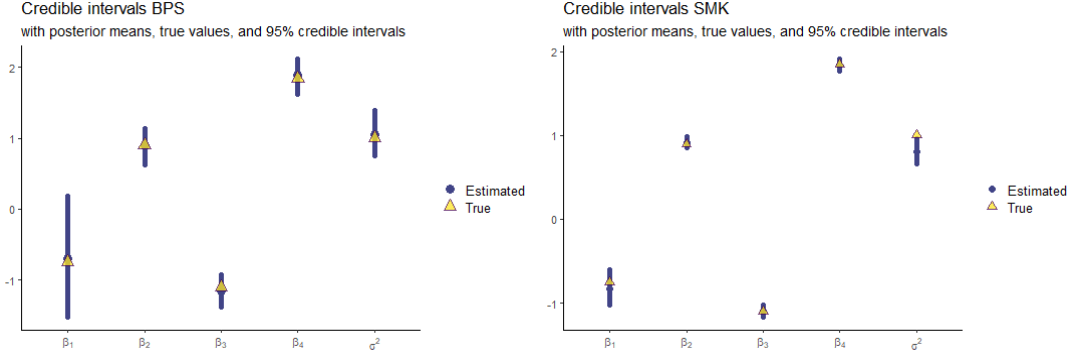


Figure S19: from left to right: comparison between credible intervals for the parameters recovered from BPS and SMK. For $n = 5000$, $K = 10$.

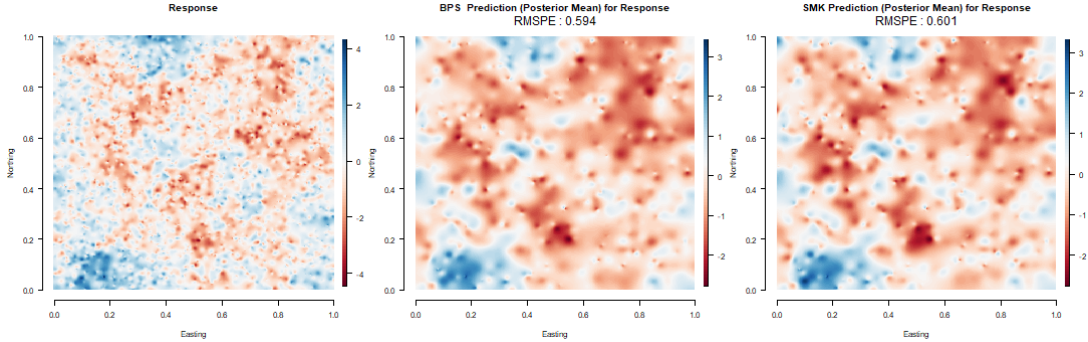


Figure S20: from left to right: comparison between the true response surface, the surface recovered from BPS and SMK, with RMSPE. For $n = 5000$, $K = 5$.

We implement BPS using $J = 9$ competitive models, $\mathcal{M}_j, j = 1, \dots, J$, where each model is defined by a set of candidate values for the hyperparameters $\{\delta_j^2, \phi_j\}$ in (S20). The candidate models are constructed by considering all possible combinations of selected values for δ^2 , and ϕ . In our experiments, the grid of models was built using $\delta^2 \in \{0.20, 0.25, 0.30\}$ and $\phi \in \{3, 4, 5\}$. These values correspond to effective spatial ranges of $\{0.99, 0.75, 0.60\}$ units, beyond which the spatial correlation drops below 5%.

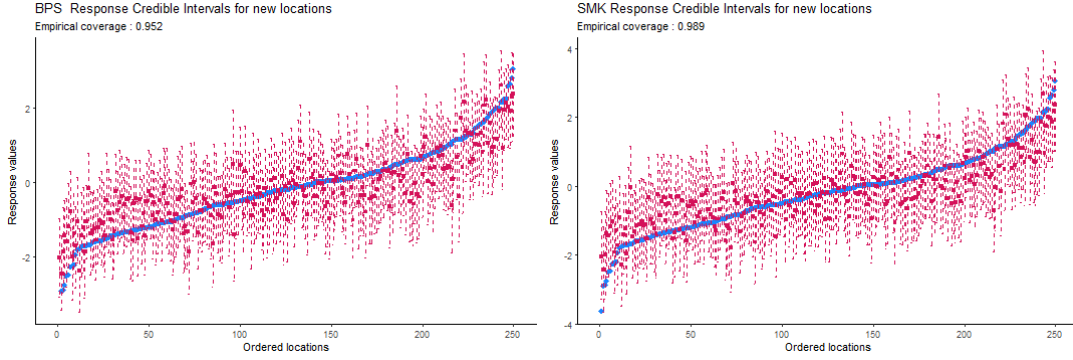


Figure S21: from left to right: comparison between posterior predictive intervals for the response recovered from BPS and SMK, with empirical coverage. For $n = 5000$, $K = 5$.

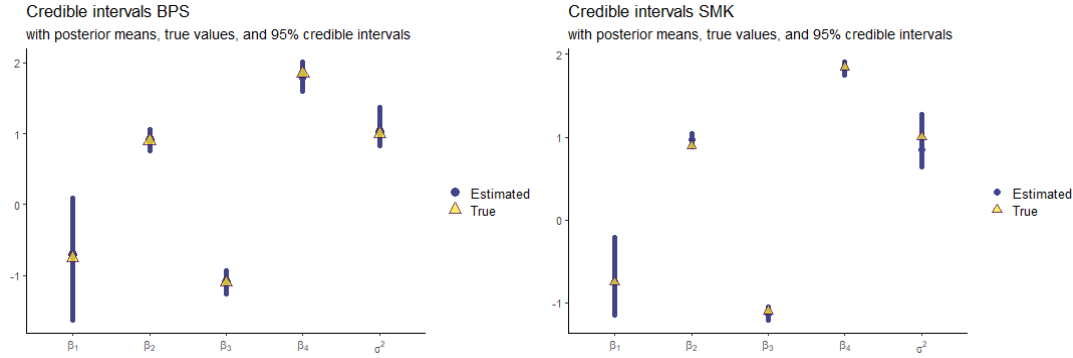


Figure S22: from left to right: comparison between credible intervals for the parameters recovered from BPS and SMK. For $n = 5000$, $K = 5$.

For the NIG joint prior proposed in Section S4, we adopt non-informative parameter choices. We set $m_0 = 0_p$, $M_0 = 10\mathbb{I}_p$, $a_\sigma = 2$, and $b_\sigma = 2$. In our experiments, we use an exponential spatial correlation function, $\rho_\phi(\cdot, \cdot)$, which is fully determined by the model \mathcal{M}_j , as it specifies a value for ϕ . Within this conjugate framework, we draw samples of size $R = 250$ from both the posterior and posterior predictive distributions.

We design simulation experiments considering four settings: $n = 5,000$ with $K = 10$ (subset size 500), $n = 5,000$ with $K = 10$ (subset size 1000), $n = 10,000$ with $K = 20$ (subset size 500), and $n = 10,000$ and $K = 10$ (subset size 500). To provide a comprehensive discussion of the results, we present three visualizations (cartoons) for each of the experimental settings.

Figure S17 shows the estimated response surface using both BPS and SMK for the setting $n = 5000$ and $K = 10$. The results indicate no significant differences in the interpolation between the two methods. Although the RMSPE reveals minor discrepancies, these differences

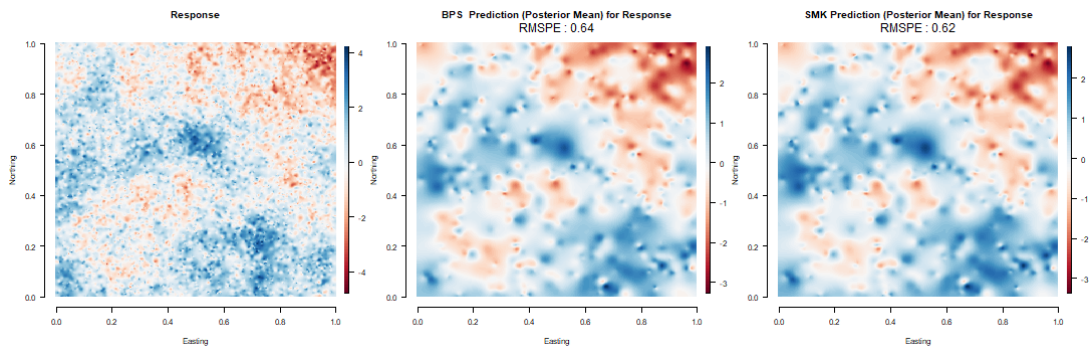


Figure S23: from left to right: comparison between the true response surface, the surface recovered from BPS and SMK, with RMSPE. For $n = 10000$, $K = 20$.

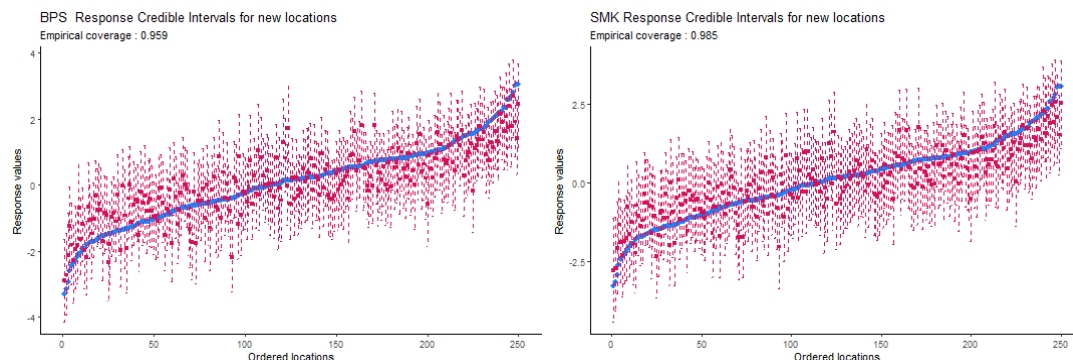


Figure S24: from left to right: comparison between posterior predictive intervals for the response recovered from BPS and SMK, with empirical coverage. For $n = 10000$, $K = 20$.

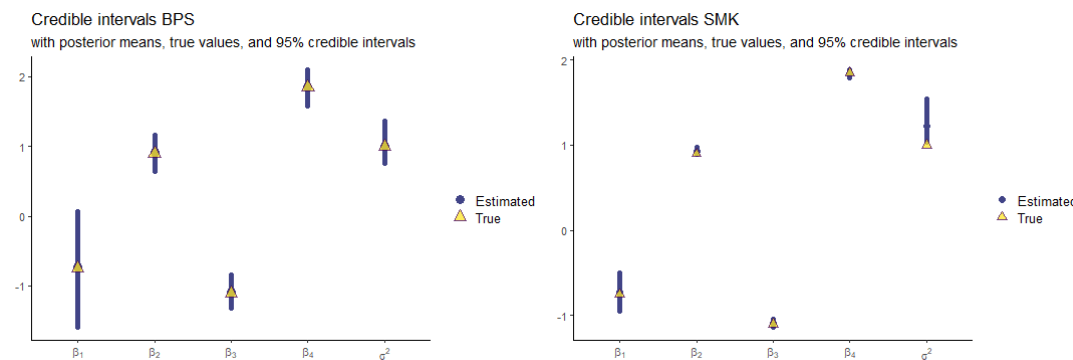


Figure S25: from left to right: comparison between credible intervals for the parameters recovered from BPS and SMK. For $n = 10000$, $K = 20$.

are negligible, making the predictive performance of both approaches largely indistinguishable. In Figure S18, we report the posterior predictive interval for the response variable. Once again, the empirical coverage appears impressive. While BPS produces slightly wider intervals, this effect is less pronounced than the underestimation of variability observed with SMK. Furthermore, Figure S18 highlights superior MAP estimates for BPS.

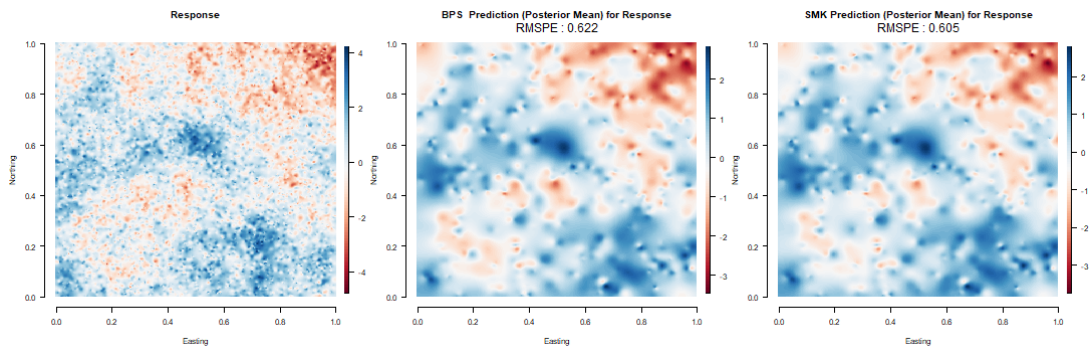


Figure S26: from left to right: comparison between the true response surface, the surface recovered from BPS and SMK, with RMSPE. For $n = 10000$, $K = 10$.

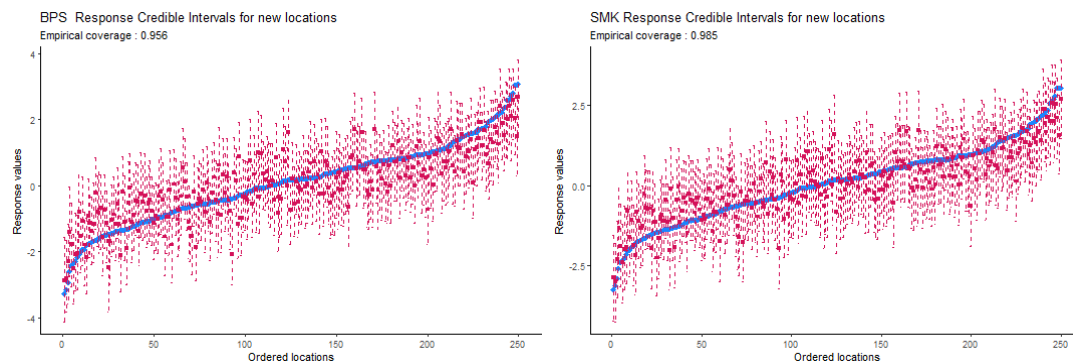


Figure S27: from left to right: comparison between posterior predictive intervals for the response recovered from BPS and SMK, with empirical coverage. For $n = 10000$, $K = 10$.

Figure S19 illustrates the recovery of parameter estimates. Similar to the predictive inference results, the posterior credible intervals for the parameters provide nearly indistinguishable inferences across the two models. Both methods successfully recover the true values for β and σ^2 , although BPS consistently delivers superior MAP estimates. Additionally, the narrow credible intervals produced by SMK, as shown in Figure S19, further confirm the underestimation of variability. Despite this, BPS offers wider posterior credible intervals, which are more accurately centered around the true parameter values.

In terms of predictive performance, both Figure S20 and Figure S21 show equivalent results for $n = 5000$ and $K = 5$. While the interpolated response surface shows no significant differences from the SMK results, the latter again results in an excess of empirical coverage.

As expected, increasing the subset size enhances the overall inferences. This improvement is evident in Figure S22, which illustrates a better recovery of parameter estimates,

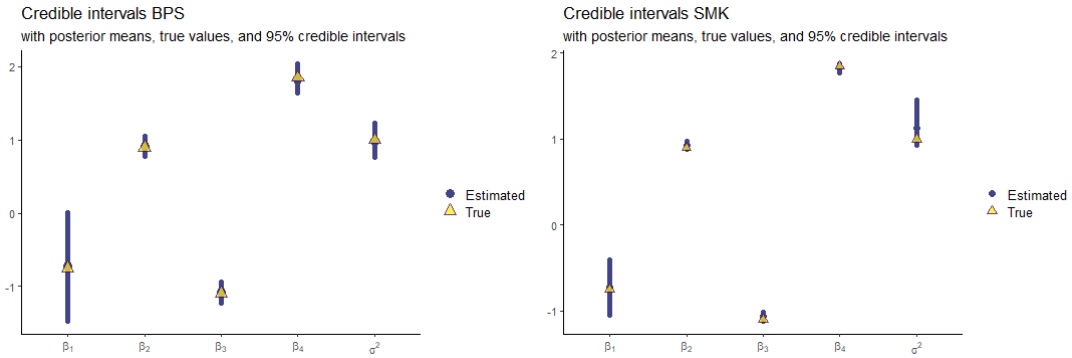


Figure S28: from left to right: comparison between credible intervals for the parameters recovered from BPS and SMK For $n = 10000$, $K = 10$.

particularly for SMK. For BPS, there are no major differences; both the MAP estimates and posterior inferences demonstrate good performance.

Figure S23 presents a comparison of the estimated posterior mean surfaces for $n = 10000$ and $K = 20$. The interpolation results obtained from SMK, show only minor discrepancies, with matching graphical outcomes. This pattern is also evident in the empirical coverage. Figure S24 demonstrates the striking similarities between the methods. However, as in previous settings, BPS produces superior MAP estimates, without the overabundance of empirical coverage seen with SMK.

Finally, Figure S25 shows the posterior credible intervals, where BPS delivers superior estimates, particularly for the spatial variance σ^2 . Together with Figure S19, these results suggest “accelerated” learning for BPS. Empirically, BPS appears to achieve superior model learning, holding other factors constant, especially evident from the partition size of 500. In contrast, SMK tends to yield poorer parameter recovery.

Figures S26, S27, and S28 display findings similar to those from the previous settings, particularly for $n = 5000$ and $K = 10$. These results reinforce the importance of subset size in producing reliable posterior inferences. Notably, even with a larger partition size, SMK underestimates σ^2 . In Figure S28, the true spatial variance parameter almost falls outside the 95% credible interval in the SMK approach.

Table S1: Computational aspects for the different settings, with time in minutes.

Model	$n = 5000, K = 10$	$n = 5000, K = 5$	$n = 10000, K = 20$	$n = 10000, K = 10$
SMK	27.02	120.42	69.50	329.14
BPS	1.34	7.24	2.21	11.05
Relative ratio	20.16	16.63	31.45	29.79

In conclusion, as observed in the multivariate modeling in Section 4.1 and Section S3.1, the inferences drawn from BPS and SMK in the univariate case are also indistinguishable, both in terms of predictive accuracy and inferential outcomes.

However, remarkable differences emerge when considering the computational effort required by each method. Table S1 reports the absolute computation times for both approaches, as well as the relative time ratio of SMK to BPS. The results highlight the computational gains achieved by BPS, while still maintaining equivalent inferential performance. The relative computational advantage of BPS becomes more pronounced as the dataset size increases, even with larger subsets. This can be attributed to the fact that Gaussian process regression dominates the overall computational cost, whereas assimilating inference from the subsets is comparatively less demanding.

Finally, as in the multivariate case, if the number of locations grows significantly, the geometric median of posteriors required by SMK becomes computationally infeasible, unlike the double Bayesian predictive stacking approach, which remains practical.

S5.2 Simulation - Transfer learning

We investigate the performance of various misspecified models, following the same approach used for multivariate modeling in Sections 4.2 and S3.2.

We begin by generating a synthetic dataset with $n = 5,000$ and $p = 2$, based on the model in Equation (S20). The parameters for this model are set as follows: $\beta = \{2.05, -0.55\}$, $\sigma^2 = 2$, and $\delta^2 = \tau^2/\sigma^2 = 0.25$. We choose an exponential spatial covariance function with a range parameter $\phi = 10$, which depicts the spatial dependence in ω . The predictor matrix

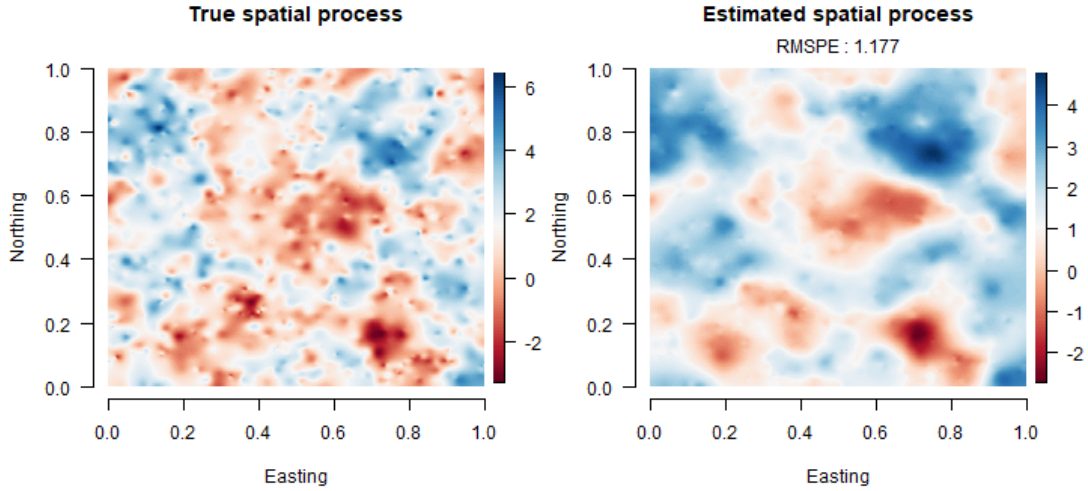


Figure S29: from left to right: comparison between the true spatial surface and the recovered surface for scenario (i), with RMSPE.

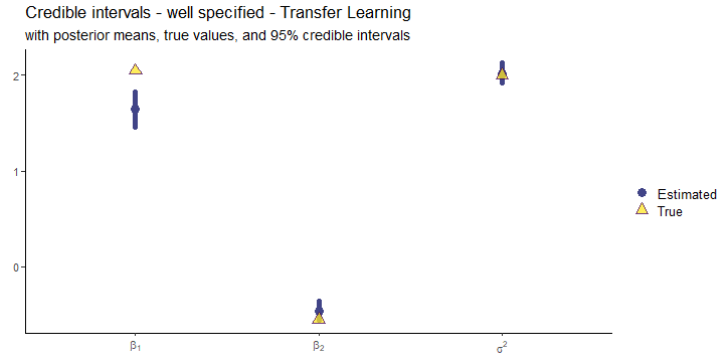


Figure S30: Posterior credible intervals for the parameters for scenario (i), with true parameters in yellow.

X includes an intercept and $p - 1$ columns generated from a standard uniform distribution over $[0, 1]$.

Building on the experimental design from Section 4.2, we explore synthetic data using three different models, all of which assign the NIG prior distribution to β and σ . We set $m_0 = 0_p$, $M_0 = 10\mathbb{I}_p$, $a_\sigma = 2$, and $b_\sigma = 2$. The models differ in the values of δ^2 and ϕ , which represent: (i) a well-specified case, using the true data-generating values $\{\delta^2 = 0.25, \phi = 10\}$; (ii) a moderately misspecified setting, with $\{\delta^2 = 0.11, \phi = 12.63\}$, where the values are incorrectly specified but relatively close to the true ones; and (iii) a highly misspecified setting, with $\{\delta^2 = 0.95, \phi = 50\}$. In addition, we include BPS as a comparison. For each approach, we partition the original dataset into $K = 10$ subsets, each consisting of 500

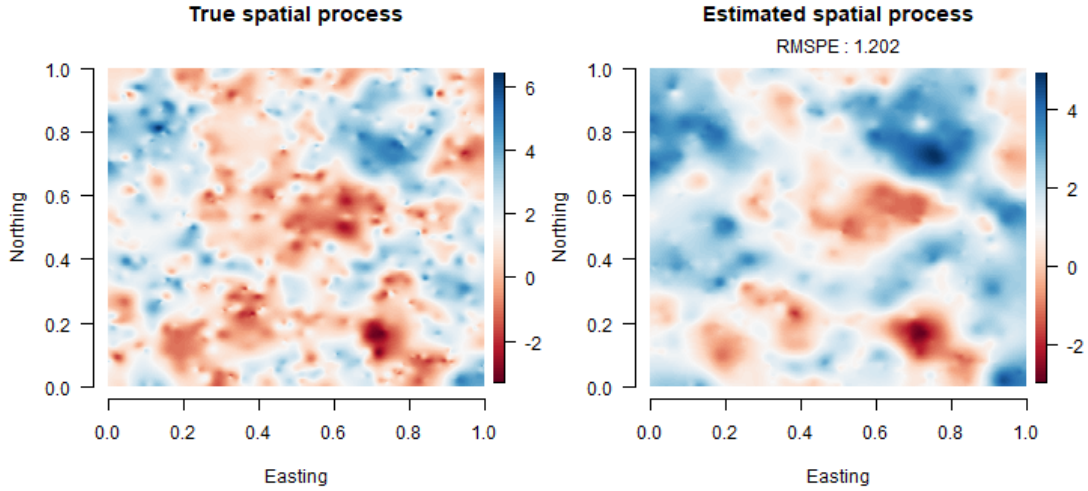


Figure S31: from left to right: comparison between the true spatial surface and the recovered surface for scenario (ii), with RMSPE.

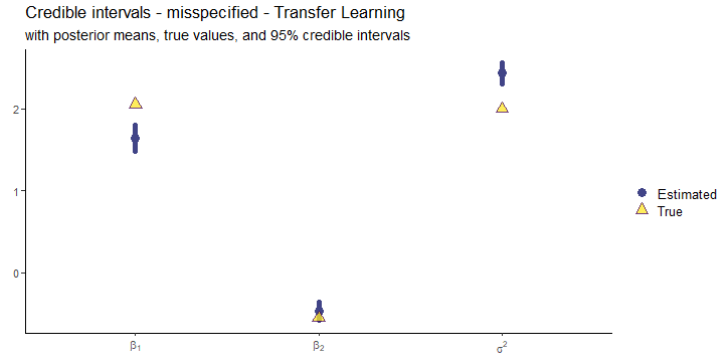


Figure S32: Posterior credible intervals for the parameters for scenario (ii), with true parameters in yellow.

units. For BPS, we consider $J = 9$ competitive models, with $\delta^2 \in \{0.10, 0.25, 0.40\}$ and $\phi \in \{8, 10, 12\}$. These values correspond to effective spatial ranges of 27%, 21%, and 18% of the maximum point inter-distance (i.e., $\sqrt{2}$) in the unit square.

We begin by presenting the results from scenario (i) and will subsequently increase the level of misspecification, concluding with the results from double Bayesian predictive stacking. For each scenario, we present two sets of results. We display the true spatial response alongside the interpolated predictive surface (posterior mean), including the associated RM-SPE. Finally, we present the posterior parameter credible intervals.

The first scenario is referred to as “well specified”, as it uses the same values for $\{\delta, \phi\}$ as those used in the data generation mechanism. Unsurprisingly, Figure S29 shows good

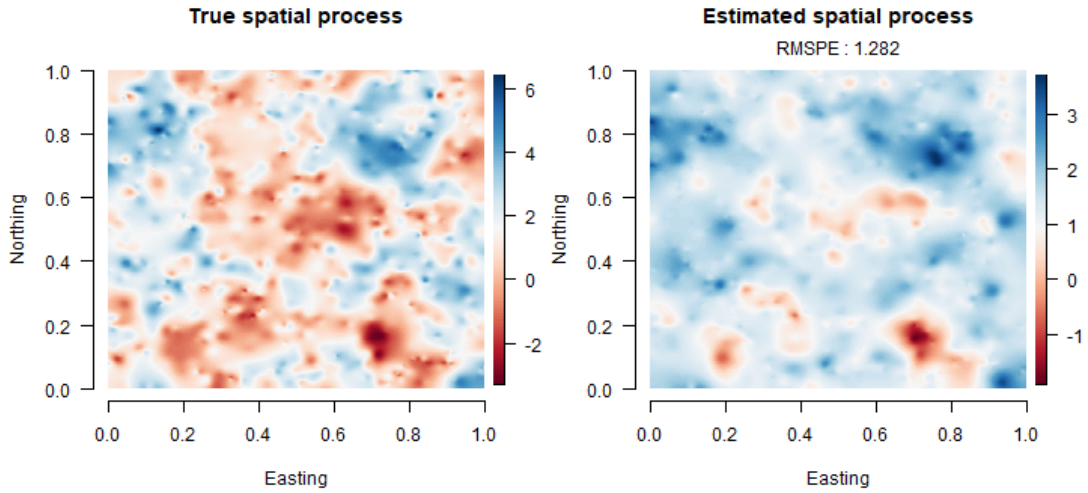


Figure S33: from left to right: comparison between the true spatial surface and the recovered surface for scenario (iii), with RMSPE.

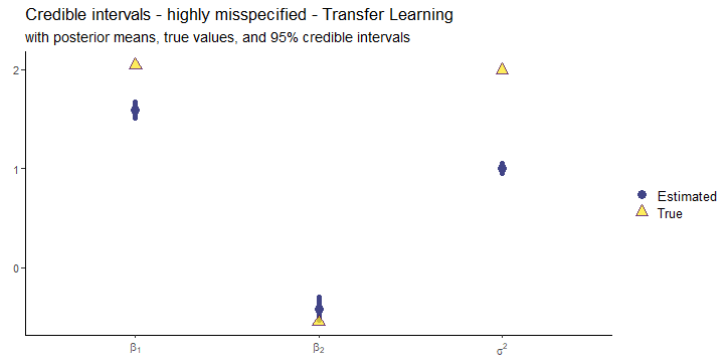


Figure S34: Posterior credible intervals for the parameters for scenario (iii), with true parameters in yellow.

predictive performance, both graphically and in terms of the RMSPE. Figure S11, which provides the posterior credible intervals, indicates effective recovery of the parameters. It is worth noting that the intercept regression coefficient falls outside the 95% credible interval. However, as will be observed in the following scenarios, this pattern occurs across all considered cases, except for BPS, which consistently provides superior MAP estimates for all parameters in model (S20).

While the results for the misspecified scenario are not as impressive as those observed in the multivariate setting shown in Section S3.2, they still perform reasonably well, considering the parameter values of $\{\delta^2 = 0.45, \phi = 6.63\}$. Despite Figure S31 does not present particularly enthusiastic results, the RMSPE is very close to that achieved in scenario (i).

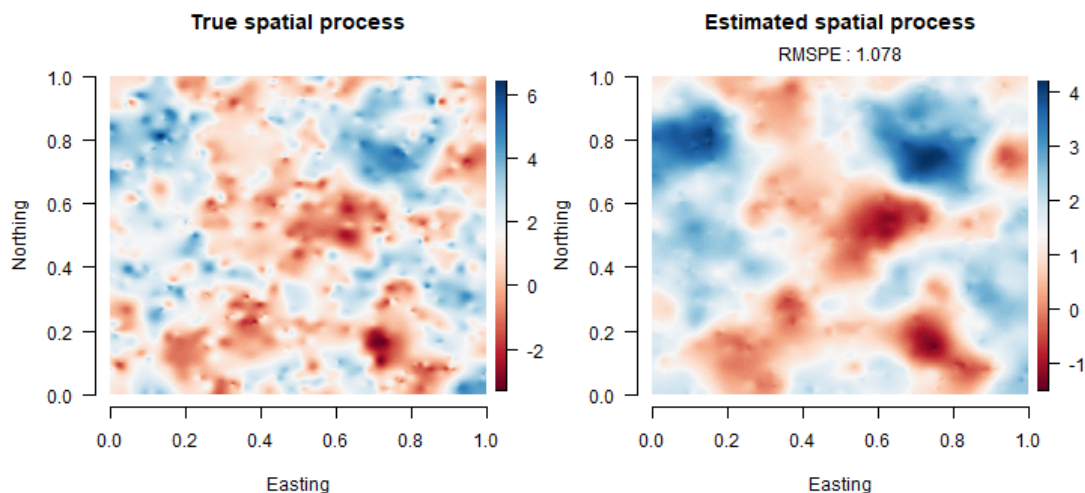


Figure S35: from left to right: comparison between the true spatial surface and the recovered surface for BPS, with RMSPE.

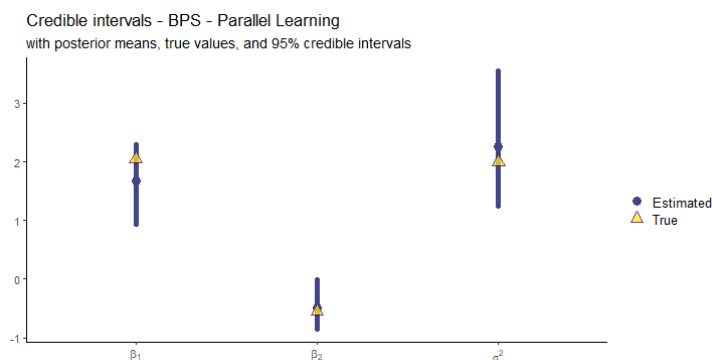


Figure S36: Posterior credible intervals for the parameters for scenario (iii), with true parameters in yellow.

Figure S32 indicates poor parameter recovery, especially for σ^2 , where the MAP estimate sensibly underestimates the true value. This reflects on the narrow range of the credible intervals presented in the same figure.

Next, we examine the outcomes of the “highly misspecified” model, corresponding to scenario (iii), which uses $\{\delta^2 = 0.95, \phi = 50\}$. As pointed out in Section 4.2, the performance in this setting is quite intriguing. We are considering a model that attributes nearly all variability to the “nugget”, implying almost absent spatial dependence. However, the theoretical conclusions drawn from Figure S33 are only marginally reliable. Comparing Figure S34 with Figure S32, it appears that scenario (iii) behaves similarly for the regression coefficients, while still strongly underestimating σ^2 , as anticipated based on its definitions. Overall, the RMSPE remains extraordinarily low relative to expectations.

Model	δ^2	ϕ	RMSPE
WELL SPECIFIED	0.25	10	1.177
MISSPECIFIED	0.11	12.63	1.202
HIGHLY MISSPECIFIED	0.95	50	1.282
DOUBLE BPS	0.26	9.89	1.078

Table S2: RMSPE and specification for each model scenario.

Last but not least, Figure S35 presents the predictive results yielded by double BPS. While the interpolation performance is striking, we will focus on the RMSPE, which demonstrates the best results across all settings. BPS outperforms scenario (i), which uses the true values for generating synthetic data. Remarkably, BPS achieves an RMSPE lower than that of scenario (i) as well as the difference observed between scenarios (i) and (iii). Figure S36 reveals that BPS also provides superior MAP estimates for all parameters, as anticipated, albeit at the cost of wider posterior credible intervals. This finding is particularly noteworthy, given that inferential performance is typically weakest for the spatial variance, which is often not identifiable from the realized data (Zhang, 2004).

Table S2 provides a summary of the predictive performances along with the specified hyperparameter values for each model. A review of Table S2 in conjunction with the figures presented above clearly illustrates the robustness of the results reported in Stein (1988); Stein and Handcock (1989). It becomes almost impossible to distinguish between the performance of the well-specified and misspecified settings. Furthermore, as observed in the multivariate case, the highly misspecified setting performs only marginally worse than the others. In contrast, BPS demonstrates a clear dominance over the alternative approaches, both in terms of predictive accuracy and posterior inferences.

S6 Application - Univariate

Among the key aspects, sea surface temperature (SST) is crucial for environmental and climate scientists. Since SST is a determinant of the exchanges of vapor, and heat, from

ocean to atmosphere. Here, we present an application of the BPS approach for univariate models, fully described in the Section S4, indeed on sea surface temperature data. The aforementioned development has the scope to enable researchers to perform geostatistical analysis on massive spatial data sets, even with modest computational and memory resources. Thanks to the conjugate framework, together with the BPS to remove the dependence from nuisance hyperparameters δ^2, ϕ , Bayesian model-based inference for geostatistical regression is hastened. This is achieved without compromising the inferences. As an illustration, we analyze a data set composed of 1,002,500 georeferenced observations of SST, collected within June 2022. To this end, we gather the dataset on the National Oceanic and Atmospheric Administration (NOAA) data server. We consider SST data that extend all over the world, for all the oceans. Within this massive data set, we use $n = 1,000,000$ observations for model fitting while the rest for predictive assessment. As explanatory variables, in order to gather the trend structure across the world, we consider the coordinates after a sinusoidal projection and scaled to 1,000 kilometers units, plus an intercept, leading to $p = 3$. For the spatial covariance function, we choose to use an exponential kernel. Prior choices follow standard choices, as specified in (2.5), and as considered in Banerjee (2017); Zhang et al. (2021). As a matter of fact, we consider the NIG joint prior in Section S4, where we fix as follow its parameters: $m_0 = 0_p$, $M_0 = 10\mathbb{I}_p$, $a_\sigma = 2$, and $b_\sigma = 2$. The set of hyperparameter values was defined by considering explanatory spatial data analysis and evaluating the empirical variogram to find insight about ϕ and δ^2 , see Section S7. Since the variogram suggests the absence of a nugget, we assign a near-zero value to the noise-to-spatial variance ratio, that is $\delta^2 = 10^{-6}$. While, again from EDA, we opt to the following values for range parameter $\phi \in \{0.0163, 0.0244, 0.0326\}$. Regarding the partition strategy, considering the result in Section S3.3, we take into account $K \in \{2,000, 4,000\}$ as the number of subsets, which correspond to the subset size of $n_k = \{500, 250\}$ units respectively. For both values of K , the subsets were created by random samples of observations all over the global ocean

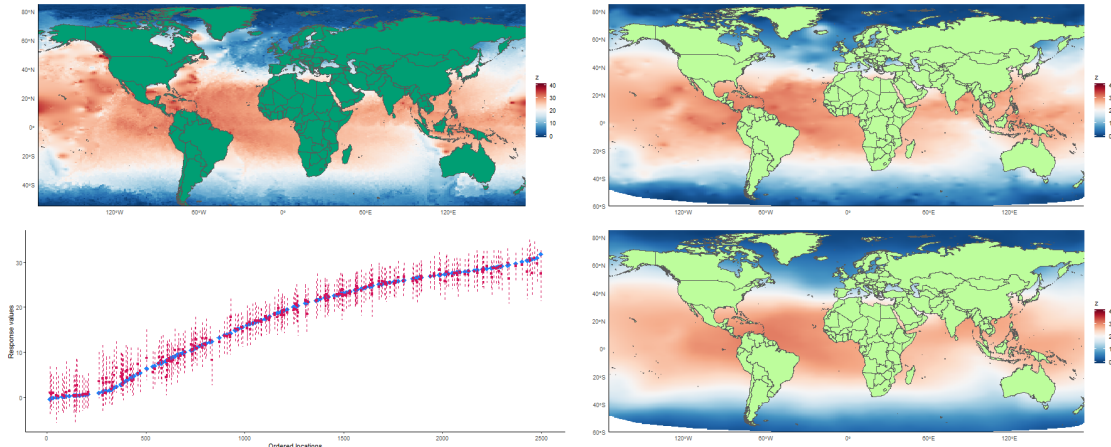


Figure S37: from left to right: comparison between training (top left panel), test (top right panel), and predicted surface (bottom right panel). In addition, the empirical coverage for the response (bottom left panel). Results for $K = 2,000$.

surface, avoiding block or clustering partition, as suggested in [Guhaniyogi and Banerjee \(2018\)](#). However, we mainly discuss the results for $K = 2,000$ only, while [Table S3](#) reports the outcomes for both the K considered.

[Figure S37](#) displays a set of interpolated maps for $K = 2,000$. From the top left to the top right corners, we find the interpolation maps of the training and test SST data respectively. In these maps, as in the other, SST is represented in a shade of colors. Warmer colors correspond to higher sea surface temperatures, on the contrary, colder colors are shown, which means a lower temperature. From the cartoon, the SST shows a clear spatial pattern. Indeed from the equator to the tropics, one can find high surface temperatures on average, while a drop in the temperatures happens by moving toward the poles. Besides the interpolations of training and test data, [Figure S37](#) also shows a third interpolations map. Indeed, in the bottom right corner of [Figure S37](#) there is the predicted posterior means interpolation, obtained from the BPS model with $K = 2,000$, for the withheld test locations. From this cartoon, it is evident the capability of the model to recover the true response surface. As a matter of fact, by looking in detail, one can spot that it gets all the variations of temperature happening all over the world's surface. As commonly observed with meta-kriging approaches, a sort of over-smoothing is still present. Even if it could be seen as a shortcoming, it is reconducted to a better generalization ability, avoiding overfitting phenomena. This can

also be extrapolated by noticing the striking improvement in terms of RMSPE with respect to a nonspatial Bayesian conjugate linear model (BLM). The RMSPE for the nonspatial model is indeed 9.855, while for the double BPS, a substantially lower root mean square predictive error of 1.165 for $K = 2,000$, and 1.556 when $K = 4,000$, is achieved. Due to the sensible higher values of RMSPE of the BLM, we have insight into the fact that coordinates alone do not capture the spatial dependencies present in sea surface temperature data adequately. Not only in terms of predictive performance but also the uncertainty quantification from BPS produces good results, despite the number of partitions. The bottom left corner of Figure S37, shows the ordered withheld locations, and the predictive 95% credible intervals (complete of MAP estimates). Displaying a quite high coverage, corresponding to an empirical coverage of 99.4%. This disproves in this case the underestimation of the variability, often associated with meta-learning approaches. Looking to the right column in Figure S37, the fitted sea surface temperature interpolated map over the test data, obtained from BPS, is almost indistinguishable from the true one. Moreover, the good predictive performance achieved in the analysis is based on only 250 posterior predictive samples, since the conjugate framework. This was gained, without using huge computational resources, but just a laptop. The entire process with $K = 2,000$ subsets, concerning the Divide-Conquer approach (subset estimation, combination, full posterior inference, and prediction), takes slightly more than 1 hour, or 63 minutes for precision. Even more striking than this, is the computational time achieved when $K = 4,000$, which is only 16 minutes. Empirically showing a quadratic order of dependence upon the number of locations within each partition, while an almost indistinguishable RMSPE was obtained.

Lastly, in Table S3 we illustrate a comparison between the posterior sample for β, σ^2 , obtained by a Bayesian conjugate linear model, and BPS for $K \in \{4,000, 2,000\}$. The posterior inferences vary consistently passing from the non-spatial model to BPS. For the former, we observe inflated distribution for intercept β_0 , and the variance σ^2 , which show

	Conjugate linear model	BPS ($K = 4,000$)	BPS ($K = 2,000$)
β_0	17.890 (17.87, 17.91)	10.378 (4.146, 14.306)	8.846 (3.382, 12.627)
β_{long}	0.010 (0.01, 0.02)	-0.051 (-0.318, 0.236)	-0.040 (-0.347, 0.221)
β_{lat}	-0.540 (-0.550, -0.540)	-0.190 (-0.661, 0.308)	-0.102 (-0.427, 0.412)
σ^2	96.470 (96.21, 96.73)	30.860 (22.142, 48.058)	25.607 (18.032, 38.050)
RMSPE	9.855	1.556	1.165
Time	<1	16	63

Table S3: Sea Surface Temperature data analysis parameter estimates, RMSPE, and computing time in minutes for candidate models. Parameter posterior summary 50 (2.5, 97.5) percentiles.

posterior distributions located over high values with respect to the range of response variable. Bayesian predictive stacking modeling provides more reasonable estimates. Moreover, for both values of K , the direction of association with the scaled longitude β_{long} result inverted with regard to Bayesian conjugate modeling.

S7 Exploratory data analysis

We present results from two explanatory spatial data analyses that complement Sections 5 and S6. Variograms are employed in both analyses to extract “guidelines” on spatial parameters such as spatial variability proportion α , signal-to-noise ratio δ^2 , and spatial range ϕ , which are essential for setting up the double BPS framework for GeoAI applications. Fitting variograms, as described below, to glean the required parameters for BPS are automated and require no human intervention.

We first examine the spatial properties of Vegetation Index data in Section 5 focusing on two response variables: the Normalized Difference Vegetation Index (NDVI) and Red Reflectance (RR). As in the SST analysis, we use independent sample variograms for NDVI and RR, based on 31,875 randomly sampled locations. For NDVI, the empirical variogram estimates the nugget 0.03, a sill of 0.27, and a practical range of approximately 88 based upon automated weighted least squares. This corresponds to significant spatial correlation up to about 10,000 kilometers. The proportion of spatial variability is computed as $\alpha = \sigma^2/(\tau^2 + \sigma^2) = 0.27/(0.03 + 0.27) \approx 0.9$, resulting in 0.909 without rounding. Finally, the

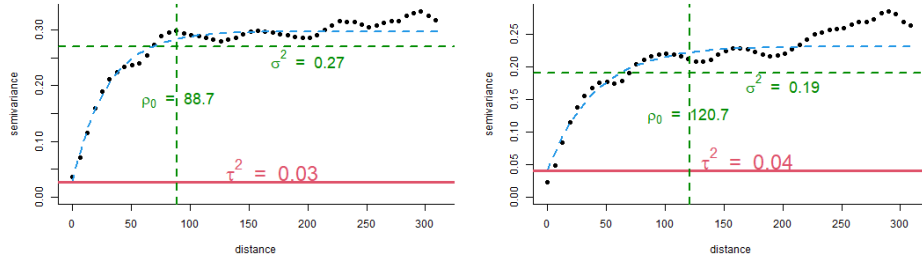


Figure S38: From left to right: sample variograms of NDVI, and Red Reflectance.

spatial range parameter is estimated as $\phi = 0.067$ based upon the distance beyond which the spatial correlation drops to less than 0.05; see the left panel of Figure S38.

For RR, the variogram parameters include a nugget effect of 0.04, a sill of 0.19, and a practical range of approximately 120, which corresponds to around 13,000 kilometers. The slightly higher nugget effect for RR suggests greater measurement error or micro-scale variability compared to NDVI. The proportion of spatial variability is estimated as $\alpha = 0.19/(0.04 + 0.19) \approx 0.825$. The practical range for RR is more extended than that of NDVI, indicating that RR values remain spatially correlated over a greater distance. Concluding the exploratory spatial data analysis, we select a spatial range of $\phi = 0.049$ for RR.

The combined analysis of the variograms for NDVI and RR provides essential information about the spatial variance proportion and range parameters, which are critical for informing artificially intelligent geospatial modeling systems. This analysis results in $\alpha \in \{0.825, 0.909\}$ and $\phi \in \{0.049, 0.067\}$. These findings help improve the accuracy of spatial predictions, enhancing ecological interpretations, and increasing computational efficiency by avoiding excessive misspecified model specifications.

In the second exploratory analysis, associated with Section S6, we explore the spatial characteristics of the SST data using a sample variogram. The variogram provides a deeper understanding of spatial dependence in the SST measurements, crucial for defining a plausible set of values for parameters such as the signal-to-noise ratio δ^2 and spatial range ϕ .

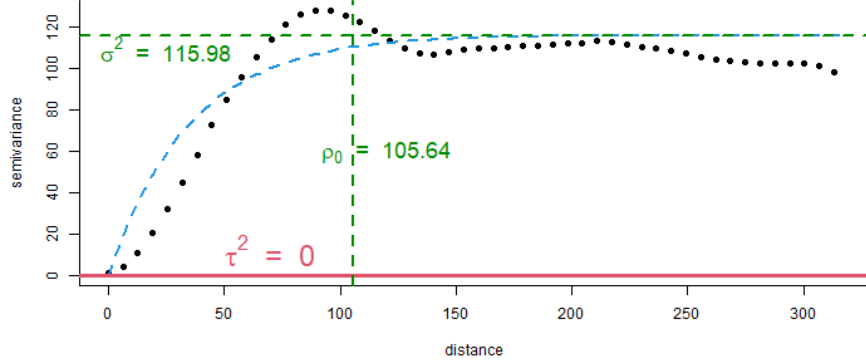


Figure S39: Sample variogram of SST data.

The empirical variogram, depicted in Figure S39, shows the semi-variance as a function of distance, revealing key spatial statistics. For our SST data, based on 25,000 randomly sampled locations, the variogram indicates no nugget effect, $\tau^2 = 0$, a sill of 115.98, and a practical range of $\rho_0 = 105.64$. This implies that SST measurements become almost spatially uncorrelated beyond a distance of approximately 11.5 thousand kilometers. The practical range, ρ_0 , is the distance within which data points exhibit substantial spatial correlation. The absence of a nugget effect suggests no measurement error or micro-scale variability at distances approaching zero. In Section S6, after testing several values in the interval $(10^{-8}, 10^{-1})$, we fix $\delta^2 = 10^{-6}$. The data exhibit extremely strong spatial dependence, as confirmed by Figure S39, reinforcing the choice of this parameter. These findings provide a comprehensive view of the spatial structure, which is critical for subsequent geostatistical modeling and spatial predictions.

For the exponential spatial covariance parameter ϕ , we take advantage of empirical variogram estimation. A crucial consideration here is the “over-smoothing” often observed with BPS, which suggests that wider or doubled values of ϕ compared to variogram-based estimates may be more appropriate. In Section S6, we expand the initial point estimate of ϕ by one-third, considering the set $\phi \in \{0.0163, 0.0244, 0.0326\}$ for further analysis.

References

- Banerjee, S. (2017). High-Dimensional Bayesian Geostatistics. *Bayesian Analysis* 12(2), 583–614.
- Banerjee, S. (2020). Modeling massive spatial datasets using a conjugate bayesian linear modeling framework. *Spatial Statistics* 37, 100417. *Frontiers in Spatial and Spatio-temporal Research*.
- CVX Research, I. (2012, August). CVX: Matlab software for disciplined convex programming, version 2.0.
- Finley, A. O., A. Datta, B. D. Cook, D. C. Morton, H.-E. Andersen, and S. Banerjee (2017). Efficient algorithms for bayesian nearest neighbor gaussian processes. *Journal of Computational and Graphical Statistics* 28(2), 401–414.
- Fu, A. and B. Narasimhan (2023). *ECOSolveR: Embedded Conic Solver in R*. R package version 0.5.5.
- Fu, A., B. Narasimhan, and S. Boyd (2020). Cvxr: An r package for disciplined convex optimization. *Journal of Statistical Software* 94(14), 1–34.
- Grant, M. C. (2005). *Disciplined convex programming*. Ph. D. thesis.
- Guhaniyogi, R. and S. Banerjee (2018). Meta-kriging: Scalable bayesian modeling and inference for massive spatial datasets. *Technometrics* 60(4), 430–444.
- Gupta, A. K. and D. K. Nagar (2000). *Matrix variate distributions*. Monographs and surveys in pure and applied mathematics. Boca Raton: Chapman & Hall/CRC.
- Iranmanesh, A., M. Arashi, and S. M. M. a. Tabatabaey (2010). On conditional applications of matrix variate normal distribution. *Iranian Journal of Mathematical Sciences and Informatics* 5(2), 33–43.

- Minsker, S., S. Srivastava, L. Lin, and D. B. Dunson (2017). Robust and scalable bayes via a median of subset posterior measures. *Journal of Machine Learning Research* 18(124), 1–40.
- O’Donoghue, B., E. Chu, P. Neal, and S. Boyd (2016, Jun). Operator splitting for conic optimization via homogeneous self-dual embedding. *Journal of Optimization Theory and Applications* 169(3), 1042–1068.
- Stein, M. L. (1988). Asymptotically efficient prediction of a random field with a misspecified covariance function. *The Annals of Statistics* 16(1), 55–63.
- Stein, M. L. and M. S. Handcock (1989). Some asymptotic properties of kriging when the covariance function is misspecified. *Mathematical Geology* 21, 171–190.
- Yao, Y., A. Vehtari, D. Simpson, and A. Gelman (2018). Using Stacking to Average Bayesian Predictive Distributions (with Discussion). *Bayesian Analysis* 13(3), 917–1007.
- Zhang, H. (2004). Inconsistent estimation and asymptotically equal interpolations in model-based geostatistics. *Journal of the American Statistical Association* 99(465), 250–261.
- Zhang, L., S. Banerjee, and A. O. Finley (2021). High-dimensional multivariate geostatistics: A bayesian matrix-normal approach. *Environmetrics* 32(4), e2675.
- Zhang, L., W. Tang, and S. Banerjee (2024). Bayesian geostatistics using predictive stacking.